PAVEL KISEL

KF PARTICLE FINDER: MISSING MASS METHOD FOR RECONSTRUCTION OF STRANGE PARTICLES IN CBM (FAIR) AND STAR (BNL) EXPERIMENTS

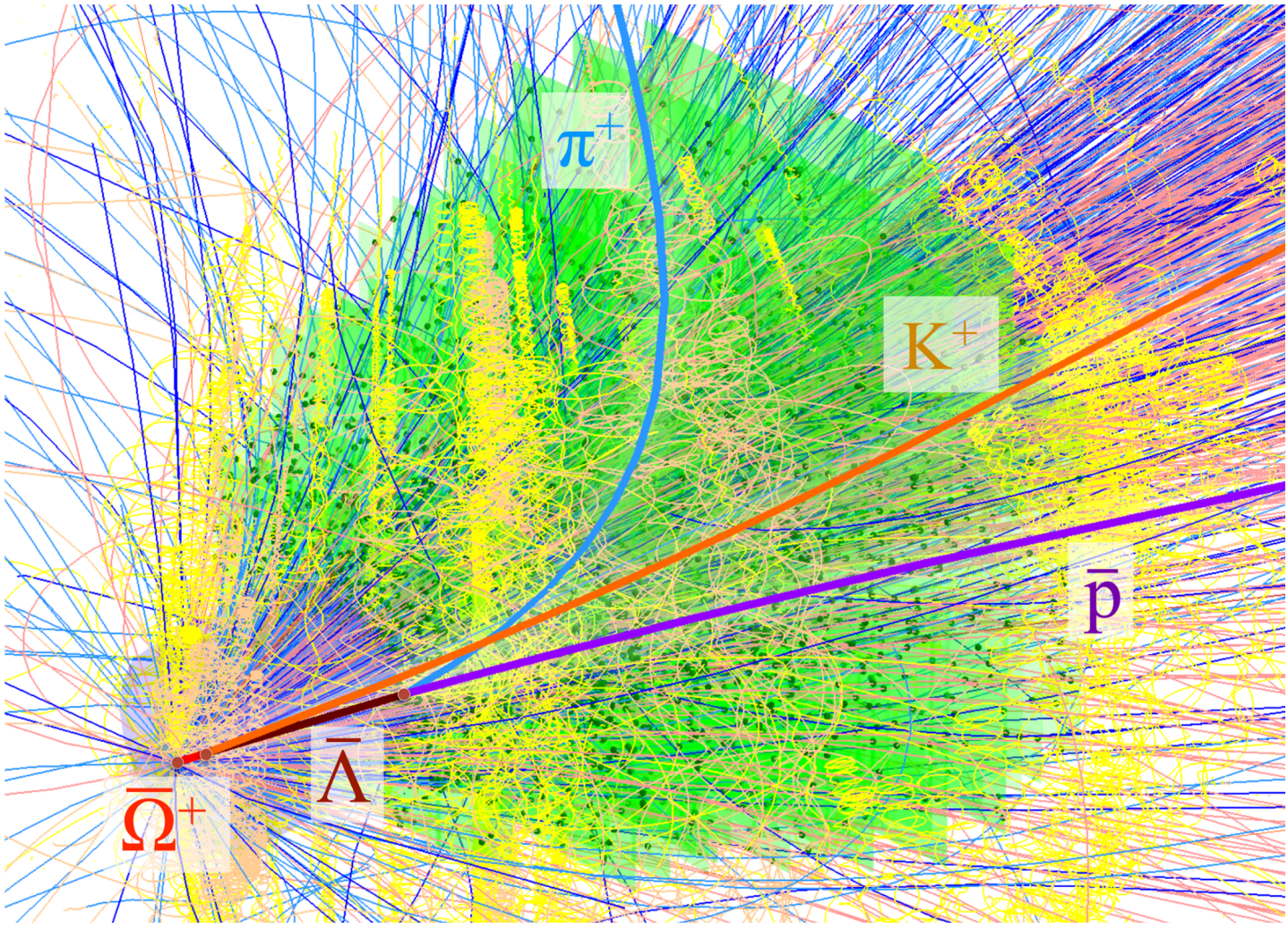

Frankfurt am Main 2022

KF Particle Finder Package: Missing Mass Method for Reconstruction of Strange Particles in CBM (FAIR) and STAR (BNL) Experiments

Dissertation
zur Erlangung des Doktorgrades
der Naturwissenschaften

vorgelegt beim Fachbereich Informatik und Mathematik
der Johann Wolfgang Goethe-Universität
in Frankfurt am Main

von
Pavel Kisel
aus Dubna

Frankfurt am Main 2022
(D 30)

Vom Fachbereich Informatik und Mathematik
der Johann Wolfgang Goethe-Universität
als Dissertation angenommen

Dekan	Prof. Dr. Martin Möller
Gutachter	Prof. Dr. Volker Lindenstruth Prof. Dr. Thorsten Kollegger
Datum der Disputation	03. November 2022

Abstract

The main task of modern large experiments with heavy ions, such as CBM (FAIR), STAR (BNL) and ALICE (CERN) is a detailed study of the phase diagram of quantum chromodynamics (QCD) in the quark-gluon plasma (QGP), the equation of state of matter at extremely high baryonic densities, and the transition from the hadronic phase of matter to the quark-gluon phase.

In the thesis, the missing mass method is developed for the reconstruction of short-lived particles with neutral particles in their decay products, as well as its implementation in the form of fast algorithms and a set of software for practical application in heavy ion physics experiments. Mathematical procedures implementing the method were developed and implemented within the KF Particle Finder package for the future CBM (FAIR) experiment and subsequently adapted and applied for processing and analysis of real data in the STAR (BNL) experiment.

The KF Particle Finder package is designed to reconstruct most signal particles from the physics program of the CBM experiment, including strange particles, strange resonances, hypernuclei, light vector mesons, charm particles and charmonium. The package includes searches for over a hundred decays of short-lived particles. This makes the KF Particle Finder a universal platform for short-lived particle reconstruction and physics analysis both online and offline.

The missing mass method has been proposed to reconstruct decays of short-lived charged particles when one of the daughter particles is neutral and is not registered in the detector system. The implementation of the missing mass method was integrated into the KF Particle Finder package to search for 18 decays with a neutral daughter particle.

Like all other algorithms of the KF Particle Finder package, the missing mass method is implemented with extensive use of vector (SIMD) instructions and is optimized for parallel operation on modern many-core high performance computer clusters, which can include both processors and coprocessors. A set of algorithms implementing the method was tested on computers with tens of cores and showed high speed and practically linear scalability with respect to the number of cores involved.

It is extremely important, especially for the initial stage of the CBM experiment, which is planned for 2025, to demonstrate already now on real data the reliability of the developed approach, as well as the high efficiency of the current implementation of both the entire KF Particle Finder package, and its integral part, the missing mass method. Such an opportunity was provided by the FAIR Phase-0 program, motivating the use in the STAR experiment of software packages originally developed for the CBM experiment.

Application of the method to real data of the STAR experiment shows very good results with a high signal-to-background ratio and a large significance value. The results demonstrate the reliability and high efficiency of the missing mass method in the reconstruction of both charged mother particles and their neutral daughter particles. Being an integral part of the KF Particle Finder package, now the main approach for reconstruction and analysis of short-lived particles in the STAR experiment, the missing mass method will continue to be used for the physics analysis in online and offline modes.

The high quality of the results of the express data analysis has led to their status as preliminary physics results with the right to present them at international physics conferences and meetings on behalf of the STAR Collaboration.

Kurzfassung

Die wichtigste Aufgabe moderner Großexperimente mit schweren Ionen wie CBM (FAIR), STAR (BNL) und ALICE (CERN) ist eine detaillierte Untersuchung des Phasendiagramms der Quantenchromodynamik (QCD) im Quark-Gluon-Plasma (QGP), der Zustandsgleichung der Materie bei extrem hohen Baryonendichten und des Übergangs von der hadronischen Phase der Materie zur Quark-Gluon-Phase.

In der Dissertation wird die Missing-Mass-Methode für die Rekonstruktion kurzlebiger Teilchen mit neutralen Teilchen in ihren Zerfallsprodukten entwickelt und in Form von schnellen Algorithmen und Software für die praktische Anwendung in Experimenten der Schwerionenphysik umgesetzt. Die mathematischen Verfahren zur Umsetzung der Methode wurden für das zukünftige CBM-Experiment (FAIR) entwickelt und in das KF Particle Finder-Paket implementiert und anschließend für die Verarbeitung und Analyse von realen Daten im STAR-Experiment (BNL) angepasst und angewendet.

Das KF Particle Finder-Paket wurde entwickelt, um die meisten Signalteilchen aus dem Physikprogramm des CBM-Experiments zu rekonstruieren, darunter Strange-Teilchen, Strange-Resonanzen, Hypernuklei, leichte Vektormesonen, Charm-Teilchen und Charmonium. Das Paket umfasst die Suche nach über hundert Zerfallsprozessen von kurzlebigen Teilchen. Dies macht den KF Particle Finder zu einer universellen Plattform für die Rekonstruktion kurzlebiger Teilchen und die physikalische Analyse, sowohl online als auch offline.

Die Missing-Mass-Methode wurde vorgeschlagen, um Zerfallsprozesse von kurzlebigen geladenen Teilchen zu rekonstruieren, wenn eines der Tochterteilchen neutral ist und nicht im Detektorsystem registriert wird. Die Implementierung der Missing-Mass-Methode wurde in das KF Particle Finder Paket integriert, um nach 18 Zerfällen mit einem neutralen Tochterteilchen zu suchen.

Wie alle anderen Algorithmen des KF Particle Finder-Pakets ist auch die Missing-Mass-Methode unter extensiver Verwendung von Vektorbefehlen (SIMD) implementiert und für den parallelen Einsatz auf modernen Multi-Core-Hochleistungsrechnern optimiert, die sowohl Prozessoren als auch Coprozessoren umfassen können. Eine Reihe von Algorithmen zur Umsetzung der Methode

wurde auf Rechnern mit mehreren Dutzend Kernen getestet und zeigte eine hohe Geschwindigkeit und praktisch lineare Skalierbarkeit in Bezug auf die Anzahl der beteiligten Kerne.

Vor allem für die Anfangsphase des für 2025 geplanten CBM-Experiments ist es äußerst wichtig, bereits jetzt mit realen Daten die Zuverlässigkeit des entwickelten Ansatzes, sowie die hohe Effizienz der derzeitigen Implementierung des gesamten KF Particle Finder-Pakets und seines integralen Bestandteils, der die Missing-Mass-Methode implementiert, nachzuweisen. Eine solche Gelegenheit bot das FAIR-Phase-0-Programm, das den Einsatz der ursprünglich für das CBM-Experiment entwickelten Softwarepakete im STAR-Experiment anregte.

Die Anwendung der Methode auf reale Daten des STAR-Experiments weist sehr gute Ergebnisse mit einem hohen Signal-Hintergrund-Verhältnis und einem großen Signifikanzwert auf. Die Ergebnisse zeigen die Zuverlässigkeit und hohe Effizienz der Missing-Mass-Methode bei der Rekonstruktion sowohl geladener Mutterteilchen als auch neutralen Tochterteilchen. Als integraler Bestandteil des KF Particle Finder-Pakets, das jetzt der Hauptansatz für die Rekonstruktion und Analyse kurzlebiger Teilchen des STAR-Experiments ist, wird die Missing-Mass-Methode weiterhin für die physikalische Analyse im Online- und Offline-Modus verwendet werden.

Die hohe Qualität der Ergebnisse der Express-Datenanalyse hat dazu geführt, dass sie den Status von vorläufigen physikalischen Ergebnissen erhalten haben und im Namen der STAR-Kollaboration auf internationalen Konferenzen und Tagungen vorgestellt werden dürfen.

Contents

Chapter 1

Introduction

Relativistic heavy ion physics aims at investigating fundamental properties of matter, namely at studying properties of quark-gluon plasma (QGP) and better understanding of quantum chromodynamics (QCD). The fundamental properties of matter are closely related not only to processes in the microcosm, but also to processes on the cosmic scale. Thus, the study of heavy ion collisions at high energies allows to understand processes at the very beginning of the birth of the Universe after the Big Bang, while collisions at low energies reproduce processes inside neutron stars, when a star is in the last stage of its evolution before turning into a black hole.

Relevance of the thesis

Studies of heavy ion physics are carried out at accelerators at the world's largest scientific centers: LHC (CERN, Switzerland), RHIC (BNL, USA) and FAIR (GSI, Germany).

During collisions of heavy ions (most often lead or gold ions) hundreds of protons and neutrons collide with each other with energies ranging from several GeV to several TeV. When two such nuclei with velocities close to those of light collide with each other, the matter undergoes a transition, forming for a short moment a droplet of hot matter, the so-called quark-gluon plasma. Quark-gluon plasma is formed when protons and neutrons "melt down" into their elementary constituents, and quarks and gluons become asymptotically free in a small volume of colliding nuclei. The QGP droplet cools momentarily, and individual quarks and gluons (also called partons) recombine into particles of ordinary matter, which fly off in all directions and are registered in the detector system of the experiment. Experiments with heavy ions make it possible to reproduce and study the fundamental processes of the Universe under laboratory conditions.

The standard model postulates the existence of 12 fundamental elementary particles with spin 1/2: 6 leptons (electron e^-, muon μ^-, tau lepton τ^-, corresponding

neutrinos ν_e, ν_μ and ν_τ), 6 quarks (u, d, s, c, b, t) and their antiparticles. Quarks have a so-called color charge, which determines their participation in the strong interaction. The presence of electric charge and isospin allows them to interact with other fermions electromagnetically and weakly, respectively. Charged leptons (electron, muon, tau) have no color charge and can participate in weak and electromagnetic interactions. Neutral leptons (neutrinos) have no electric charge, and participate only in weak interactions. The strong interaction is carried by 8 types of gluons, the weak interaction is mediated by 3 gauge bosons (W^+, W^-, Z^0), the photon provides the electromagnetic interaction. Weak interaction, unlike electromagnetic and strong interaction, can mix fermions from different generations. This is the reason why all particles become unstable, except for the lightest particles. Masses of particles are formed as a consequence of the scalar field of Higgs bosons. At present the Standard Model is the main theoretical model for describing the microcosm.

Colliding nuclei consist of protons and neutrons, which in turn consist of u (mass 2.4 MeV/c^2) and d (4.8 MeV/c^2) quarks. The strange quark s is the lightest (95 MeV/c^2) of the other quarks, so when heavy ions collide, the probability of forming particles that include the strange quark is the highest. Thus, the produced particles containing strange quarks carry information about the collision process. In addition, it was found experimentally that the yield of strange particles increases with the formation of QGP, so they are a good source of information about the properties of quark-gluon plasma.

One of the major experiments to study the properties of quark-gluon plasma using heavy ions will be the CBM (Compressed Baryonic Matter) experiment, which is currently under construction at the FAIR (Facility for Antiproton and Ion Research) acceleration complex in Darmstadt, Germany. The experiment is scheduled to start operating in 2025.

The scientific program of the CBM experiment includes:

- equation of state of nuclear matter at neutron star density,
- changes in the properties of hadrons of dense baryonic matter as a sign of the restoration of chiral symmetry,
- phase transitions from hadronic matter to quark or parton matter at high baryonic density and the critical point of QCD matter,
- hypernuclei, strange dibaryons, and massive strange particles,
- mechanisms of charm formation, its propagation and properties of charmed particles in (dense) nuclear matter.

In the experiment, up to 10^7 Au+Au collisions per second are expected, each of which will produce up to 1000 charged particles. Reconstructing particle trajectories in a non-homogeneous magnetic field, as well as searching for short-lived particles, which are of primary interest in the study of the physics program, is an extremely challenging task. To solve this problem, the FLES (First Level Event Selection) package of algorithms for reconstruction and analysis was created in the CBM experiment, which includes, among others, a software package KF Particle of algorithms based on the Kalman Filter (KF) to search for short-lived particles and its online version KF Particle Finder to work in real time. All reconstruction algorithms of the FLES package are vectorized and parallelized, providing fast and efficient reconstruction of collisions in the CBM experiment.

In order to comprehensively study the decays of strange particles, which, as noted above, carry important information about the properties of compressed baryonic matter produced in heavy ion collisions, the missing mass method has been developed and implemented within the KF Particle package.

The missing mass method is used to reconstruct decays of short-lived charged particles when one of the daughter particles is neutral and is not registered in the detector system of the experiment. The method is based on the use of the laws of conservation of energy and momentum.

As an example of such short-lived particles, the decay channels and their probabilities for Σ^- and Σ^+ particles, as well as their antiparticles, can be given:

$$\begin{array}{lll} \Sigma^- \to n\pi^- & \overline{\Sigma}^+ \to \overline{n}\pi^+ & BR = 99.85\% \\ \Sigma^+ \to p\pi^0 & \overline{\Sigma}^- \to \overline{p}\pi^0 & BR = 51.57\% \\ \Sigma^+ \to n\pi^+ & \overline{\Sigma}^- \to \overline{n}\pi^- & BR = 48.31\% \end{array}$$

As can be seen, they all have a neutral particle in the decay products, and the missing mass method is the only method for their reconstruction and further analysis.

Let's illustrate how the missing mass method works using an example of decay

$$\Sigma^- \quad \to \quad n\pi^-. \tag{1.1}$$

In this decay, the daughter pion is registered in the tracking detector and identified in one of the identification (PID, Particle Identification) detectors, whereas the neutron, being a neutral particle, is not registered in the detector system. However, Σ^-, although it has a short lifetime $c\tau_{\Sigma^-} = 4.4$ cm, but in fixed-target experiments the average trajectory length in the laboratory coordinate system due to relativistic boost can reach 15–20 cm. In this case the Σ^- particle can cross several tracking stations, be registered and then reconstructed. Thus, in

this decay it becomes possible to reconstruct trajectories of both charged particles, but Σ^-, unlike π^-, still cannot be identified, since it does not reach PID detectors.

Reconstruction of a short-lived charged particle by the missing mass method is performed in three steps:

1. reconstruction of the trajectories of the charged mother particle Σ^- and its charged daughter particle π^- in the tracking system;

2. reconstruction of the parameters of the neutral daughter n particle based on the parameters of the mother Σ^- and the charged daughter π^- particles;

3. reconstruction of the mass spectrum of Σ^- using the parameters of the n and π^- daughter particles.

A set of algorithms implementing the missing mass method has been developed in its basic version and successfully applied to simulated data of the CBM experiment. This demonstrated the applicability of the developed approach to the CBM experiment, as well as its importance for the realization of the experimental physics program.

Later, in the process of intensive and comprehensive investigations and applications in the CBM experiment, the implementation of the missing mass method was considerably extended and improved. For example, the mathematical part of the method's implementation has been significantly improved, using a more accurate and faster algorithm; in particular, all the main calculations have been performed with matrices 6×6 instead of the previous 7×7, due to the fact that the parameter energy has been removed from the state vector and from the covariance matrix. The energy and mass calculations are now performed separately in the last step, and the parameters of all short-lived particles are estimated in one iteration of subtraction by the Kalman filter method instead of the previous two, subtraction and then addition, in the initial version. This also eliminated the need for a very resource-intensive mass constraint method, which balanced the particle parameters at a certain stage of the computation, which also introduced additional inaccuracies and greatly slowed down the computation process. Such a mathematically more accurate implementation of the missing mass method has significantly improved the quality of reconstruction of short-lived particles, resulting in a twofold increase in the efficiency of their reconstruction and a 25–30% increase in the significance of the signal data.

Like all other algorithms in the KF Particle and KF Particle Finder packages, the missing mass method is implemented with extensive use of vector (SIMD, Single Instruction, Multiple Data) instructions and is optimized for parallel operation on modern many-core high performance computer systems, which can include

both processors and coprocessors. A set of algorithms implementing the method was tested on computers with dozens of cores and showed high speed and almost linear scalability with respect to the number of cores involved.

It is extremely important, especially for the initial stage of the CBM experiment, which is planned for 2025, to demonstrate already now on real data the reliability of the developed approach, as well as the high efficiency of the current implementation of both the entire KF Particle Finder package, and its integral part, implementing the missing mass method. Such an opportunity was provided by the FAIR Phase-0 program, motivating the use of the software packages originally developed for the CBM experiment in the STAR experiment.

The missing mass method, both in its initial and then improved version, has been used in real time to search for pion ($\pi^{\pm} \to \mu^{\pm}\nu$) and kaon ($K^{\pm} \to \mu^{\pm}\nu$ and $K^{\pm} \to \pi^{\pm}\pi^{0}$) decays in real data of 2 M Au+Au collisions at energies 5.75, 7.3, 9.8, and 26.5 GeV/n with a fixed target, collected in 2020 as part of the BES-II beam energy scan program and reconstructed online using a chain of algorithms for express production and analysis of the data on the High Level Trigger (HLT) computer cluster. It was shown that in the improved version of the missing mass method in the $\pi^{\pm} \to \mu^{\pm}\nu$ channels, the signal increases 40 fold and the significance — 7 fold. In $K^{\pm} \to \mu^{\pm}\nu$ and $K^{\pm} \to \pi^{\pm}\pi^{0}$ channels, the signal increases by 2 fold and the significance increases by 1.5 fold compared to the initial version. Application of the method to real data shows very good results with a high signal-to-background ratio and a large value of significance. In the case of pion decays $\pi^{\pm} \to \mu^{\pm}\nu$ it was possible to obtain a practically clean signal with almost complete absence of background.

These results were obtained during online data analysis in the express chain on the HLT cluster, while the detector system was still undergoing calibration and alignment. With standard offline data processing, the results will be improved due to full calibration of all detector systems of the STAR setup.

The results demonstrate the reliability and high efficiency of the missing mass method in the reconstruction of both charged mother particles and their neutral daughter particles. As an integral part of the KF Particle Finder package, now the main approach for reconstruction and analysis of short-lived particles in the STAR experiment, the missing mass method will continue to be used for physics analysis in online and offline modes.

It should also be noted that the high quality of the results obtained from the express analysis of data in real time has led to their status as preliminary physics results with the right to present them at international physics conferences and meetings on behalf of the STAR Collaboration.

Purpose of the thesis

The purpose of this thesis was to develop the missing mass method for efficient reconstruction of short-lived particles with neutral particles in their decay products and a set of fast algorithms capable to process data in real time on large computer clusters under conditions of high event multiplicity (up to 10^7 collisions per second) and dominant background.

The structure of the thesis

The thesis consists of eight chapters. The first chapter briefly formulates the goals and objectives of the research, and describes the structure of the dissertation. The second chapter gives a brief introduction to experimental physics of heavy ions and describes the importance of studying strange particles as carrying information about the state and properties of compressed baryonic matter, which is formed during the collision of heavy ions. The third chapter is devoted to a comprehensive description of the detector system and the physics program of the CBM (FAIR/GSI) experiment. The fourth chapter contains a brief discussion of many-core computer architectures and parallel methods for their efficient use. The fifth chapter describes the problem of searching for short-lived particles, as well as the KF Particle and KF Particle Finder packages of algorithms developed for the CBM experiment. The missing mass method, details of its implementation, and results of its application to simulated data in the CBM experiment are discussed in detail in chapter six. Chapter seven briefly describes the STAR (BNL) experiment and its beam-energy scan program BES-II, and presents and discusses the results of applying the missing mass method to real STAR data on the High Level Trigger computer cluster. The conclusion in chapter eight briefly summarizes the results of the dissertation.

Chapter 2

Experimental heavy ion physics

How is the Universe arranged and what are its elementary building blocks? These issues have been of interest to mankind since ancient times first for Greek philosopher-scientists (like the seven spheres of Aristotle (Fig. 2.1), and the atom of Democritus, around 400–300 BC), and then already professional physicists from the end of the 19th century to the modern time (Fig. 2.2).

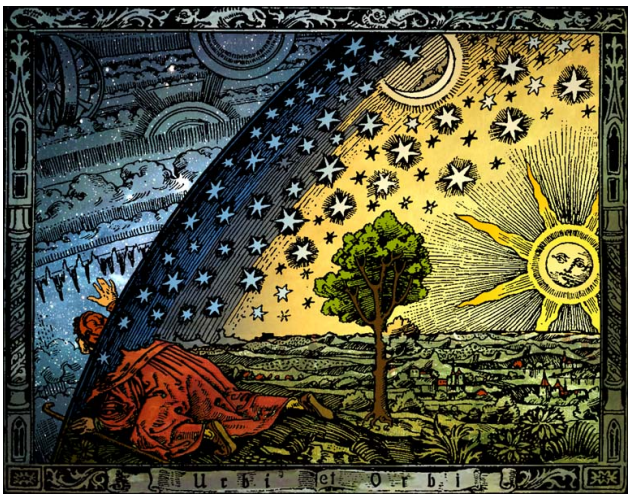

Figure 2.1: Engraving appearing in a book by a 19th century French astronomer-writer C. Flammarion [2].

The study of radioactivity led to the fact that already at the beginning of the 20th century physicists knew about the existence of atoms, electrons and protons. Investigation of the atomic structure gave rise to the emergence of quantum mechanics and the concept of elementary particles, as mathematical objects, which are described by wave functions expressing the probabilistic nature of a particle to be in space and time.

Rutherford proposed a fundamentally new approach to the study of quantum objects by bombarding a target-object with a beam of charged particles. This method then led to the construction of accelerators and the development of detec-

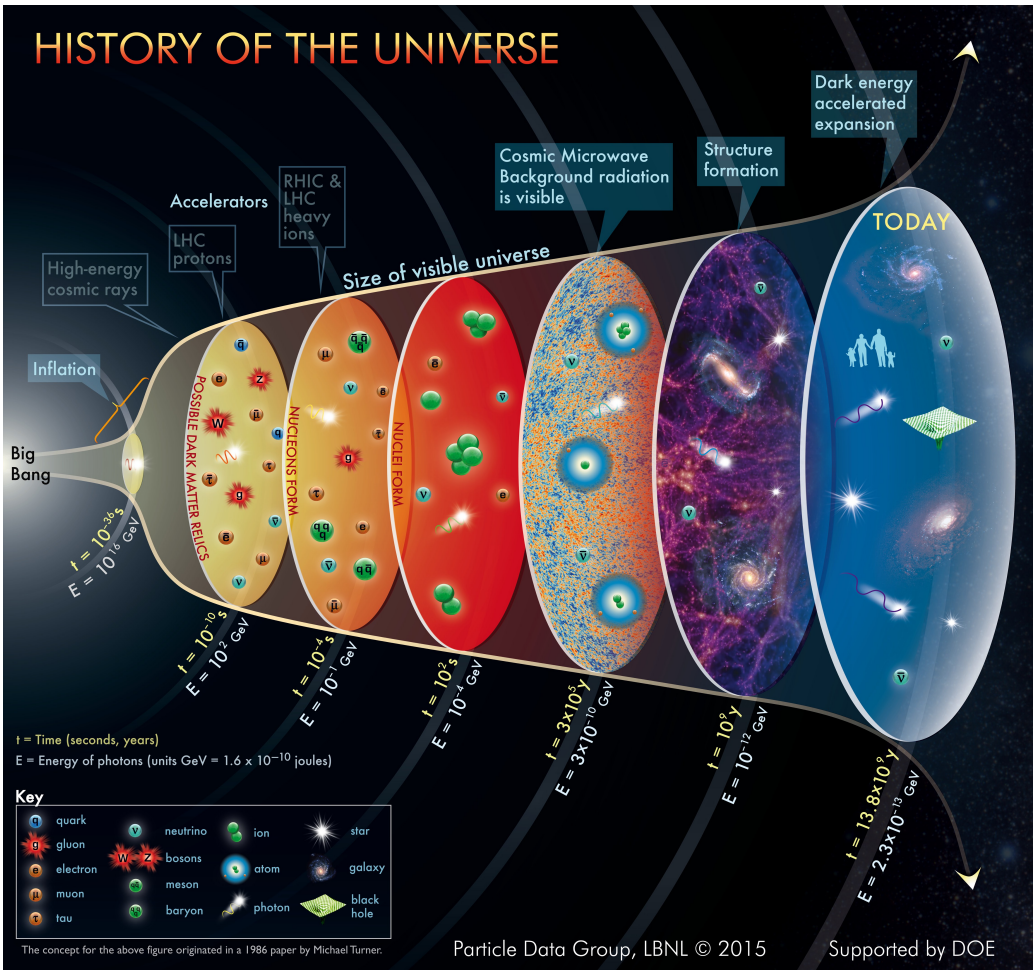

Figure 2.2: Thermal history of the Universe in the Big Bang model, with the Universe expanding and cooling through various phases. In the electroweak stage ($\sim 10^{-15}$ to 10^{-12} sec) the entire Universe is already populated with quarks, leptons, gluons, photons, W, Z and Higgs bosons [1].

tor technologies. This in turn gave rise to the explosive discovery of an increasing number of elementary particles (Fig. 2.3) with the leptons observed as point-like objects, while the hadrons had a size of about 10^{-13} cm.

2.1 Classification of elementary particles

In the mid-1960s, the number of elementary particles was estimated already in dozens, which required work on their analysis and systematization, and the development of theoretical models.

There are several ways to classify the elementary particles [5]. The simplest and

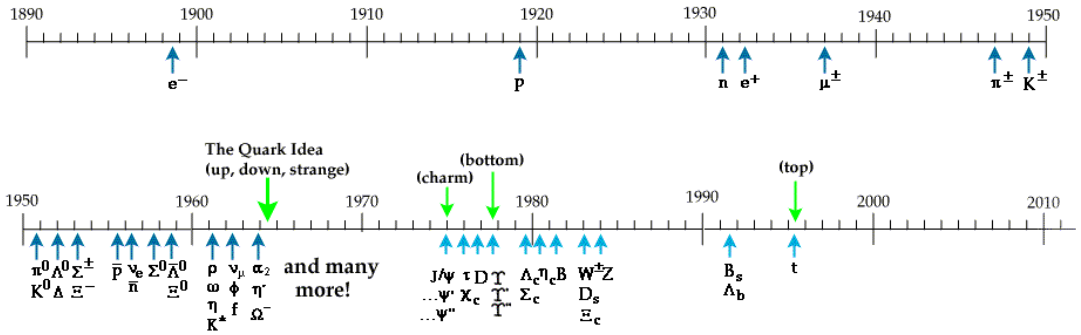

Figure 2.3: A time line of particle discoveries from 1898 to the present [3]. In 2012 a new particle with a mass of 125 GeV was discovered and later confirmed to be the Higgs boson.

historically the first classification of the particles is according to their stability. Unstable particles can be classified according to their lifetime. The number of unstable particles behaves with time as:

$$N = N_0 \exp(-t/\tau), \tag{2.1}$$

where N_0 is the initial number of particles, τ is the lifetime measured at rest and $T_{1/2} = \tau \ln 2 = 0.693 \cdot \tau$ is the half-life time.

Stable particles are: the photon (γ), the electron (e^-) and the positron (e^+), neutrinos and anti-neutrinos, the proton (p) and the anti-proton ($\bar{p}$).

Particles with lifetimes longer than about 10^{-8} s are considered to be almost stable since they can be registered in detector systems.

Particles with lifetimes ranging from 10^{-6} to 10^{-12} s decay via the *weak interaction*. This group includes the $\mu^{\pm}$, $\tau^{\pm}$, the d, s, c and b quarks and the $\pi^{\pm}$, $K^{\pm}$, K^0, $\bar{K}^0$, Λ^0, $\Sigma^{\pm}$, Ξ^-, D, Λ_c, B and other hadrons.

Particles with lifetimes ranging from 10^{-16} to 10^{-20} s decay via the *electromagnetic interaction*, for instance, the hadrons π^0, η^0, Σ^0.

Hadrons with lifetimes of the order of 10^{-23} s decay via the *strong interaction*, the so-called resonances ρ, ω, K^*, N^*, Λ, Y^*, etc.

The mediators of the weak interaction, $W^{\pm}$ and Z^0 bosons have very short lifetimes of the order of 10^{-25} s due to their large masses with respect to the relatively small mass of the final state particles.

Another important classification (Fig. 2.4) can be done according to the spin, the intrinsic angular momentum of the particles. Elementary particles are classified in *fermions* and *bosons* depending on whether they have semi-integer or integer spin. Fermions follow the Fermi-Dirac statistics and the Pauli exclusion principle. Bosons follow the Bose-Einstein statistics with possibility to have the

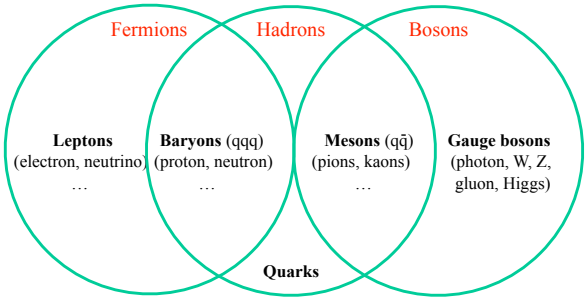

Figure 2.4: A simple classification of elementary particles according to their spin.

same quantum numbers. Fermions are divided into leptons, which are not subject to the strong interaction, and baryons, which feel the strong interaction. Bosons are divided into mesons, which are hadrons, and fundamental bosons, mediators of interactions.

One more classification is based on the conservation of the baryon number, that means that a baryon cannot decay into a system without baryons and, therefore, an unstable baryon after a series of decays, ends up as the lightest baryon, that is, a proton, which is a stable particle. The conservation of the lepton number prohibits the conversion of leptons into bosons or baryons. There are three types of lepton numbers, corresponding to the three lepton families, the electron, muonic and tau lepton numbers, that are conserved. Other quantum numbers are related to approximate conservation principles and conserved only in electromagnetic and strong interactions.

There was another very productive attempt to classify the hadrons by sorting them into multiplets. In that way each multiplet of one to four particles had particles with roughly the same mass and are identical in all other aspect except the electric charge, for example, a doublet of the proton and the neutron. Later multiplets were expanded to super-multiplets. There were eight different quantum numbers within these super-multiplets, so-called the "eightfold way" classification. It became clear with time that the eightfold way is a form of the Lie group SU(3). The super-multiplets led in 1964 to the quark hypothesis by Gell-Mann and Zweig. There were proposed three different quarks, u, d and s (and antiquarks), which formed all types of hadrons known at the time: the mesons made of a quark and an antiquark and the baryons made of three quarks.

2.2 The Standard Model (SM)

Currently, the most recognized theoretical model is the Standard Model (SM) of particles and interactions (Fig. 2.5) that is based on the principles of local gauge invariance, i.e. invariance of the equations of motion to arbitrary changes in the coordinates of space-time.

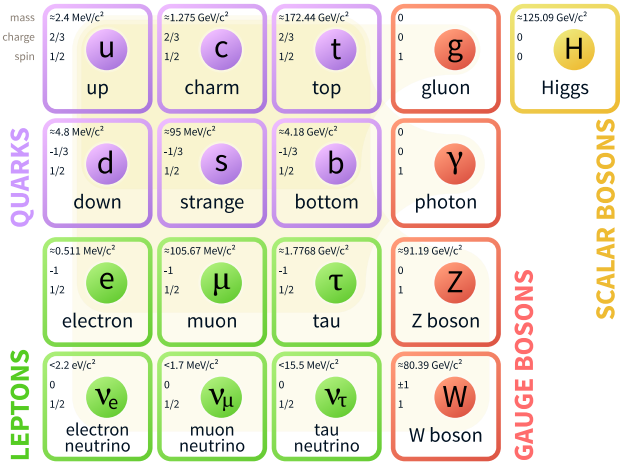

Figure 2.5: The Standard Model of elementary particles with the three generations of matter, gauge bosons in the fourth column, and the Higgs boson in the fifth [4]. The values in the upper left corner of each box are the mass, electrical charge and spin of the particle.

The Standard Model describes the electromagnetic, weak and strong interactions of all elementary particles [5]. The Standard Model does not consider the gravitational interaction, since its effect is negligible at the sub-atomic level. The Standard Model of particle physics is based on the quantum electrodynamics, the quantum chromodynamics, and the quark-parton model. The quantum electrodynamics (QED) describes processes that occur under the action of electromagnetic forces, which are studied with a high accuracy. The quantum chromodynamics (QCD) describes the processes of strong interactions and is constructed by analogy with QED, but to a greater extent is a semi-empirical model. The quark-parton model combines the theoretical and experimental results of studies of the properties of particles and their interactions. The Standard Model has external parameters, such as the masses of leptons and quarks.

The Standard Model postulates the existence of 12 fundamental quantum fields of spin 1/2 whose quanta are fundamental fermion particles that can be combined into three generations of fermions: 6 leptons (electron e^-, muon μ^-, tau lepton τ^-, electron neutrino ν_e, muon neutrino ν_μ and tau ν_τ neutrinos), 6 quarks (u, d, s, c, b, t) and 12 antiparticles corresponding to them.

Quarks participate in strong, weak, and electromagnetic interactions; charged leptons (electron, muon, tau-lepton) — in weak and electromagnetic; neutrinos — only in weak interactions. All three types of interactions arise as a consequence of symmetry with respect to the three types of gauge transformations. The interaction particles are the bosons: 8 gluons for strong interaction (symmetry group SU(3)); 3 heavy gauge bosons (W^+, W^-, Z^0) for weak interaction (symmetry group SU(2)); one photon for electromagnetic interaction (symmetry group U(1)). Unlike the electromagnetic and strong, a weak interaction can mix fermions from different generations, which leads to instability of all particles, except for the lightest ones, and to such effects as violation of CP-invariance and neutrino oscillations. The mass of the particles is generated by the scalar field of

Higgs bosons.

Table 2.1: Selected baryons and mesons, including their quark content and masses [6].

Baryon	Quark content	Mass (GeV)	Meson	Quark content	Mass (GeV)
p	uud	0.938	π^+	$u\bar{d}$	0.140
n	udd	0.939	K^0	$d\bar{s}$	0.498
Λ	uds	1.116	K^+	$u\bar{s}$	0.494
Σ^-	dds	1.197	ϕ	$s\bar{s}$	1.020
Ξ^0	uss	1.315	D^0	$c\bar{u}$	1.864
Ω^-	sss	1.672	D^+	$c\bar{d}$	1.869
Λ_c^+	udc	2.285	D_s^+	$c\bar{s}$	1.968
Σ_c^{++}	uuc	2.452	J/ψ	$c\bar{c}$	3.097
Ξ_c^+	usc	2.466	B^0	$d\bar{b}$	5.279
Ω_c	ssc	2.698	B^+	$u\bar{b}$	5.279
Ξ_{cc}^+	dcc	—	B_s^0	$s\bar{b}$	5.370
Λ_b	udb	5.624	Υ	$b\bar{b}$	9.460

At normal nuclear densities and temperatures quarks together with gluons are bound into hadrons, which are known as baryons with three quarks (the proton $|p\rangle = |uud\rangle$ and neutron $|n\rangle = |udd\rangle$) and mesons with a quark-antiquark pair (the pion $|\pi^-\rangle = |d\bar{u}\rangle$ and kaon $|K^-\rangle = |s\bar{u}\rangle$), some of them are listed in Tab. 2.1 together their quark content and masses. Manifesting the SU(3) symmetry of the strong interaction baryon and meson form multiplets as shown in Fig. 2.6 together with the quark structure of the particles. The multiplets demonstrate the approximate flavor symmetry between the up, down and strange quarks.

The quark model in its simplest form is not complete, since the Pauli principle excludes the presence of a spin 3/2 in an Δ^{++} isobar with a quark composition $|\Delta^{++}\rangle = |uuu\rangle$. Therefore, it was necessary to postulate the presence of quarks and antiquarks of an additional quantum number called color. Quarks can exist in three different color states, called red, green, blue. Color here are treated like an electric charge in electrodynamics.

Quarks are fermions with spin 1/2; gluons are bosons with spin 1. Quarks are classified according to two characteristics: aroma and color. There are 6 quark flavors and 3 colors for each quark. Aroma is a characteristic that is conserved in strong interactions. Gluon is made up of two colors — color and anti-color, and all other quantum numbers are zero. When a gluon is emitted, the quark changes color, but not the aroma. There are 8 gluons in total.

While demonstrating the success in hadron classification, QCD being constructed by analogy with QED, however, experiences difficulties using methods developed for QED. In contrast to the electromagnetic coupling constant

$$\alpha = e^2/\hbar c = 1/137, \tag{2.2}$$

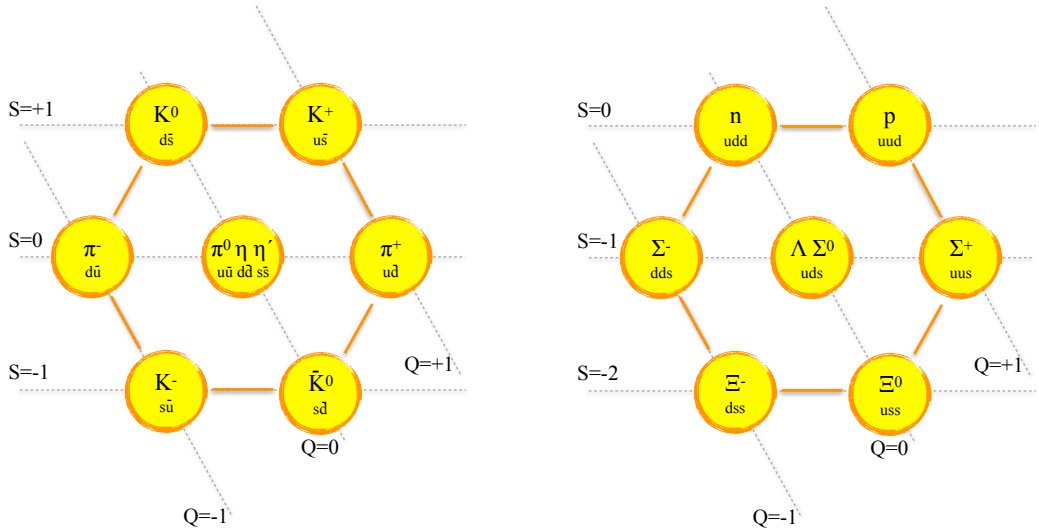

Figure 2.6: The lowest SU(3) meson and baryon multiplets together with the quark structure of particles: (left) the pseudo-scalar nonet of mesons with spin 0 and (right) the baryon octet with spin 1/2.

the QCD coupling constant of strong interaction α_s might be of the order of one and depends on the momentum Q^2 transferred in the interaction and has an inverse logarithmic decrease with increasing the transferred momentum Q^2:

$$\alpha_s(Q^2) \propto \frac{1}{\ln(Q^2/\Lambda^2)} \tag{2.3}$$

with Λ — a scale constant.

For large values of the transferred momentum Q^2 (*hard* spectrum), the α_s coupling constant is small and the QED perturbation approach is valid, on the other hand, for small transferred momenta Q^2 (*soft* spectrum) only very complicated numerical methods of (lattice) QCD can be applied. Thus, the perturbation approach can be applied only up to the distances of about one order smaller than the nucleon radius, whereas already to describe the nucleon the lattice QCD methods should be used.

The Lagrangian in QED has a form [7]:

$$\mathcal{L}_{\text{QED}} = -\frac{1}{4}F_{\mu\nu}^2 \tag{2.4}$$

with

$$F_{\mu\nu} = \partial_\mu A_\nu - \partial_\nu A_\mu, \tag{2.5}$$

where A_μ is the vector potential of the electromagnetic photon field. The anti-symmetric 4×4 tensor $F_{\mu\nu}$ contains components of the electric and magnetic fields.

The Lagrangian in QCD with gluons only is:

$$\mathcal{L}_0 = -\frac{1}{4}\sum_a F^a_{\mu\nu}F^{\mu\nu\,a} \tag{2.6}$$

with $a = 1, 2, ..., 8$ color indices, and

$$F^a_{\mu\nu} = \partial_\mu A^a_\nu - \partial_\nu A^a_\mu + [A_\mu, A_\mu]^a, \tag{2.7}$$

where A^a_μ are the eight vector potentials of the gluon field, and g_s is the strong color charge. The last term in square brackets represents self-interaction of gluons, since they, in contrast to the photon, have non-zero charge.

The QCD Lagrangian has also additional terms related to quarks that describe interactions of quarks and gluons, and the self-interaction fo quarks:

$$\mathcal{L}_{\mathrm{QCD}} = \mathcal{L}_0 + i\sum_q \bar{\psi}^i_q \gamma^\mu (D_\mu)_{ij}\psi^j_q - \sum_q m_q \bar{\psi}^i_q \psi_{q\,i} \tag{2.8}$$

with

$$(D_\mu)_{ij} = \delta_{ij}\partial_\mu + i\frac{g_s}{2}\sum_a \lambda^a_{i,j}A^a_\mu, \tag{2.9}$$

where ψ^i_q are the four-component Dirac spinors describing quark fields of color i and flavor q and the (3×3) matrices $\lambda_{i,j}$ are the representations of the SU(3) group.

The coupling constant α_s is related to the color charge

$$\alpha_s = \frac{g_s^4}{4\pi}. \tag{2.10}$$

The full expression for α_s is:

$$\alpha_s(Q^2) = \frac{12\pi}{(33 - 2n_f)\ln(Q^2/\Lambda^2)}(1 + \text{higher logarithmic terms}), \tag{2.11}$$

where n_f is the number of quark flavors. The strong coupling strength α_s is the only free parameter in the QCD Lagrangian and is determined from experimental measurements. According to the generally adopted convention one defines the value of α_s at the mass of the Z^0 boson to be $\alpha_{m_Z} = 0.118 \pm 0.002$. This gives for the scale constant the value $\Lambda = 217^{+25}_{-23}$ MeV [7].

There are attractive forces between quarks that have two properties: asymptotic freedom at very small distances; and confinement, because the potential interaction energy $V(r)$ increases indefinitely with increasing distance r between quarks (Fig. 2.7). The increase of the interaction strength for a $q\bar{q}$ pair can be approximated by the Cornell potential

$$V(r) = -\frac{4\alpha_s}{3r} + kr, \tag{2.12}$$

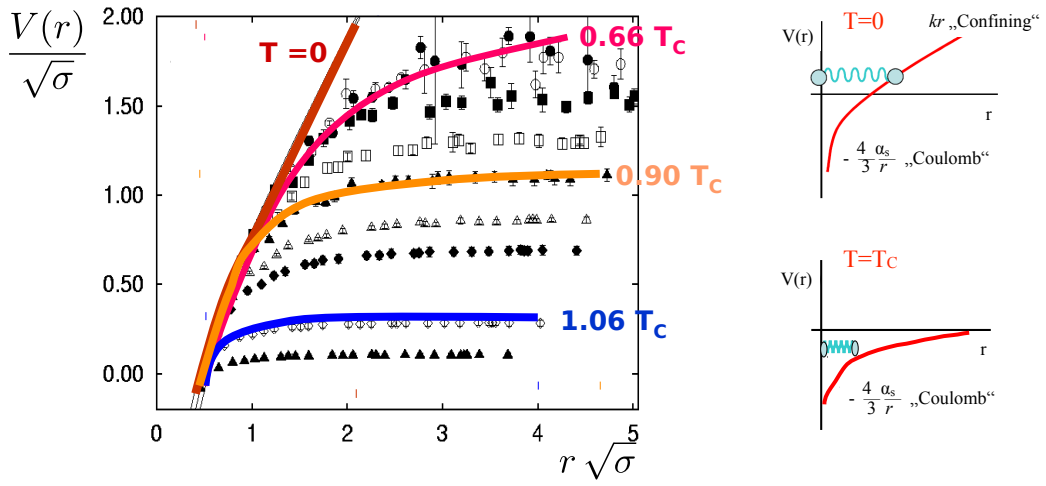

Figure 2.7: Confinement is explained by the increase of the interaction strength for a $q\bar{q}$ pair in the Cornell potential $V(r) = -(4/3)(\alpha_s/r) + kr$, where α_s is the coupling strength of strong interaction and k parametrizes the effects of confinement. A lattice QCD calculation for a heavy quark pair exhibits screening of long range confining potential with increasing the temperature over the critical temperature T_C [8, 9].

where r is the distance between quarks, and k is the string constant effecting confinement.

At shorter distances and/or at large transfer four-momentum Q^2 the coupling strength α_s becomes smaller, therefore at small distances and/or at large energies quarks behave like free particles. This effect is known as the asymptotic freedom.

When the distance r between quarks increases, the interacting color field can be represented as a tube connecting the $q\bar{q}$ pair, and at large distances it become energetically favorable to convert the stored energy into a new $q\bar{q}$ pair. Confinement cannot be described perturbatively, but with simple bag models or more accurately with lattice QCD.

The confinement property is inherent in QCD at ordinary temperatures and densities of nuclear matter. However, in collisions of relativistic heavy ions, one can create conditions, when QCD matter will lose the confinement properties, and quarks and gluons will become capable of propagating over distances larger than 1 fm.

The quarks confined in the proton acquire dynamically an additional mass ($\sim$ 350 MeV) through the confining effect of strong interactions, since $M_p \approx$ 938 MeV, but $m_u + m_u + m_d = 10 \div 15$ MeV. It is expected that deconfinement will result in a restoration of the "bare" values of the quarks masses, which they have in the QCD Lagrangian: $m_u \approx 2.4$ MeV, $m_d \approx 4.8$ MeV. This effect is usually referred to as "partial restoration of chiral symmetry". In the chiral symmetry fermions and anti-fermions have opposite helicity. The symmetry is exact

only for massless particles, therefore its restoration for the quarks with small masses is only partial.

In QCD, the dynamics of the system is determined by the response of the vacuum to the presence of a test charge. The principle of uncertainty in quantum theory allows the existence of pairs of antiparticle particles during a time inversely proportional to their energy. The presence of a quark condensate ($q\bar{q}$) in the QCD vacuum is a signal of spontaneous breaking of chiral symmetry, since the relation

$$\langle q\bar{q}\rangle = \langle q_L\bar{q}_R\rangle + \langle q_R\bar{q}_L\rangle \tag{2.13}$$

means that left and right quarks and antiquarks can be transformed into each other. The quark condensate can be used as an order parameter in QCD. Calculations on the space-time lattice show that in the phase transition of deconfinement the quark condensate tends to zero, signaling the restoration of chiral symmetry.

2.3 The QCD phase diagram

A first description of high energy hadronic and nuclear collisions was proposed by Fermi [11, 12] in 1950 in terms of the statistical thermal model with formation of a highly excited, but thermally equilibrated fireball, which decays into particles according to the statistical rules.

A hydrodynamical expansion of the fireball with the subsequent cooling down process of the system until it reaches the freeze-out temperature of the order of the pion mass was first discussed by Landau [13] in 1953.

Later Hagedorn [14] in 1965 has proposed to describe such multi-hadron state of matter by thermodynamics with a limiting temperature, now quoted as the Hagedorn temperature, which is again of the order of the pion mass and is equal to about 160 MeV.

In 1975 Cabibbo and Parisi [15] idetified the limiting Hagedorn temperature with the temperature of the phase transition from the hadronic stage to the stage of the quark matter and discussed for the first time the QCD phase diagram at finite baryon densities and temperatures as illustrated in Fig. 2.8 in its current state of knowledge.

As it was discussed in the previous section, the quark matter may exist in different states. At low temperatures and densities, quarks are confined into hadrons, at high temperatures and densities of the matter the state with free quarks is called Quark-Gluon Plasma (QGP). The quark gluon plasma [17, 18] is a (locally) thermally equilibrated state of matter in which quarks and gluons are deconfined from hadrons, so that color degrees of freedom become manifest over nuclear, rather than merely nucleonic, volumes. The QGP state is believed to exist in the

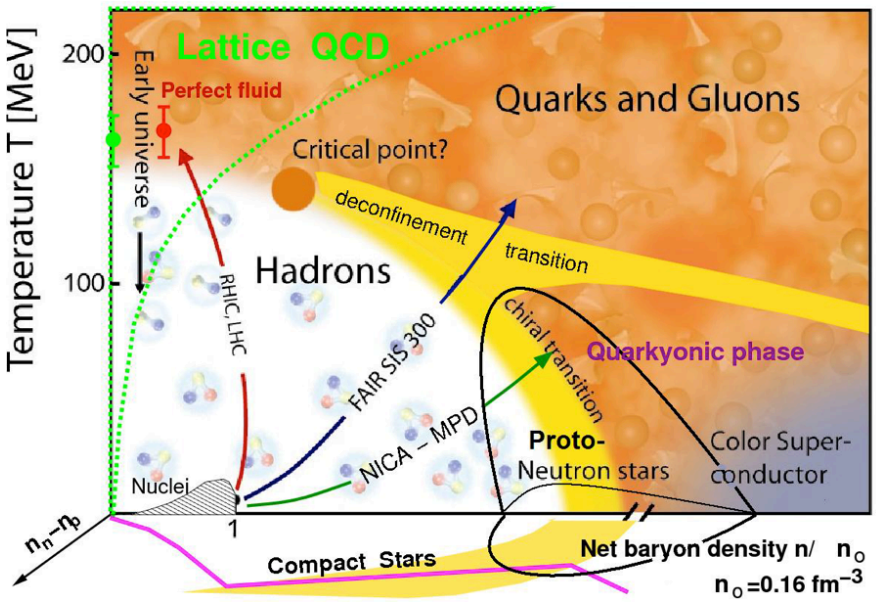

Figure 2.8: The QCD phase diagram of hadronic and partonic matter as a function of temperature and net baryon density [16].

early Universe about 10^{-6} second after the Big Bang. Current lattice QCD calculations show that the transition happens around the critical temperature T_C = 150–180 MeV, which corresponds to an energy density of about 0.3–1.0 GeV/fm^3.

With the pure gluon medium and with massless quarks of two (u, d) or three (u, d, s) flavors the calculations predict the phase transition of the first-order with a step-like increase of the energy density at the critical temperature, thus indicating the phase transition. This reflects a jump in the number of degrees of freedom from 3 for a (pure pion) hadron gas to 37 for a two-flavor quark-gluon plasma.

The calculations predict also existence of the critical point with the second-order continuous transition, so-called *cross-over*, when there is no sharp change of the medium parameters indicating this type of the phase transition and, therefore, hard to be measured.

The QGP state can exist also at low temperatures and at very high baryon densities, similar to the core of neutron stars. Even further, at low temperatures and extremely high densities quarks and gluons form a superconductor state of matter.

Let us analyse the QCD phase diagram more quantitatively [8, 19, 20, 21] and consider a two-phase system of particles consisting of π-mesons, u- and d-quarks (and antiquarks), and gluons. The thermodynamic variables in the system are: temperature T, baryonic chemical potential μ, and volume V. In the gas approximation, when describing the hadronic gas, as well as the quark-gluon plasma,

we will for simplicity neglect the interaction between the particles. The energy difference in the ground state of the quark-gluon plasma and hadronic gas is determined by introducing the phenomenological constant B, the numerical value of which is known in the bag model [8, 20, 21]. We first consider the two limiting cases $\mu = 0$ and $T = 0$.

At zero chemical potential and low temperatures, the hadronic system will be in the state of a pion gas. The pressure and the energy density of such a gas ($p = \varepsilon/3$) are determined by the formulas of a relativistic gas of noninteracting massless bosons:

$$p_H(T, \mu = 0) = \frac{\pi^2}{90} g_H T^4, \quad \varepsilon_H(T, \mu = 0) = \frac{\pi^2}{30} g_H T^4, \tag{2.14}$$

where $g_H = 3$ taking into account the three charge states of the pion.

At high temperatures, the formation of a quark-gluon plasma (QGP) is expected. The QGP pressure and the energy density are determined by the sum of the relativistic gluon Bose gas and the quark Fermi gas:

$$p_Q(T, \mu = 0) = \frac{\pi^2}{90} g_Q T^4 - B, \quad \varepsilon_Q(T, \mu = 0) = \frac{\pi^2}{30} g_Q T^4 + B, \tag{2.15}$$

with a negative vacuum pressure accounting in the parameter B and $g_Q = (2 \times 8 + \frac{7}{8} \times 2 \times 2 \times 2 \times 3) = 37$ takes into account the spin and color states of gluons, quarks, and antiquarks. The factor (7/8) accounts difference in the normalization of Boltzmann and Fermi distribution functions.

The condition that the pressures of the two phases (hadronic and QGP) are equal

$$p_H(T = T_C, \mu = 0) = p_Q(T = T_C, \mu = 0) \tag{2.16}$$

allows us to find the critical temperature:

$$T_C = \left(\frac{45}{17\pi^2} B \right)^{1/4} \approx 0.72 \cdot B^{1/4} \approx 140 \text{ MeV} \tag{2.17}$$

with $B \approx 0.17$ GeV/fm^3 from the bag model.

At the critical temperature $T_C \approx 140$ MeV, the hadron phase transition to the quark-gluon plasma occurs. This is a first-order phase transition, since the energy density experiences a jump at the critical point:

$$\varepsilon_Q(T_C, \mu = 0) - \varepsilon_H(T_C, \mu = 0) = 4B. \tag{2.18}$$

The critical value of the energy density

$$\varepsilon_C = \frac{3 g_H}{g_Q - g_H} B = \frac{9}{34} B = 0.045 \text{ GeV/fm}^3. \tag{2.19}$$

Therefore, at energy densities exceeding

$$\varepsilon = \varepsilon_C + 4B = 0.73 \text{ GeV/fm}^3, \tag{2.20}$$

the hadronic matter is in the phase of a quark-gluon plasma.

Summarizing, at temperatures above the critical temperature $T_C \approx 140$ MeV, the hadronic matter is in the phase of a quark-gluon plasma with the energy density $\varepsilon > 0.73$ GeV/fm^3.

Let us consider another limiting case of the model — zero temperatures and a nonzero baryon chemical potential $\mu = 3\mu_Q$, where μ_Q is the quark chemical potential. Then in the hadronic phase there is a degenerate Fermi gas of baryons with the pressure and the energy density, respectively:

$$p_H(T = 0, \mu_Q) = \frac{\mu_Q^4}{6\pi^2}, \quad \varepsilon_H(T = 0, \mu_Q) = \frac{\mu_Q^4}{2\pi^2}, \tag{2.21}$$

and the baryon density equal

$$n_B = \frac{2\mu_Q^3}{2\pi^2}. \tag{2.22}$$

At high densities, the system is in the phase of a quark-gluon plasma with the pressure and the energy density:

$$p_Q(T = 0, \mu_Q) = \frac{\mu_Q^4}{2\pi^2} - B, \quad \varepsilon_Q(T = 0, \mu_Q) = \frac{3\mu_Q^4}{2\pi^2} + B. \tag{2.23}$$

From the equilibrium condition $p_H(0, \mu_C) = p_Q(0, \mu_C)$ we obtain the critical value of the chemical potential

$$\mu_C = 3(3\pi^2 B)^{1/4} \approx 7 \cdot B^{1/4}. \tag{2.24}$$

The critical baryon density in this case

$$n_C = 2(3\pi^2)^{1/4} B^{3/4} \approx 0.86 \cdot B^{3/4} \approx 5n_0, \tag{2.25}$$

where $n_0 = 0.17$ nucleons/fm^3 is a normal nuclear density.

A more accurate study of the hadron gas model for arbitrary temperatures and chemical potentials leads to the phase diagram shown in Fig. 2.8. As can be seen from the figure, there are several experimental possibilities to form of a quark-gluon plasma in collisions of relativistic heavy ions:

- by raising the temperature of the hadronic medium;
- by increasing the baryon density;
- a combination of these factors.

2.4 The Quark-Gluon Plasma (QGP) in laboratory

Investigations of the heavy ion collisions have been initiated in the early 1970-ies at the Lawrence Berkeley National Laboratory (LBNL) in Berkeley and at the Joint Institute for Nuclear Research (JINR) in Dubna, when light nuclei were first time accelerated to the few GeV per nucleon energies using their proton synchrotrons. The Bevatron in Berkeley used the linear accelerator SuperHilac as an injector to pre-accelerate heavy elements. The combined facility, the Bevalac, has achieved the energies of 1–2 GeV per nucleon. Similarly the syncrophasotron in Dubna was converted to accelerate heavy ions.

The idea to create the Quark-Gluon Plasma (QGP) in laboratory in heavy ion collisions was first discussed in 1974 [22] followed by the pioneering work on the Bevalac accelerator at LBNL and later on other accelerating facilities at BNL, CERN and GSI.

The heavy ion collisions are characterized by the beam energy, colliding heavy ions, and the impact parameter b. The impact parameter b is a distance between the centers of the two nuclei, thus representing an overlapping region of the colliding nuclei. The multiplicity of particles produced in a heavy ion collision is directly related to the impact parameter. The centrality is the percentile of the multiplicity distribution, for example, 0–5% centrality contains the most central collisions and corresponds to an impact parameter less than 3.5 fm. A fireball of strongly interacting quantum chromodynamics matter is usually created from the participant nucleons in the central and semi-central collisions.

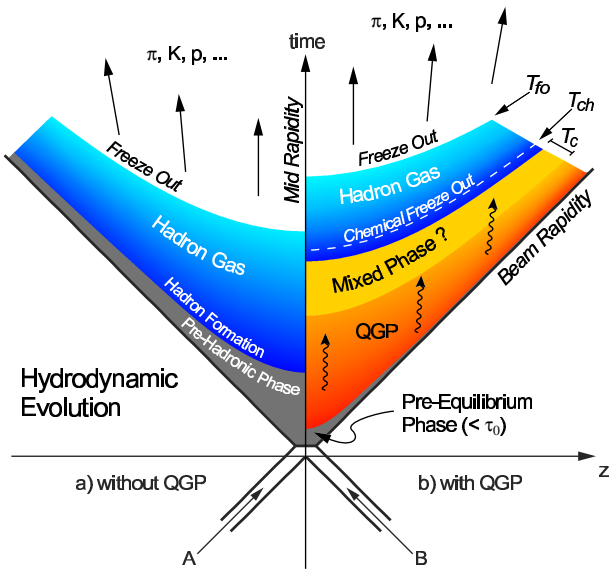

Figure 2.9: Schematic space-time representation of stages of the evolution of nuclear matter: the initial non-equilibrium state, the phase of the equilibrium quark-gluon plasma, the mixed phase of quarks, gluons and hadrons, hadronic gas and, finally, noninteracting secondary hadrons. At low energies the QGP phase is not formed.

Let us consider the space-time evolution of hadron-hadron and heavy ion collisions [19] as represented in Fig. 2.9 using the light-cone variables (z, t).

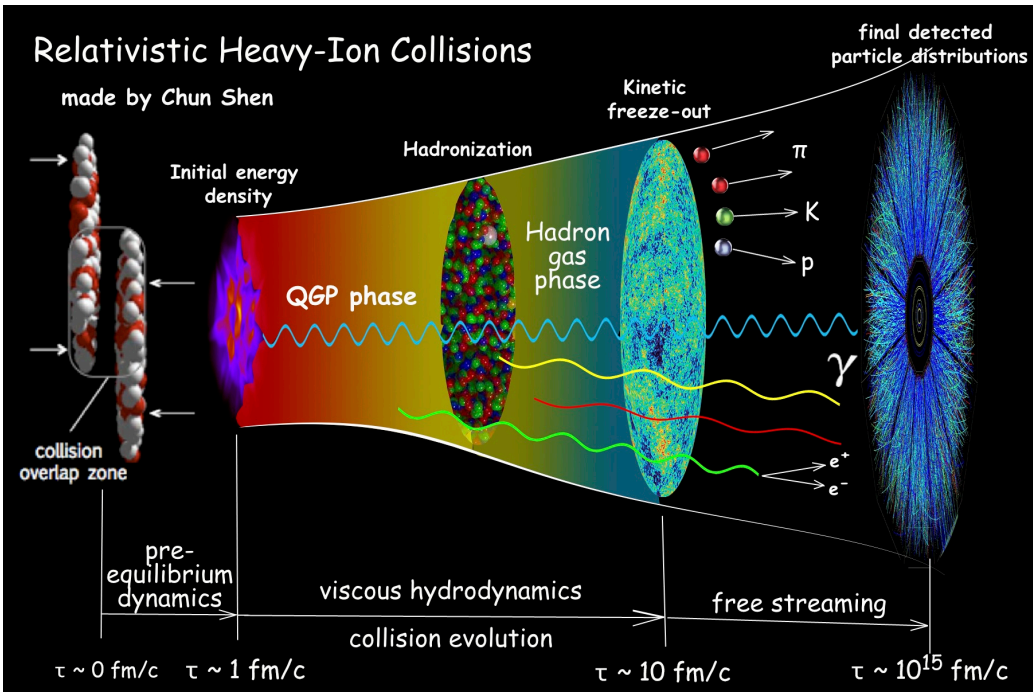

Figure 2.10: Schematic detector representation of stages of the evolution of nuclear matter: the initial non-equilibrium state, the phase of the equilibrium quark-gluon plasma, the mixed phase of quarks, gluons and hadrons, hadronic gas and, finally, noninteracting secondary hadrons.

Within the framework of the parton structure of hadrons, their interaction (e.g. in *pp* collisions) at high energies occurs as follows. Before the interaction, the relativistic hadrons are ensembles of partons (valence and sea quarks, antiquarks and gluons) distributed over the hadron momentum fraction transferred by the partons. As a result of the hadron-hadron interaction, part of the fastest partons do not participate in collective interactions and form the leading secondary hadrons. The relatively slow partons of the colliding nuclei interact with each other, forming a quark-gluon system, whose evolution leads to the formation of a soft part of the spectrum of secondary hadrons. Under certain circumstances, multiple parton-parton interactions can create conditions for establishing thermodynamic equilibrium at the initial temperature T_i. The subsequent evolution (expansion) develops according to the laws of hydro- and thermodynamics, the temperature of the system falls. At the final stage of evolution, the temperature decreases such that the system forms noninteracting hadrons.

The space-time and detector evolution of central collisions of heavy nuclei at RHIC or LHC energies looks as follows (Fig. 2.9 and Fig. 2.10,). At the initial time in the nucleon-nucleon collisions of two Lorentz compressed nuclei (with a thickness of $\sim$ 1 fm), partons (quarks and gluons) interact, leading to multiple production of quarks, antiquarks, and gluons. The generated quarks and

gluons, in turn, interact with each other and with partons already existing in the colliding nuclei. It is assumed that multiple parton-parton interactions can lead to the establishment of local thermodynamic equilibrium in the quark-gluon system at a temperature of T_i. If the initial temperature is higher than the temperature of the phase transition ($T_i > T_C$), then the system is in the state of a quark-gluon plasma. The QGP then expands, the temperature decreases and reaches the critical temperature T_C. In case of a first-order phase transition the nuclear matter spends some time in a state of a mixed phase in which quarks, antiquarks, gluons, and hadrons coexist. In this state, the quark degrees of freedom are transformed into hadronic ones until the chemical freeze out happens. Finally, the system expands and, after reaching the kinetic freeze out, decays into noninteracting particles, which then are registered in a detector system.

Use of the Glauber model to describe the initial stage, the perfect-fluid hydrodynamics for the quark-gluon plasma and the kinetic simulations of the freeze-out process is a well-established model of ultra-relativistic heavy ion collisions.

Soft hadrons, i.e. the hadrons with relatively small transverse momenta with respect to the collision axis, constitute more than 90% of the produced particles and carry the information about the bulk properties of the very hot and dense stage of the matter, the quark-gluon plasma.

Since heavy quarks, i.e. charm and beauty, are mainly produced via the gluon fusion in hard scattering processes at the initial stage and exist during the entire evolution of the system, they are sensitive probes to study the medium properties of the strongly interacting matter created in heavy ion collisions.

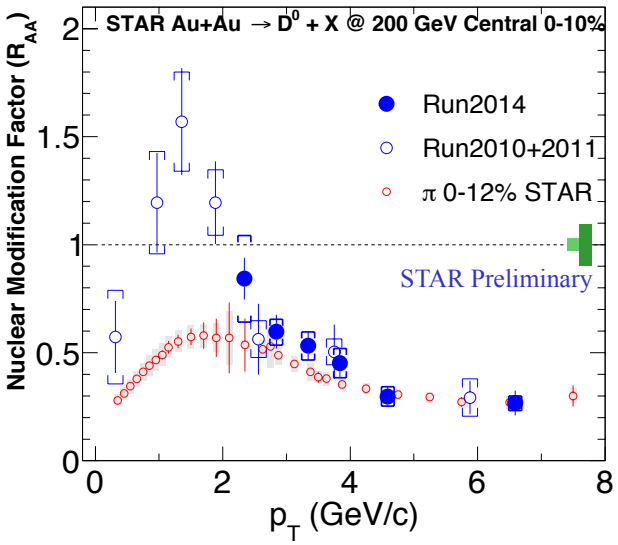

Figure 2.11: The nuclear modification factor R_{AA} of D^0 meson in Au+Au collisions at $\sqrt{s_{NN}} = 200$ GeV in the STAR experiment [24]. A large suppression is observed at high p_T due to energy loss and strong charm-medium interaction. The enhancement at $p_T \sim 0.7$–2 GeV/c is described by models with coalescence of charm and light quarks.

The heavy quarks traversing the medium lose energy via collisional (scattering of the heavy quark with light quarks) and radiative (gluon radiation) processes. The in-medium energy loss of heavy quarks can be investigated by measuring the

nuclear modification factor (R_{AA}) of heavy-flavor particles, which is defined as a ratio of the transverse momentum (p_T) differential yield of particles in heavy ion collisions (dN_{AA}/dp_T) with respect to the pp collisions (dN_{pp}/dp_T) scaled with the average number of binary collisions (the average nuclear overlap function) in heavy ion collisions $\langle N_{coll}\rangle$:

$$R_{AA} = \frac{dN_{AA}/dp_T}{\langle N_{\rm coll}\rangle\, dN_{pp}/dp_T}. \tag{2.26}$$

Alternatively, when the reference pp data are not known, one can consider the production ratio R_{CP} of hadronic species, observed in central collisions relative to peripheral ones.

The average number of binary collisions $\langle N_{\rm coll}\rangle$ is usually estimated from the Glauber model [23]. The model considers all nucleons in each nucleus as hard spheres distributed according to the nuclear density function, e.g. the Saxon-Woods density distribution

$$\rho(r) = \rho_0/(1 + e^{(r-R)/z}) \tag{2.27}$$

with the density in the central plateau region ρ_0, the mean electromagnetic radius R at $\rho(r) = 0.5\rho_0$ and the thickness of the surface layer z. The nucleons are considered as free particles without internal motion inside the nucleus and, therefore, they move along parallel straight lines, interacting with the nucleons of the other nucleus with the probability equal to the cross section, which is known from the elementary collisions. From such geometrical considerations one gets the number $N_{\rm part}$ of the nucleons participated in the collision and the number of subsequent collisions $N_{\rm coll}$. By averaging over an unbiased sample of collisions one can obtain the required average number of binary collisions $\langle N_{\rm coll}\rangle$.

In absence of nuclear effects, R_{AA} is expected to be unity, since the heavy ion collision in that case is just a superposition of nucleon-nucleon collisions with incoherent fragmentation (Fig. 2.9, a). The energy loss of heavy flavors in the quark-gluon medium due to collisional or radiative processes, on the other hand, causes a shift of the transverse momentum distribution towards lower values, that results in a suppression of heavy-flavor particle yields $R_{AA} < 1$ at intermediate and high p_T momenta.

Fig. 2.11 represents the measurements of the nuclear modification factor R_{AA} of $D^0(c\bar{u})$ meson in Au+Au collisions at $\sqrt{s}_{NN} = 200$ GeV in the STAR experiment [24]. Since open heavy flavor hadrons have very short lifetimes ($c\tau_{D^0} = 122.9$ μm), they can not be registered directly in the detector system, but instead are reconstructed from their decay products, like in the $D^0 \to K^-\pi^+$ hadronic decay channel with registered K^- and π^+. As one can see, the R_{AA} is suppressed at high p_T transverse momenta and is comparable with R_{AA} measurements for light hadrons (π). The enhancement of R_{AA} for D^0 at $p_T \sim 0.7$–2 GeV/c

is described by theoretical models with coalescence of charm and light quarks in the medium.

2.5 Strangeness enhancement in QGP

One of the first signatures of the QGP was the strangeness enhancement [25, 26] observed as an increased production ratio R_{AA} of strange hadrons in heavy ion collisions with respect to pp collisions.

Since colliding nuclei are composed only of u and d quarks, the initial strangeness content is very small and there is no net strangeness, and, therefore any strange quarks or antiquarks observed experimentally are created in the collision. Originally, it was proposed that strangeness production would increase in QGP due to the high production rate of $gg \to s\bar{s}$, a process absent in the hadronic state. The subsequent hadronization of these $s\bar{s}$ quarks results in a significant increase in strange particle production. In addition, as mentioned above, the transition from ordinary baryonic matter to the QGP state is expected to result in a restoration of the chiral symmetry, such that the threshold energy of the $s\bar{s}$-pair production should be much lower than in hadronic collisions. Therefore, the production ratio R_{AA} of hyperons and anti-hyperons should be larger in heavy ion collisions relative to pp collisions. This effect is called strangeness enhancement.

The strangeness enhancement in a baryon rich matter can also be a result of the Pauli principle: suppression of $u\bar{u}$ and $d\bar{d}$ pair production in favor of $s\bar{s}$ pairs in initial u and d-rich environment remaining from incident nuclei. Furthermore, the $\bar{u}$ and $\bar{d}$ anti-quarks annihilate with u and d quarks, while $s\bar{s}$ annihilation occurs less frequently until saturation of the s and $\bar{s}$ abundances.

As a quantitative description of the strangeness enhancement, the ratio of the strange quark pairs with respect to the non-strange quark pairs (so-called Wroblewski ratio [28]) can be used as well:

$$\lambda_s = \frac{2\langle s\bar{s}\rangle}{\langle u\bar{u}\rangle + \langle d\bar{d}\rangle}, \tag{2.28}$$

where the quantities in brackets refer to the number of newly formed quark-antiquark pairs and thus exclude all quarks that were present in the target and projectile. The value λ_s varies from ≈ 0.2 (or about 20% of the strange quark pairs with respect to the light quark pairs production) in pp and peripheral collisions to ≈ 0.45 in central heavy ion collisions. The ratio is mainly determined by the most abundant (due to its smaller mass) strange particle, the kaon, and its ratio K/π to the pion (Fig. 2.12) with the strangeness enhancement factor of about 2, which becomes stronger for multiple-strange baryons and anti-baryons reaching 6–10 for Ξ ($\bar{\Xi}$), and about 20 for Ω ($\bar{\Omega}$).

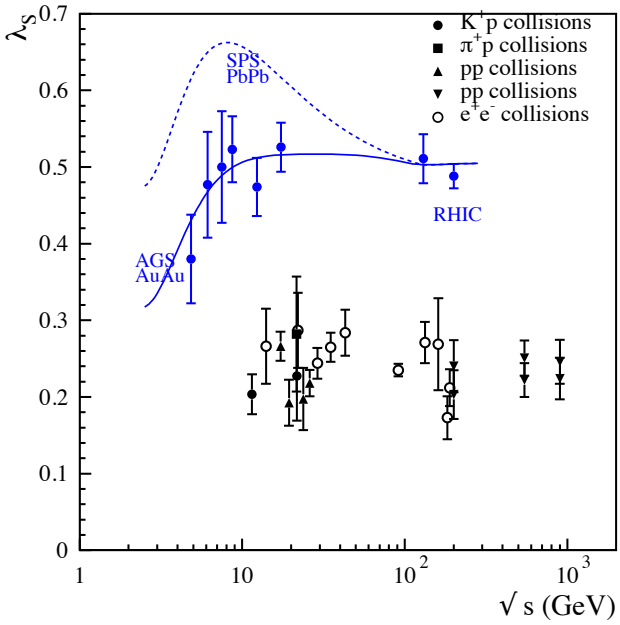

Figure 2.12: Wroblewski ratio in elementary and heavy ion collisions as estimated from statistical model fits. The superimposed dashed line is the predicted value from a fully equilibrated hadron gas, the solid line is the interpolation from hadron gas with extra strangeness suppression γ_s [27].

Thus, the abundance of strange quarks resulting in the strangeness enhancement is sensitive to the conditions and dynamics of the deconfined strongly interacting quantum chromodynamics matter phase.

Chapter 3

The Compressed Baryonic Matter (CBM) experiment

Investigation of the relativistic heavy ion physics [29] has began in 1970's at the BEVALAC facility at the Lawrence Berkeley Laboratory (LBNL) and later at SIS18 at GSI in Darmstadt. The hot and compressed matter was investigated in fixed-target experiments within the confined phase region. Investigation of the deconfined region became possible with ultra-relativistic heavy ion beams, where the kinetic energies of the particles far exceeded their rest masses, at the Brookhaven AGS and at the CERN SPS accellerators. Much higher collision energies have been reached in collider experiments STAR (Solenoidal Tracker at RHIC) at the Brookhaven Relativistic Heavy Ion Collider (RHIC) and ALICE (A Large Ion Collider Experiment) at the CERN Large Hadron Collider (LHC).

3.1 The Facility for Antiproton and Ion Research (FAIR)

The Facility for Antiproton and Ion Research (FAIR) project is aimed to build a large international center for studying the structure and fundamental properties of matter. It is an accelerating complex of new generation which will provide unique opportunities to perform research in the most exciting fields of modern science: nuclear, hadron and particle physics, atomic and anti-matter physics, high density plasma physics, and applications in condensed matter physics, biology and bio-medical sciences [30]. A layout of the FAIR accelerator complex is given in Fig. 3.1.

The four scientific pillars of the FAIR accelerator complex are:

- Compressed Baryonic Matter, CBM,

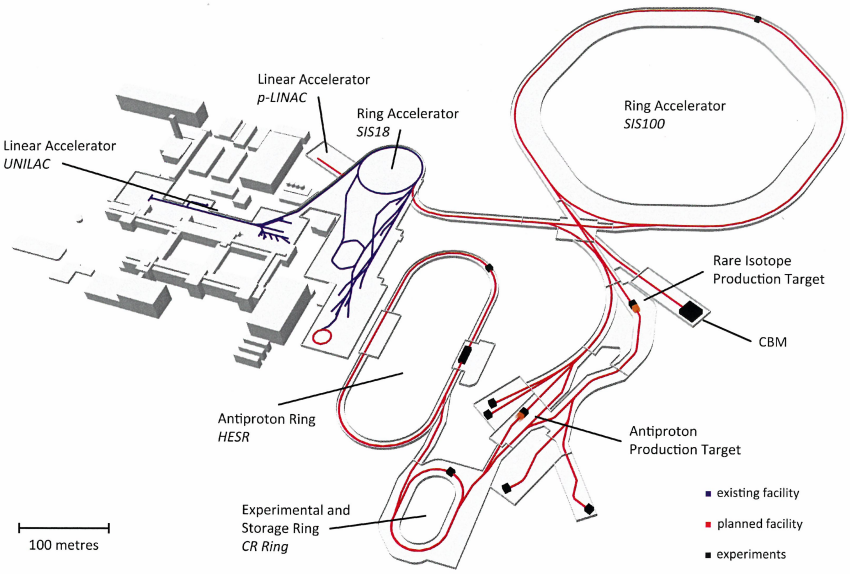

Figure 3.1: The Facility for Antiproton and Ion Research (FAIR) complex [30].

- antiProton ANnihilation at DArmstadt, PANDA,
- Nuclear Structure, Astrophysics and Reactions, NUSTAR,
- Atomic, Plasma Physics and Applications, APPA.

3.2 The CBM physics program

FAIR will provide heavy ion beam energies from 2–11 GeV/n with the SIS100 synchrotron, and 11–35 GeV/n with the SIS300 synchrotron. In central Au+Au collisions at FAIR SIS300 energies the nuclear fireball will be compressed to about 10 times saturation density ρ_0, even at SIS100 energies more than 8 times ρ_0 will be reached [29, 32, 33, A1]. At such densities, the nucleons will overlap each other and dissolve into their constituents.

The heavy ion beams of the FAIR facility are well suited to provide high net-baryon densities (Fig. 3.2, left), when the nucleons start to fuse and form large quark bags, and thus to explore the properties of strongly interacting matter at neutron star core densities [29, 34, A1]. According to different transport models and a hydrodynamics model, the nuclear fireball in central Au+Au collisions even at 5 GeV/n will be compressed to more than 5 times saturation density ρ_0, when the nucleons start to melt into quarks forming a mixed phase of hadrons and quarks. The calculations predict that the dense fireball spends a relatively long time within the phase coexistence region. These conditions appear to be sufficient

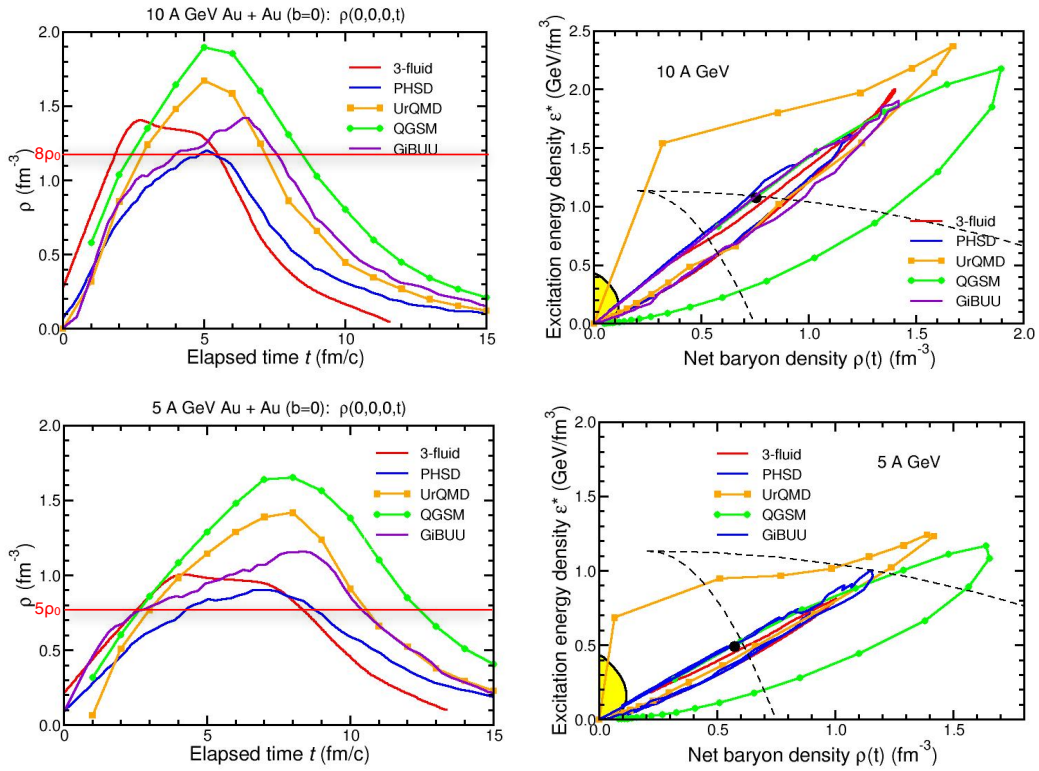

Figure 3.2: Evolution of the net-baryon density $\rho(t)$ as a function of elapsed time (left) and time evolution of the excitation energy density $\varepsilon^* = \varepsilon - m_N\rho$ versus the net-baryon density ρ (right, with a system evolving clockwise along trajectory) in the center of the fireball for central Au+Au collisions at beam energies of 5 GeV/n (bottom row) and 10 GeV/n (upper row) calculated by various transport models and a hydrodynamic model [29, 34]. The full symbols on the curves for UrQMD and QGSM indicate time steps of 1 fm/c. The dashed lines enclose the regions of phase coexistence [35]. The yellow zone denotes post-freeze-out streaming.

for the phase transition. At top SIS100 energies a net-baryon density of $8\rho_0$ will be reached to form pure quark matter.

In Fig. 3.2 (right) the excitation energy density $\varepsilon^*(t) = \varepsilon(t) - m_N\rho(t)$ (with the energy density $\varepsilon(t)$ and the mass density $m_N\rho(t)$) in the center of the collision zone is shown as a function of the net-baryon density for central Au+Au collisions at beam energies of 5 GeV/n and 10 GeV/n. The solid lines correspond to the time evolution (clockwise in the figure) of the system and the dots on the curves correspond to steps of 1 fm/c collision time in the UrQMD and QGSM models [29, 34]. The dashed lines enclose the expected region of phase coexistence [35]. The calculations predict that the dense fireball spends a sufficiently long time within the phase coexistence region already at 5 GeV/n and goes beyond this region at higher beam energies.

Working at relatively low beam energies of FAIR one may include into consideration also a chaotic motion of nucleons in nuclei, so-called the *Fermi motion*, which is described by the Fermi-gas model [7]. Because of the Pauli exclusion principle, each energy level in a potential well of a nucleus can be occupied by at most two nucleons of the same kind (protons or neutrons). The highest filled energy level is called the *Fermi level* and corresponds to the nucleon kinetic energy between 20 MeV for light nuclei and 40 MeV for heavy nuclei. The Fermi motion in nuclei has been experimentally verified in quasi-elastic electron scattering experiments. The Fermi momentum of nucleons is roughly constant for nuclei heavier than Ni and close to the corresponding value in infinite nuclear matter with density $\rho = 0.17$ fm^{-3}:

$$p_F = (3\pi^2\rho/2)^{1/3} = 270 \text{ MeV/c or } 1.37 \text{ fm}^{-1}. \tag{3.1}$$

The Fermi motion can widen substantially the true nucleon-nucleon center-of-mass energy distribution up to 20% depending on the colliding nuclei and their energies [7].

The experimental challenge of the CBM experiment [29, 32, 33, A1] is to identify diagnostic probes of the dense phase of the fireball which is transiently formed in the collision. The focus of CBM is, therefore, to study messengers from the dense fireball such as hadrons containing charm quarks, multiple strange hyperons, and dilepton pairs. The scientific program of the CBM experiment includes:

- The equation-of-state of nuclear matter at neutron star densities. CBM will measure the excitation functions of multi-strange hyperons in Au+Au collisions. At lower FAIR energies, Ξ and Ω hyperons are produced in sequential collisions involving kaons and Λs, and, therefore, are sensitive to the density in the fireball. CBM will measure also the excitation function of the collective flow of hadrons which is driven by the pressure created in the early fireball.

- Modifications of hadron properties in dense baryonic matter as a signature for chiral symmetry restoration. The relevant observable is the in-medium mass distribution of vector mesons decaying in lepton pairs in heavy ion collisions at energies from 2 to 45 GeV/n, and for different collision systems. Leptons are penetrating probes carrying the information out of the dense fireball.

- Phase transitions from hadronic matter to quarkyonic or partonic matter at high net-baryon densities, and the critical point of QCD matter. CBM will measure the excitation function of yields, spectra, and collective flow of strange and charmed particles in heavy ion collisions up to 45 GeV/n. CBM will measure event-by-event fluctuations of baryons and strangeness

in heavy ion collisions with high precision as function of beam energy from 2 to 45 GeV/n.

- Hypernuclei, strange dibaryons and massive strange objects. Theoretical models predict that single and double hypernuclei, strange dibaryons and heavy multi-strange short-lived objects are produced via coalescence in heavy ion collisions with the maximum yield in the region of SIS100 energies. CBM will measure the decay chains of single and double hypernuclei in heavy ion collisions at SIS100 energies. Few events have been observed in reactions with K^- beams. CBM will search for strange matter in the form of strange dibaryons and heavy multi-strange short-lived objects.

- Charm production mechanisms, charm propagation, and in-medium properties of charmed particles in (dense) nuclear matter. CBM will measure open charm and charmonium in proton-nucleus and nucleus-nucleus collisions at beam energies of 15–45 GeV/n.

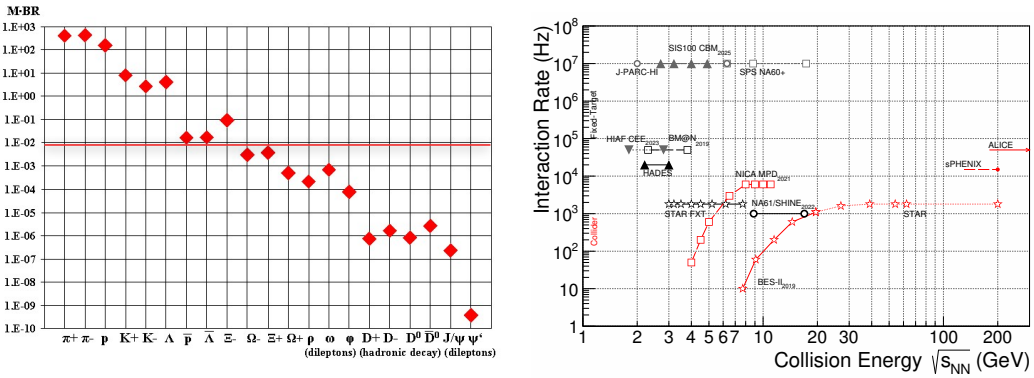

Figure 3.3: Left: Model predictions for central Au+Au collisions at 25 GeV/n for yields (multiplicity $M \times BR$ branching ratio) of observables intended to be measured in the CBM experiment [29]. The area below the red line indicates the particles that have not yet been accurately measured in heavy ion experiments in the FAIR energy range. Right: Running and future heavy ion experiments at moderate collision energies ordered with respect to the maximum interaction rate and the center-of-mass collision energy [31, A1].

The experimental program of CBM comprises the measurement of a large number of observables at different beam energies and different collision systems [29]. Many of them are extremely rare, like multi-strange anti-hyperons, open and hidden charm (Fig. 3.3, left). The area below the red line indicates the particles that have not yet been measured in heavy ion collisions at the FAIR energies. Most of these observables are very important, since they are produced during the first stages of the collision and can be used as probes of the compressed baryonic

matter at all stages of the collision. Charm and open charm are in particular the most challenging to measure.

In order to measure such rare observables with unprecedented precision, the CBM detector has to operate at very high interaction rates of up to 10^7 collisions per second, that is several orders of magnitude higher than the capacity of running and future heavy ion experiments (Fig. 3.3, right) and poses extreme requirements for detectors, read-out electronics and data processing.

3.3 The CBM detector setup

In the Compressed Baryonic Matter (CBM) experiment [32] with heavy ions highest baryon densities will be created and the properties of super-dense nuclear matter will be explored in various extreme states similar, for instance, to the conditions of matter in the center of neutron stars, where the matter is at the final stage of the evolution before transition into a black hole. The CBM experiment will complement the experimental heavy ion program at the LHC accelerator complex at CERN where the properties of the hot matter similar to that after the Big Bang are investigated. The layout of the CBM detector setup is shown in Fig. 3.4.

The goal of the experiment is to measure multiplicities, phase-space distributions and flow of protons, pions, kaons, hyperons, hadronic resonances, light vector mesons, charmonium and open charm including their correlations and event-by-event fluctuations in heavy ion collisions [29]. The CBM experiment has to identify both, hadrons and leptons, and to select rare probes at interaction rates of up to 10 MHz with particle multiplicities of up to 1000 charged particle per event.

The CBM setup consists of:

- a large acceptance dipole magnet to bend charged particles created in the collision;
- radiation-hard silicon pixel and strip detectors (a Micro Vertex Detector (MVD) and a Silicon Tracking System (STS)) are placed inside the superconducting dipole magnet and allow high-resolution tracking and momentum reconstruction for charged particles, and vertex determination. The MVD detector consists of four layers of silicon monolithic active pixel sensors, the STS detector is based on double-sided silicon micro-strip sensors arranged in eight stations;
- a Ring Imaging Cherenkov (RICH) detector comprising a CO_2 radiator and a UV photon detector realized with multi-anode photomultipliers for

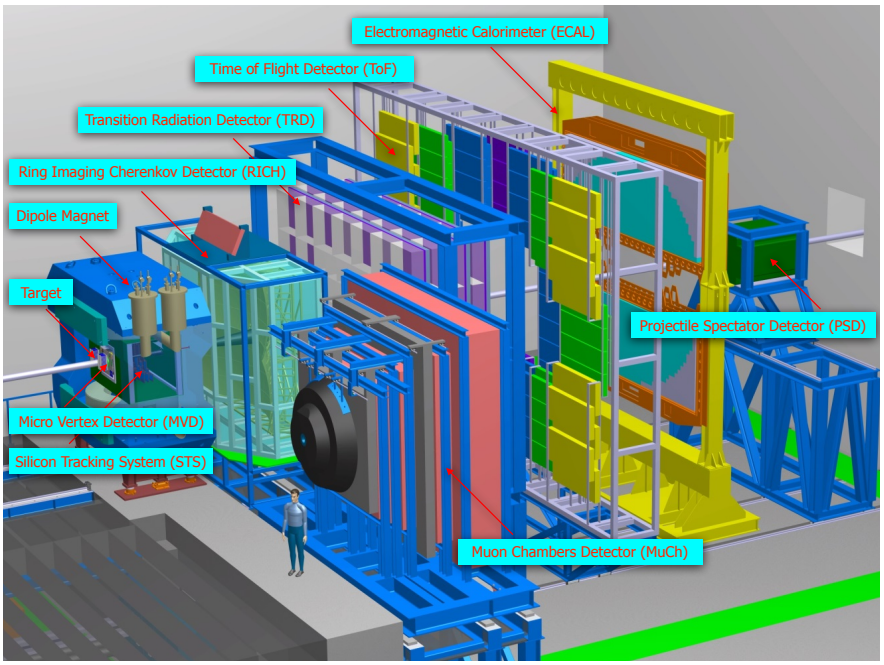

Figure 3.4: The CBM setup: target, superconducting dipole magnet, Micro-Vertex Detector (MVD), Silicon Tracking System (STS), Ring Imaging CHerenkov (RICH) detector, Transition Radiation Detector (TRD), Time-Of-Flight detector (TOF), Electromagnetic CALorimeter (ECAL), Muon Chambers (MuCh), and Projectile Spectator Detector (PSD).

electron identification and a Transition Radiation Detector (TRD) for pion suppression, particle tracking, and identification using specific energy loss are placed further downstream the magnet;

- Multi-Gap Resistive Plate Chambers (MRPC) with low-resistivity glass of a Time-Of-Flight detector (TOF) for the identification of hadrons;
- an Electromagnetic Calorimeter (ECAL) to measure direct photons in selected regions of the phase space;
- Muon Chambers (MuCh) will replace the RICH in the muon configuration and consist of a set of gaseous micro-pattern chambers sandwiched between hadron absorber plates made of graphite and iron;
- a Projectile Spectator Detector (PSD) for an event plane characterization and determination of the collision centrality.

In order to investigate the electron and muon components of di-leptons, the CBM detector will operate in two different configurations: in the electron setup the RICH will be used to measure di-electrons; in the muon setup muon pairs will

be measured using the MuCh detector. Both setups will be interchanged on a yearly basis.

The CBM detector is designed for studies on the SIS100, as well as the SIS300 accelerators, which is planned to be build a few years after the SIS100. The CBM setup for the SIS300 will have several more TRD stations, a larger TOF wall and the ECAL of a larger size with respect to the SIS100 version of the CBM setup.

Observables	MVD	STS	RICH	MuCh	TRD	TOF	ECAL	PSD
π, K, p		x	(x)		(x)	x		x
Hyperons		x			(x)	(x)		x
Open charm	x	x	(x)		(x)	(x)		x
Electrons	x	x	x		x	x		x
Muons		x		x		(x)		x
Photons							x	x
Photons ($e^{\pm}$ conv.)	x	x	x		x	x		x

Table 3.1: Observables and required detectors. Detectors marked as (x) can be used to suppress background [29].

The CBM detector components required for the measurement of the different observables are listed in Table 3.1.

Detection of a particle is based on interaction of the particle with matter, that causes an energy loss of the particle, and this energy is a subject to detect.

3.3.1 The Superconducting Dipole Magnet

The superconducting dipole magnet [38, 39] is a central part of the CBM detector system. The magnet has a large gap with a height of 140 cm and a width of 250 cm in order to install and maintain the target, and the tracking system of the Micro-Vertex Detector (MVD) and the Silicon Tracking System (STS) inside the magnet. Therefore the angular acceptance of the magnet should cover $\pm 25^o$ in the vertical and $\pm 30^o$ in the horizontal direction. The magnet is designed to generate the non-homogeneous vertical magnetic field with the field integral of 1 T·m to bend charged particle trajectories in the MVD and the STS detectors for momentum determination with a resolution $\Delta p/p = 1\%$.

The conceptual design of the magnet is shown in Fig. 3.5. The magnet is supplied with a yoke of magnetically soft steel with low carbon content. The upper and bottom beams form the poles of the magnet. The magnet is located in immediate proximity to the RICH detector, where the magnetic field should not exceed 250 G, therefore magnetic shields, reducing the field in the RICH, are installed on the yoke. The H-type magnet will be superconducting in order to reduce the operation costs. The superconducting coils have the "Cossack saddle"

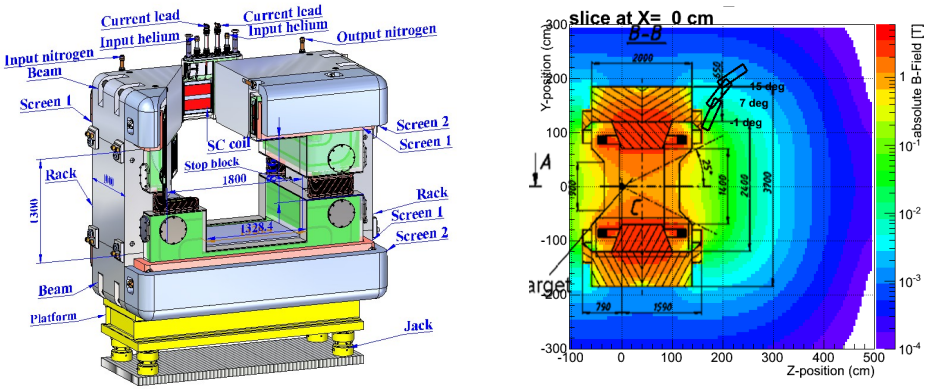

Figure 3.5: Left: 3D view of the dipole magnet with the support structure [38]. Right: Magnetic field distribution in the (y-z) plane at $x = 0$ [39].

form, which allows to create a magnet with a minimal size along the beam. The excitation coils are hosted in the cryostat.

3.3.2 The Micro-Vertex Detector (MVD)

The main task of the Micro-Vertex Detector (MVD) is the identification of D mesons via their weak hadronic decay into pions and kaons [29, 40, 41, 42, 43]. In addition, the MVD detector will provide background suppression for di-electron measurements, where close pairs have to be rejected in order to reduce the combinatorial background, as well as improved tracking for the hyperon identification.

Since the D meson lifetimes are $\tau = 123$ μm/c for D^0 and $\tau = 314$ μm/c for $D^{\pm}$, the MVD detector has to provide an extremely high position resolution of the secondary (decay) vertices reconstruction. That leads to the requirement to the MVD detector to have an excellent position resolution and a very low material budget to reduce effects of multiple scattering. For that reason the detector will be build on Monolithic Active Pixel Sensors (MAPS).

A cross section of a typical MAPS device is presented in Fig. 3.6 [41]. A MAPS sensor is composed of three differently P-doped silicon layers. A moderately doped epitaxial layer, which forms the sensitive volume of the device, lies in between two highly doped layers: the substrate and the P-wells. During the fabrication of a MAPS sensor, the substrate serves as the seed crystal for the growth of the epitaxial layer. It also contributes to the mechanical stability of the device. The doping levels of the substrate and the P-wells are several orders of magnitude higher than of the epitaxial layer.

The epitaxial layer forms the undepleted sensitive volume of the device. A minimum ionising particle penetrating this layer generates approximately 80 electron-hole pairs per micrometer of particle trajectory in the volume. The electrons

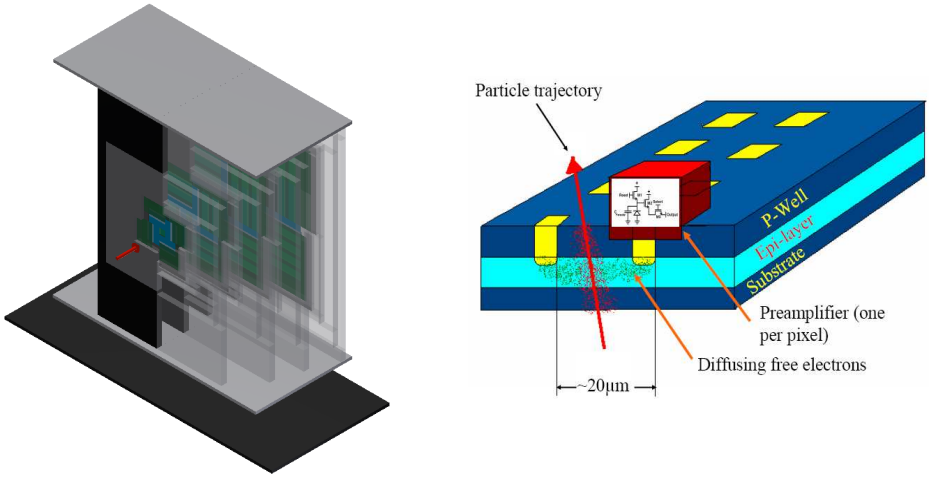

Figure 3.6: Left: The design proposal of the MVD detector. To visualize all stations and their sensors, the half-station support structures and the heat sinks of the "right downstream side"-group of the half-stations have been set transparent [42]. Right: Schematic view of a cross section of a MAPS device. The epitaxial layer is shown in light blue and the collecting diodes are indicated by the yellow areas. The red box is a representation of one pixel and does not correspond to a real implementation [41].

diffuse in the epitaxial layer but cannot leave it due to the repulsive field generated by the P^+/P^- junctions. They are collected by regularly implanted N-wells which form together with the epitaxial layer the charge collection diodes. Due to the charge collection by thermal diffusion, this charge is distributed over a cluster of roughly 3×3 pixels.

MAPS are developed in a standard CMOS[1] technology. The technology was first applied in photography as CMOS Image Sensors. As detectors in experimental particle physics MAPS were first proposed in 1999 and now, due to their high spatial resolution, they are used to build MAPS-based vertex detectors in several experiments.

The MVD detector is designed to have the pixel size between 25×25 μm^2 and 40×40 μm^2 with the hit position resolution from 3.5 μm to 6 μm depending on the pixel size. A total thickness will vary between 300 μm and 500 μm silicon equivalent for sensors and support structures. In addition to that, MVD will be positioned in vacuum to prevent multiple scattering before particles reach the first MVD station.

The detector will consist of four stations at the distances of 5, 10, 15 and 20 cm from the target. The first MVD station is placed at the closest possible position to the target to provide the most precise secondary vertex resolution. All these together will provide reconstruction of the secondary (decay) vertex of a D meson

[1]Complementary Metal-Oxide-Semiconductor

with a resolution of about (50–100) μm along the beam axis z.

3.3.3 The Silicon Tracking System (STS)

The Silicon Tracking System (STS) [44] is the main tracking detector of the CBM setup. Its task is to detect charge particles with high accuracy and efficiency to provide good quality and low noise measurements to track reconstruction algorithms at the expected multiplicity of charged particles to be up to 1000 per event within the STS acceptance, which covers polar angles from 2.5^o to 25^o.

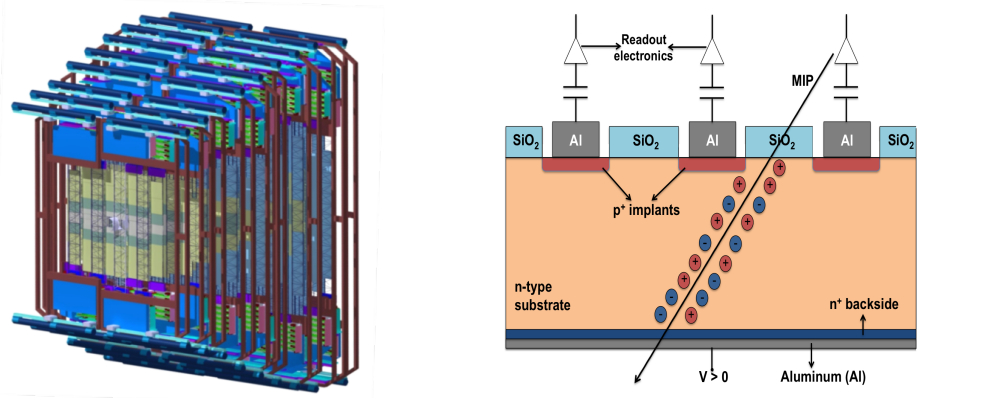

Figure 3.7: Left: The design proposal of the STS detector [44], which consists of 8 stations based on double-sided silicon micro-strip detectors on lightweight ladder-like mechanical supports. Several stations are horizontally enlarged for increased coverage of low-momentum particles in the dipole magnetic field. Right: Operational principle of silicon strip detector [45].

The STS detector (Fig. 3.7 (left)) consists of 8 layers of silicon detectors, which are located downstream of the target after the MVD detector at distances between 30 cm and 100 cm with the spacing between layers of 10 cm. It is placed within the magnetic field of about 1 T·m bending power. Since trajectories of charged particles are bended in the magnetic field, this should provide momentum determination of charged particles with a resolution of $(\Delta p/p) = 1\%$, that in turn requires thin detector modules with low multiple scattering of charged particles. Therefore to make possible an efficient track reconstruction, the STS system is based on silicon micro-strip detectors on lightweight ladder-like mechanical supports. The micro-strip sensors will be double-sided with a stereo angle of 15^o, a strip pitch of 60 μm, strip lengths between 20 and 60 mm, and a thickness of 300 μm of silicon, that will provide a typical hit resolution of the order of 25 μm. In order to reduce the amount of material in the detector volume, the data readout part will be done through multi-line micro-cables with fast electronics at the periphery of the stations, where the cooling lines will be placed as well.

The required time resolution of the STS is of the order of 10 ns, corresponding to a collision rate of 10 MHz.

The strips on the front side are tilted by 7.5^o and on the back side by -7.5^o creating a stereo angle of 15^o.

The operational principle of the silicon micro-strip detector is shown in Fig. 3.7 (right) [45]. A silicon detector is a revers-biased diode with the depleted zone acting as a solid-state ionization chamber. When a charged particle passes through a silicon detector, it produces many electron-hole pairs along the path. Average energy required to create a single electron-hole pair is about 3.6 eV for silicon. The charge released in the depletion region can be collected, whereas the charge created in the neutral, non-depleted zone recombines with the free carriers and is lost. Therefore, the silicon detectors should be operated with an applied voltage sufficient to fully deplete the crystal volume. Under the application of reverse-bias, the electrons drift towards the $n+$-side and holes to the $p+$-side. This charge migration induces a current pulse on the read-out electrodes and constitutes the basic electrical signal. The integrated current is equal to the total charge and hence is proportional to the energy loss of the particle in the sensitive region of the detector. A Minimum Ionizing Particle (MIP) traversing a silicon layer of depth 300 μm deposits the most probable energy of about 90 keV and produces about 85 electron-hole pairs per μm, i.e., 25000 electron-hole pairs for 300 μm thick silicon crystal.

3.3.4 The Ring Imaging CHerenkov (RICH) detector

The main task of the Ring Imaging CHerenkov (RICH) detector [46, 47, 48] is to provide identification and separation of electrons and pions from lowest momenta up to 8 GeV/c – 10 GeV/c and with a desirable pion suppression of at least 100 in order to ensure a high quality of the measurement of di-electrons as we aim at covering di-electron masses ranging from below ρ, ω to beyond charmonium, as well as at a reconstruction of photons using γ-conversion pairs. The RICH detector will consist of a 1.7 m long gaseous CO_2 radiator (overall length approximately 2 m) and two arrays of mirrors and photon detector planes (Fig. 3.8 (left)). The mirror plane is split horizontally into two arrays of spherical glass mirrors, 4 m $\times$ 1.5 m each. The 72 mirror tiles have a curvature of 3 m radius, a thickness of 6 mm and a reflective Al+MgF_2 coating. Rings of Cherenkov radiation will be projected onto two photon detector planes 2 m $\times$ 0.6 m each located behind the CBM dipole magnet and shielded by the magnet yokes. As photon detector, multi-anode photomultiplier tubes (MAPMT) are foreseen. They provide sufficient granularity and fast response to allow running at the maximum CBM interaction rate of 10 MHz.

In-beam tests with a prototype RICH of real-size length showed that 22 photons

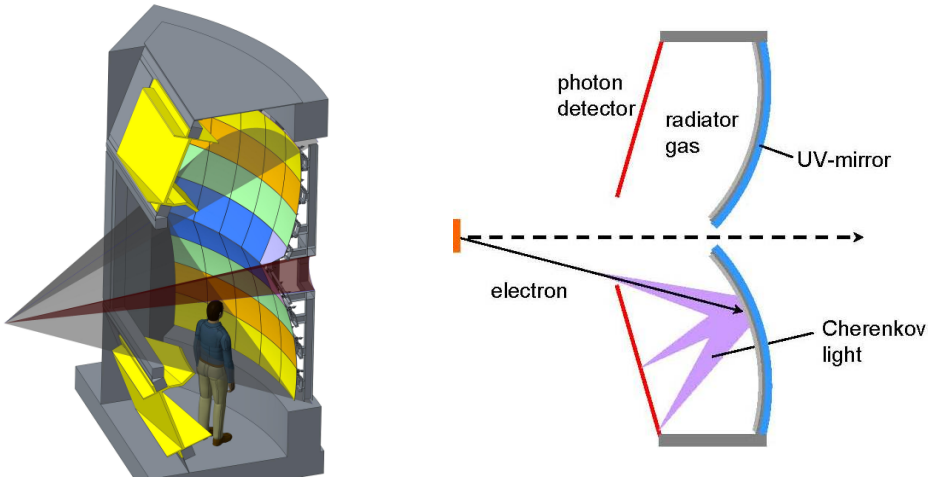

Figure 3.8: Left: The design proposal of the RICH detector [49], shown in the beam direction. The sensor planes are shown in yellow, the mirror tiles in several colours, and the complete support structure in grey. The transparent grey cone marks the geometrical acceptance. Right: Schematic view of the RICH detector with its imaging UV mirrors. The Cherenkov cones are imaged on the photomultiplier tubes (PMT) as rings [46].

are measured per electron ring. On the order of 100 rings are seen in central Au+Au collisions at 25 GeV/n beam energy due to the large material budget in front of the RICH detector. Still, due to the high granularity (approx. 55 000 channels) and high number of photons per ring, a pion suppression on the order of 500 is expected to be achieved according to simulations.

The RICH detector will be placed next to the dipole magnet about 1.6 m downstream of the target. Its mechanical structure is designed such that the whole RICH detector can be exchange with the MuCh detector for a complementary measurement of di-leptons in the di-muon channel.

The RICH detector operation is based on the Cherenkov radiation. This previously unknown radiation in medium under the influence of fast electrons was first observed in 1934 by Pavel Cherenkov, a PhD student of the Lebedev Institute of Physics (FIAN, Moscow), who worked under the supervision of Sergey Vavilov. The nature of this luminescence was explained in 1937 by Igor Tamm and Ilya Frank, who showed that with uniform and rectilinear motion of a charge particle in a homogeneous and infinite medium with a velocity exceeding the phase velocity of light propagation in a given medium, radiation must emerge whose properties coincide with those observed by Cherenkov. Mechanical and acoustic (shock Mach waves) analogs of this radiation are also well known. In 1958, Cherenkov[2], Tamm and Frank jointly received the Nobel Prize in Physics

[2]Sergey Vavilov died in 1951, and the Nobel Prizes are not awarded posthumously.

for the discovery and the study of the Cherenkov effect.

The Cherenkov effect is that an electric charge particle moving in a medium with a constant velocity v emits electromagnetic waves (light) with a continuous spectrum and with a specific angular distribution. In this case, radiation at the frequency ω occurs only if the velocity of the charge particle v exceeds the phase velocity of light in the transparent medium $v = c/n(\omega)$, i.e.

$$v > \frac{c}{n(\omega)}, \tag{3.2}$$

where $n(\omega)$ is the refractive index of light (at frequency ω) in the medium (c is the speed of light in vacuum). The peculiarity of the angular distribution of radiation mentioned above is that the wave vector of radiated waves $\vec{k}$ forms an angle θ with velocity $\vec{v}$, and:

$$\cos(\theta_0) = \frac{c}{n(\omega)v}. \tag{3.3}$$

These results can be obtained using the Huygens principle: each point in the path of a charged particle moving uniformly and rectilinearly with speed v becomes the source of a spherical wave emitted at the moment when the charged particle passes through the point. Under condition (3.2), these spheres have a common envelope — a cone with a vertex that coincides with the instantaneous position of the charge particle, and the angle θ_0 is determined by the expression (3.3). The angle θ_0 is the same for all frequencies ω and the radiation has a sharp front, which forms a cone with the angle of the solution $(\pi - 2\theta_0)$ and the charge particle at its vertex. This cone is analogous to the Mach cone, which characterizes the shock wave produced by the supersonic motion of a source in air or other medium, when the hydrodynamic or acoustic front on the Mach cone is sharp and is often observed, for example, during the flight of a supersonic aircraft.

Thus, the Cherenkov radiation is an electromagnetic radiation in a form of radiation cone emitted by a charged particle which passes through a dielectric medium with a speed greater than the phase velocity of light in that medium. In that case the particle disrupts the local electric field in the medium making it electrically polarized by the particle's electric field. The excited atoms or molecules of the medium will produce γ radiation relaxing back to an equilibrium state. Since the particle travels with a greater speed than light in the medium, the result is a cone of Cherenkov photons, which travels at the speed of light in the medium c/n, where c is the speed of light in vacuum, n is the refraction index of the medium. The Cherenkov photons are mainly emitted in the visible and ultraviolet (UV) region of the spectrum. The Cherenkov light cone is further reflected in the RICH detector (Fig. 3.8 (right)) by the focusing mirrors to the PMT planes to form a ring.

3.3.5 The Transition Radiation Detector (TRD)

It is interesting that the transition radiation was discovered as a result of the study of the Cherenkov radiation. Igor Tamm and Ilya Frank theoretically determined the properties of the Cherenkov radiation for an infinite medium, but in actual experiments the dimensions of the Cherenkov emitter are always limited. Therefore, Vitaly Ginzburg and Ilya Frank began to study this process and in 1944 predicted the existence of a new type of electromagnetic radiation, which they called transition radiation. Transition radiation arises when the boundaries of two media intersected by a moving charge, in which the propagation velocities of electromagnetic waves are different. In particular, they considered the case of the motion of an electron from a vacuum into an ideal conductor.

Let us consider a charge that moves in a vacuum in the direction of a high-conducting metal, playing the role of an ideal mirror. It is known from electrodynamics that under such conditions the charge field in vacuum is the sum of the charge fields q moving in vacuum in the absence of a mirror and the charge $-q$ moving in the mirror towards the charge q (i.e. with the speed $-v$). The charge $-q$ is thus the "image" of the charge q. When the charge q crosses the boundary, it enters a highly conductive medium and practically no more field is created in the vacuum; the $-q$-image also disappears. Thus, in a vacuum, annihilation of a pair of charges q and $-q$ occurs, and in annihilation, as in any acceleration of charges (in this case, both "charges" q and $-q$ abruptly stop at the interface), radiation arises — the transitional radiation. Such radiation "back" into vacuum has not found much practical application.

Much more important in practical terms for ultra-relativistic particles was the radiation "forward", i.e. in the direction of the velocity of the particle as it leaves the medium into the vacuum. In this case radiation of very high frequencies will also be emitted, and the total radiation energy of a particle with charge q and mass m is:

$$W = \frac{q^2 \omega_p}{3c} \frac{E}{mc^2}, \tag{3.4}$$

where ω_p is the plasma frequency of the medium. At high frequencies, all substances are equivalent to a plasma with dielectric constant

$$\varepsilon = n^2 = 1 - \frac{{\omega^2}_p}{\omega^2}; \quad {\omega^2}_p = \frac{4\pi e^2 N}{m_e}, \tag{3.5}$$

N is the electron concentration in the medium, e and m are the charge and mass of the electron.

The radiation energy W is proportional to the energy of the particle E, and therefore, measuring W, it is possible to determine the energy E, which is very important in the experimental high energy physics. The transition radiation detectors are based on the measurement of the energy W of the "forward" transition

radiation. It should be noted that since the energy W for one boundary is very small, transition detectors need to use many layers of materials with different indices of refraction, separated, for example, by air interlayers.

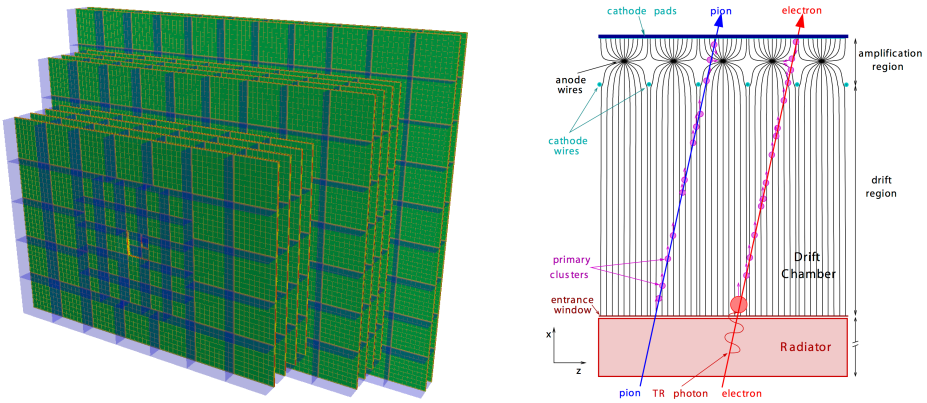

Figure 3.9: Left: A schematic setup of the complete TRD with three stations of four, four and two detector layers. The inner-most detector modules in station one and two are smaller than the outside ones [50]. Right: Schematic layout of a Multi-Wire Proportional Chamber (MWPC) with a transition radiation photon [50].

In the CBM experiment the Transition Radiation Detector (TRD) [29] will be built of three stations (Fig. 3.9 (left)) each consisting of 3–4 detector layers and located at approximately 5 m, 7.2 m and 9.5 m downstream the target. The detector is divided into rectangular pads with a resolution of 300–500 μm across and 3–30 mm along the pad. Every second transition radiation (TR) layer is rotated by 90^o to ensure an accurate measurements in both coordinates.

The TRD detector is aimed for the reconstruction of particle trajectories, for the identification of electrons and positrons with $p > 1.5$ GeV/c, and for the pion suppression of 100 at 90% electron efficiency. Only such ultra relativistic ($\gamma > 1000$) electrons and positrons are able to produce TR-photons at these momenta. The production of transition radiation (Fig. 3.9 (right)) takes place when an ultra-relativistic particle crosses multiple layers of different materials with different electromagnetic properties of the media. A typical energy of a TR-photon is within the range of 1–30 keV.

3.3.6 The Time-Of-Flight detector (TOF)

The Time-of-Flight detector (TOF) [29, 51] of the CBM experiment will provide identification of charged hadrons by measuring the time of flight and determining the particle momentum (in addition to the STS detector). It will be a wall composed of Multi-gap Resistive Plate Chambers (MRPC) (Fig. 3.10 (left)) and covering the polar angles between 2.5^o to 35^o in X and 2.5^o to 25^o in Y. This

corresponds to an active area of about 120 m^2 (about 13.5 m width and 9 m height) at a 10 m distance from the target. At small deflection angles the pad size is about 5 cm^2 corresponding to an occupancy of below 5% for central Au+Au collisions at 25 GeV/n. The required time resolution is on the order of 80 ps.

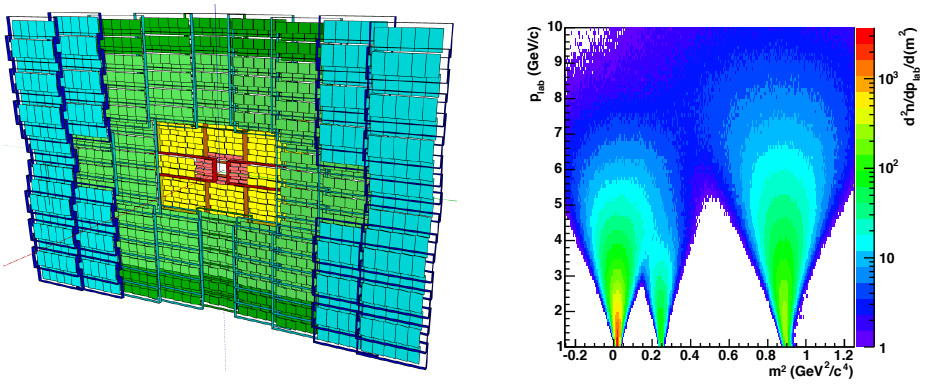

Figure 3.10: Left: A schematic setup of the complete TOF wall [51]. Right: Distribution of m^2 versus momentum for positively charged hadrons. The distance between target and TOF detector is 10 m, the time resolution is 80 ps [51].

Let us consider the time of flight method, which is used to determine the mass of a particle in the TOF detector [52, 53]. The particle momentum p is related to its rest mass m_0 by the expression:

$$p = \frac{m_0 v}{\sqrt{1 - \frac{v^2}{c^2}}} = \frac{m_0 \beta c}{\sqrt{1 - \beta^2}} = m_0 \beta \gamma c, \tag{3.6}$$

where $\beta = v/c$ is the velocity of the particle in units of the speed of light c, and γ is the Lorentz contraction factor $\gamma = 1/\sqrt{1 - \beta^2}$. For a particle flying a distance L in a time t:

$$\beta = \frac{v}{c} = \frac{L}{tc}, \tag{3.7}$$

then the equation that relates the mass of the particle to the time of flight is:

$$m_0 = \frac{p}{\beta\gamma c} = \frac{p\sqrt{1 - \beta^2}}{\beta c} = \frac{p}{c}\sqrt{\frac{1}{\beta^2} - 1} = \frac{p}{c}\sqrt{\frac{t^2 c^2}{L^2} - 1}. \tag{3.8}$$

In accordance with this equation, it is possible to calculate the mass of the particle from the measured momentum and time of flight giving the distance L to the detector wall (or, more precisely, the trajectory length) is known.

It is clear that the accuracy of separation of different particles with the same momentum will be determined by the accuracy of measuring the times of their flight from the target to the detector wall. This imposes high demands on the

accuracy of measuring the time of flight in the TOF detector. By reordering (3.8) this condition can be expressed in the following equation for equal path lengths of two particles with equal momenta:

$$\Delta t = t_2 - t_1 = \frac{L}{c}\left|\sqrt{1+\frac{m_2^2c^2}{p^2}} - \sqrt{1+\frac{m_1^2c^2}{p^2}}\right| \approx \frac{Lc}{2p^2}(m_2^2 - m_1^2), \tag{3.9}$$

where $\sqrt{1+(mc/p)^2} \approx 1 + (mc)^2/2p^2$ for relativistic particles with $p \gg mc$.

The separation power, i.e. the TOF difference in units of the TOF time resolution σ_{TOF}, can then be expressed as:

$$n_{\sigma_{TOF}} = \frac{|\Delta t|}{\sigma_{TOF}} \simeq \frac{Lc}{2p^2\sigma_{TOF}}\left|m_2^2 - m_1^2\right|. \tag{3.10}$$

Usually a separation power of $n_{\sigma_{TOF}} \geq 3$ is required to assign the proper identification to individual particles.

The main task of the TOF detector is the separation of protons, kaons and pions (Fig. 3.10 (right)). At a fixed time resolution, there is always a momentum limit above which there is a misidentification between the types of particles with adjacent masses (π/K, K/p). To increase this limit, one can according to (3.10) either improve the time resolution, or increase the path length over which the time of flight is measured. The nominal position of the CBM TOF wall will be at 10 m from the target for the typical SIS300 beam kinetic energy of 25 GeV/n for Au+Au collisions. However, in the first FAIR phase on SIS100 with beam energies up to 11 GeV/n for Au+Au collisions the nominal position will be at 6 m from the target to detect more kaons before they decay (the decay length of kaons is $c\tau = 3.712$ m). The main requirement for the CBM TOF wall performance is to allow for a 3σ separation of pions and kaons up to 4 GeV/c momentum at the nominal position of 10 m from target.

In order to achieve the optimal performance, the detector is also divided into several different regions in accordance with the expected particle fluxes (Fig. 3.10 (left)). Therefore, the fluxes in different regions of the detector depend not only on the interaction rate and the multiplicity of particles, but also on a position of the wall itself. The development of timing RPCs is therefore focused on high rate capability, low resistivity material, long term stability and the realization of large arrays with overall excellent timing performance.

3.3.7 The Electromagnetic Calorimeter (ECAL)

Calorimetric methods [54] imply total absorption of the particle energy in a bulk of material followed by the measurement of the deposited energy. High energy

photons, electrons and hadrons can interact with the medium to produce secondary particles, resulting in the development of a shower and much more efficient particle energy absorption in the material [5]. Thus, calorimeters are widely used in high energy physics to detect the electromagnetic and hadronic showers. Accordingly, such detector systems are referred to as electromagnetic and hadron calorimeters.

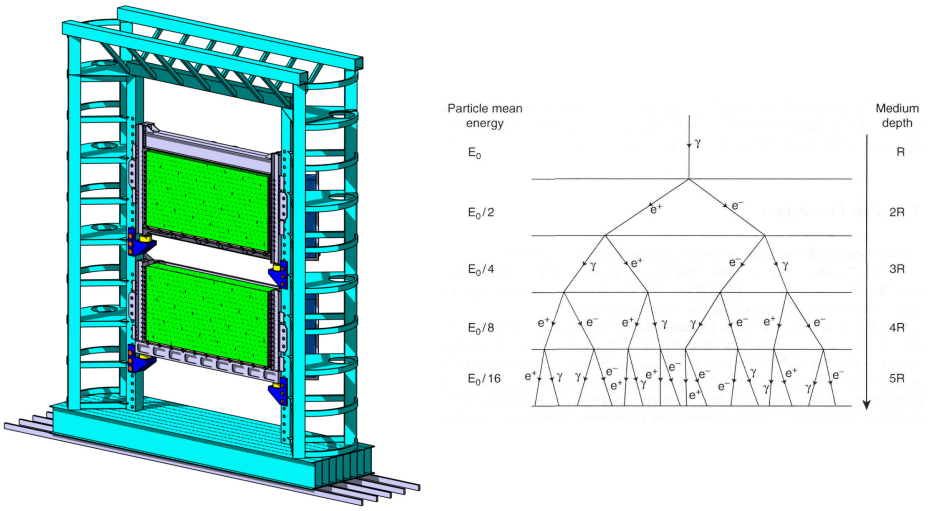

Figure 3.11: Left: The ECAL calorimeter system optimized for SIS100 [55]. Right: Simplified scheme of an electromagnetic cascade development initiated from a photon [5].

The main goal of the Electromagnetic Calorimeter (ECAL) [29, 55] (Fig. 3.11 (left)) in the CBM experiment is to identify electrons and photons and to provide measurements of their energy and position. ECAL will measure spectra of photons and neutral mesons decaying in their photonic decay channels. Measurement of the spectrum, for example, of π^0 is important to study dependence of the particle yield on the thermodynamic parameters of nuclear matter. Elliptic and directed flows of π^0, measured by ECAL, will be used to study the collision geometry and collective phenomena. Used together with RICH and TRD, ECAL will significantly contribute to the identification of particles because of its high capability to discriminate photons, electrons and hadrons with high efficiency and purity and will considerably improve the identification of J/ψ.

A high energy photon in matter turns into an electron-positron pair [5], where each e^- (e^+), in turn, is able to emit energetic photons through bremsstrahlung. These radiated photons can convert into pairs, which could again radiate, and so on. Thus, an electromagnetic shower (electromagnetic cascade) is produced with a large number of photons, electrons and positrons. The process continues until the electron and positron energies are below the critical energy E_c of

bremsstrahlung, i.e. when they lose energy only due to ionization and excitation of atoms of the medium.

The cascade development is a statistical process. Let us imagine (see Fig. 3.11 (right)) that the primary photon of energy E_0 converts into an e^+e^- pair after a radiation length L_{rad}, and the mean energy of the electron or positron is $E_0/2$. In the next radiation length, the electron and positron both emit one bremsstrahlung photon, which has approximately half the energy of the charge particle that emitted it. At this stage, after two L_{rad}, we have two photons and an e^+e^- pair. In the next radiation length (at three L_{rad}), each of the two photons is converted into an e^+e^- pair, and the previous e^+e^- pair emits two photons. Consequently, the number of particles is $8 = 2^3$, of which six are e^-, e^+, and two are γs with the mean energy of any of these particles equal to $E_0/8$. Continuing the cascade further, after t radiation lengths, the number of γ , e^- and e^+ particles is $N \simeq 2^t$, each of them with a mean energy $E_N \simeq E_0/2^t$. The same result would be obtained for a cascade initiated from an e^- instead of a γ. Here the medium thickness is measured in radiation lengths, $t = x/L_{rad}$.

Measuring the energy in units of critical energy E/E_c, one can calculate the maximum penetration t_{max} of the cascade:

$$E_{t_{max}} \simeq \frac{E_0}{2^{t_{max}}} = E_c, \qquad t_{max} \simeq \frac{\ln(E_0/E_c)}{\ln 2}. \tag{3.11}$$

For energies lower than E_c, the dominant mechanism of energy loss of the electrons is not bremsstrahlung, but the continuous processes of excitation-ionization which do not allow the radiation of new particles. The maximum number of particles present in the cascade at a given instant is therefore

$$N_{max} \simeq E_0/E_c. \tag{3.12}$$

Thus the number of particles in a cascade increases exponentially up to the maximum, after that it decreases gradually due to the statistical nature of the cascade process.

Typically, calorimeters are segmented transversely to provide information about the position of the particle and its deposited energy, and longitudinal segmentation to provide information for the particle identification based on the shape of the shower.

According to that, the ECAL detector of the CBM experiment uses the "shashlik" technology and is built from individual modules that are made from lead absorber plates interspaced with scintillator tiles as active material. Wavelength-shifted (WLS) fibers penetrate the lead/scintillator stack through the holes, and readout takes place on the back side of the sampling structure using photomultipliers. The optimized for SIS100 calorimeter system (Fig. 3.11 (left)) has 4352 electronic channels, built from 1088 modules with 60×60 mm^2 cells. The calorimeter

modules are grouped in two rectangular blocks which could be moved up and down in order to change the angular range of measured particles and to optimize the experimental conditions for different colliding ion systems and beam energies.

3.3.8 The Muon Chamber (MuCh) system

The key observables in the CBM physics program include measurement of low-mass vector mesons and charmonia, which are detected via their decays into dileptonic channels, a very sensitive diagnostic probe for extracting information about the collision process. Thus the experimental challenge for muon measurements in heavy ion collisions at FAIR energies [29, 56] is to identify low-momentum muons in an environment of high particle densities.

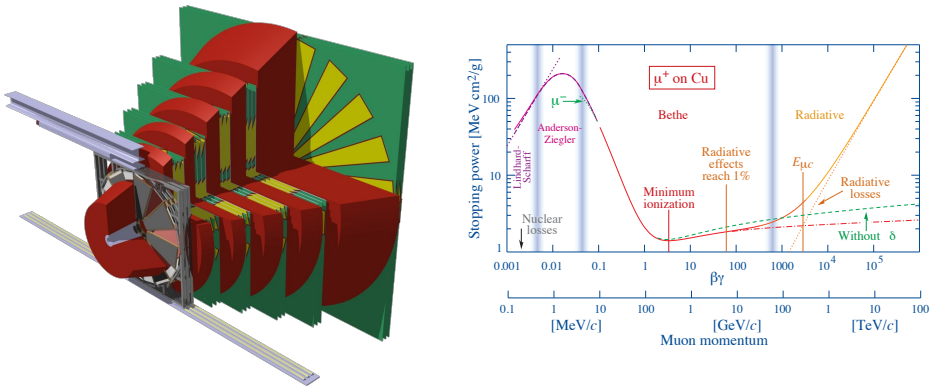

Figure 3.12: Left: The MuCh detector geometry consisting of segmented absorbers (red) and triplets of gaseous detectors (yellow) of charged particles together with the support structure (green) [56]. Right: The mean stopping power for muons in a material [57].

Muons are characterized by a much greater penetrating power than any other known particles except for neutrinos. The main reason is that they interact only electromagnetically with the shell electrons of atoms in the material, but being 200 times heavier than electrons, they lose only a small fraction of the energy in such collisions. In addition, because of their high mass, they hardly emit energy as they pass through matter, much less deviating in the electric field of atomic nuclei. A small loss of energy means that a muon can penetrate far into the material before it loses all its energy.

The mean stopping power (Fig. 3.12 (right)) for high energy muons in a material [58] can be described by:

$$\langle -dE/dx \rangle = a(E) + b(E) \cdot E, \tag{3.13}$$

where E is the total energy, $a(E)$ is the electronic (ionization and excitation)

stopping power, and $b(E)$ is the energy-scaled contribution from radiative processes — bremsstrahlung, pair production, and photonuclear interactions:

$$b \equiv b_{brems} + b_{pair} + b_{nucl}. \tag{3.14}$$

The notation is convenient because $a(E)$ and $b(E)$ are slowly varying functions of E at the high energies where radiative contributions are important. For most materials $b(E) \cdot E$ is less than 1% of $a(E)$ for $E \leq 100$ GeV.

The radiative contribution $b(E)$ is a slowly-varying function of energy which is asymptotically constant. To a very rough approximation the bremsstrahlung contribution scales as $1/M_\mu^2$, the pair-production and photonuclear interaction parts scale as $1/M_\mu$.

The muon critical energy is defined as the energy at which electronic losses and radiative losses are equal (3.13). It is obtained by finding $E_{\mu c}$ such that:

$$a(E_{\mu c}) = b(E_{\mu c}) \cdot E_{\mu c}, \qquad E_{\mu c} = \frac{a(E_{\mu c})}{b(E_{\mu c})}. \tag{3.15}$$

The CBM concept is to track the particles through a hadron absorber system, and to perform a momentum-dependent muon identification. This concept is realized (Fig. 3.12 (left)) by segmenting the hadron absorber in several layers, and placing triplets of tracking detector planes in the gaps between the absorber layers. The absorber-detector system is placed downstream of the Silicon Tracking System (STS) which determines the particle momentum. In order to reduce meson decays into muons the absorber-detector system has to be as compact as possible.

The actual design of the muon detector system consists of 6 hadron absorber layers of iron plates with increased thickness from 20 cm for the first absorber layer up to 100 cm for the last one, and 15–18 gaseous tracking chambers located in triplets behind each iron slab. The identification of a muon depends on its momentum which varies with the mass of the vector mesons and with beam energy. For example, for beam energies above 15 GeV/n muons from the decay of J/ψ mesons have to pass all 6 absorber layers with a total iron thickness of 225 cm corresponding to 13.4 interaction length λ_I. The muons from the decay of low-mass vector mesons (ρ, ω, ϕ) only have to penetrate through 5 iron absorber layers with a total thickness of 125 cm corresponding to 7.5 λ_I.

3.3.9 The Projectile Spectator Detector (PSD)

The Projectile Spectator Detector (PSD) [29, 59] will be used to determine the collision centrality and the orientation of the reaction plane. A very precise characterization of the event class is of crucial importance for the analysis of

event-by-event observables. The study of collective flow requires a well defined reaction plane which has to be determined by a method not involving particles participating in the collision.

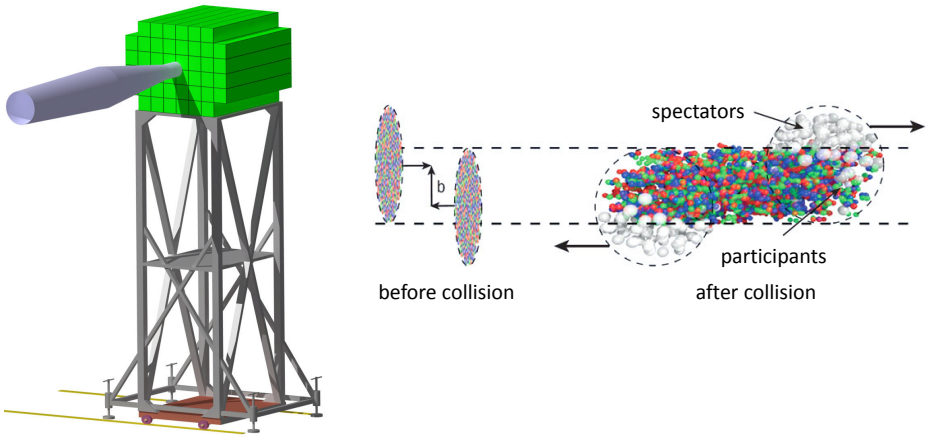

Figure 3.13: Left: The PSD detector geometry with modules (green) consisting of consecutive absorber and scintillator layers [59]. Right: Schematic representation of a nuclear collision with participants and spectators [60]. During a central collision all nucleons participate in the collision, while at peripheral collisions the number of spectators is considerable.

A collision of two heavy ions at relativistic or ultra-relativistic energies can be considered based on simple geometrical concepts with all nucleons travelling along parallel straight line trajectories. At such high beam energies the binding energy of the nucleons in their nuclei can be neglected and the heavy ion collision can be represented as a superposition of many nucleon-nucleon collisions (Fig. 3.13 (right)). The number of nucleons participating in the collision is inversely related to the value of the *impact parameter b*. In a *central collision* with a close to zero impact parameter, all nucleons are involved in the interaction process. A *peripheral collision* with a large impact parameter consists of a small number of participants N_{part} and a large number of spectators N_{spec}. A set of collisions averaged over different impact parameters are called *minimum-bias* events. It is expected that only central collisions will provide a sufficiently dense medium to produce a deconfined phase of nuclear matter.

If we extend the definition of the impact parameter b and consider a two-dimensional *impact vector* $\mathbf{b}$ connecting centers of the colliding nuclei in the plane transverse to the nucleon trajectories, then the *impact vector* $\mathbf{b}$ and the beam axis $\mathbf{z}$ determine the *reaction plane* of the collision.

The PSD detector is designed to measure the number of non-interacting nucleons (spectators) from a projectile nucleus in nucleus-nucleus collisions. The PSD (Fig. 3.13 (left)) is a full compensating modular lead-scintillator calorimeter which provides very good and uniform energy resolution. The calorimeter

comprises 12×9 individual modules, each consisting of 60 lead-scintillator layers with a surface of 10×10 cm^2. The scintillation light is read out via wavelength shifting (WLS) fibers by Multi-Avalanche Photo-Diodes (MAPD).

3.3.10 The Data AcQuisition (DAQ) system

The Data AcQuisition (DAQ) system automatically collects information from the detector front-end electronics, such as signals from registered particles and the status of the detector as such, as well as provides primary processing (for example, converting analog signals to digital ones), accumulating and transferring data to a computer cluster for further processing and analysis.

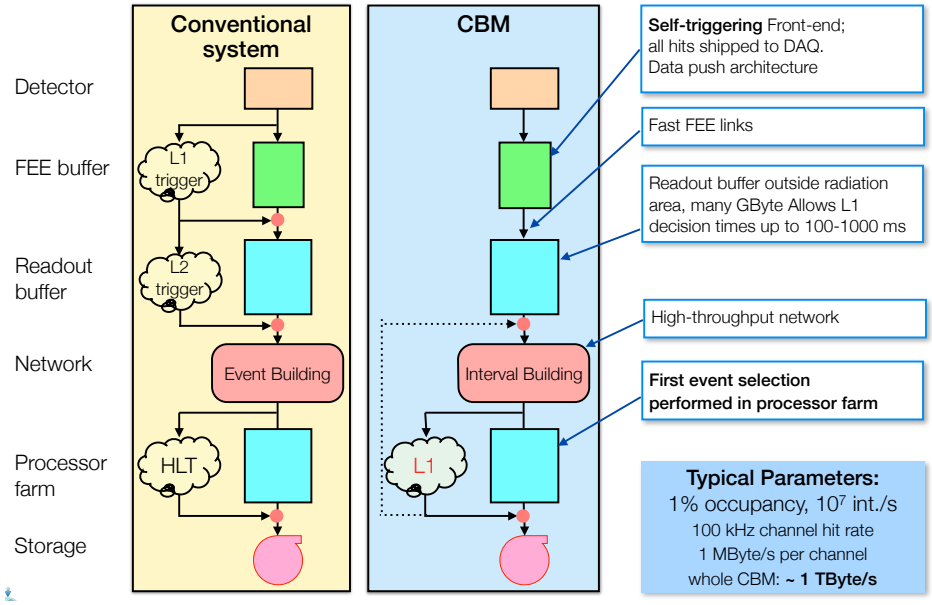

Figure 3.14: The CBM DAQ system will differ from the conventional DAQ approach with several stages of low level triggers (L1, L2) and the High Level Trigger (HLT), but is designed to have only one (L1) high level stage of the data selection [61] called the First Level Event Selection (FLES).

At the CBM design interaction rate of 10 MHz, one expects a raw data rate of up to 1 TB/s from the detector front-end electronics [62]. In order to optimise the cost of storage capacity CBM requires the maximum archival rate of 3 GB/s, thus reducing the raw data rate online by a factor of 300 or more. The experimental challenge is therefore to identify and select ($1/300 = 0.3\%$) of rare and complex decay topologies in real time for archival and to discard the vast majority (99.7%) of the raw data. For reasons of the high interaction rate and complex triggering signatures, a readout concept was chosen (Fig. 3.14), based on self-triggered, free-streaming front-end electronics that transmit time-stamped

data messages to the DAQ system when the readout channel is activated above a predetermined threshold. The DAQ system aggregates and pushes all data to an online computing (FLES) farm, where the event reconstruction and selection will be performed in software. The FLES farm will first combine the data streams from the detector front-ends into "time slices", which contain all raw data within a given time interval, and then the reconstruction procedures will be performed in order to take a decision of keeping or rejecting each event found in the time slice.

3.3.11 The First Level Event Selection (FLES)

The First Level Event Selection (FLES) package of the CBM experiment is intended to reconstruct online the full event topology including long-lived charged particles and short-lived charged and neutral particles.

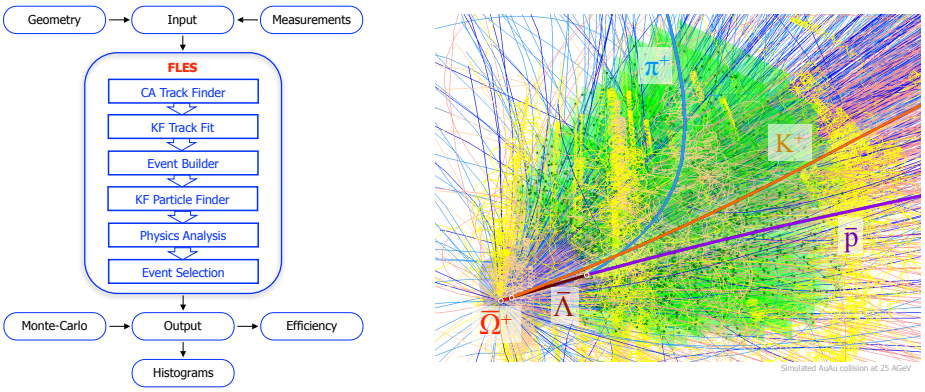

Figure 3.15: Left: Block diagram of the FLES package [63]. Right: A simulated central Au+Au collision at 25 GeV/n energy with about 1000 charged particles, where a trigger signature $\bar{\Omega}^+ \to \bar{\Lambda}K^+ \to \bar{p}\pi^+K^+$ is hidden and should be reconstructed by the FLES package in real time [64].

The FLES package consists of several modules (Fig. 3.15 (left)) [63]: a track finder, a track fitter, a particle finder and a module for physics selection. As an input the FLES package uses geometry of the tracking detectors and the detected positions (hits) of the registered charged particles. Trajectories (tracks) of the long-lived charged particles are reconstructed by the Cellular Automaton (CA) track finder based on the registered hits. The Kalman Filter (KF) based track fit is used for precise estimation of the track parameters and their errors in form of a covariance matrix. The short-lived particles, which mainly decay before they reach the first tracking detector stations, can be reconstructed via their long-lived decay products. The KF Particle Finder [65], which is based on the KF Particle package is used to find and reconstruct the parameters of short-lived particles by combining already found registered long-lived charged particles into

possible decay channels according their identified particle types (particle IDs). In addition, a performance module is implemented, which allows to monitor the reconstruction and selection at all stages. The FLES package is platform and operating system independent. It will be used in the CBM experiment for the online selection and the offline analysis on a dedicated many-core CPU/GPU farm. The farm is currently estimated to have a compute power equivalent to 60 000 modern CPU cores.

As it was mentioned above, the measured raw data will be provided to the FLES farm within time intervals, so-called time slices. The size of the time slice will be adjusted to the hardware architecture of the compute nodes [62]. Typically a time slice will contain about 1000 collisions (events) corresponding to the number of cores in a compute node in order to run on average one event per core. At the maximal interaction rate of 10 MHz, the average time between subsequent events is 100 ns. The typical duration of one event is larger than 30 ns, which is equal to the time of flight of particles with $\beta = 1$ through the detector setup. This means that many events will overlap in time. Since events are not determined by a hardware trigger before the reconstruction stage, the time slices have to be fully reconstructed and events isolated from each other in real time by the CA Track Finder [68, 69].

Fig. 3.15 (right) illustrates the challenge of the First Level Event Selection task on an example of a UrQMD[3] simulated central Au+Au collision at 25 GeV/n energy with about 1000 charged particles (different colors correspond to different types of particles). Here the decay $\bar{\Omega}^+ \to \bar{\Lambda} K^+$ with $\bar{\Lambda} \to \bar{p}\pi^+$ is of particular interest in this collision and should be found as a trigger signature by the FLES package in real time on line with the experiment [64, 65].

[3]The Ultrarelativistic Quantum Molecular Dynamics model [71, 72] is a microscopic model used to simulate (ultra)relativistic heavy ion collisions.

Chapter 4

Many-core CPU/GPU architectures

Modern large-scale high energy and heavy ion physics experiments produce huge amounts of experimental data that must often be processed in real time. This has led to the active use of powerful high performance computer clusters in such experiments. Fast and highly efficient reconstruction and analysis algorithms are being developed to process experimental data on such computer clusters. These algorithms must also be optimized to maximize the efficient use of computer resources. For this purpose, in addition to the traditional use of complex and precise mathematical methods, the algorithms should be optimized to operate with parallel streams of experimental data for their efficient and parallel processing on many-core computer systems.

The KF Particle Finder package [65] of algorithms has parallel data structures and is inherently designed for parallel data processing. Creation and development of algorithms within the package is therefore done from the beginning using parallel programming methods both at the level of vector registers using SIMD instructions, and at the level of parallel data processing on several cores of many-core computer systems.

4.1 Computer architectures

The beginning of the practical development of computer technology can be considered the pioneering work of the German engineer Konrad Zuse, which he began in 1935, and already in May 1941 he created the first fully functioning programmable computer Z3 [73].

Also in the 1930s, at the request of the U.S. government, Harvard University and Princeton University were working on the development of computer architecture for naval artillery tasks. Two types of computer architectures were proposed as a result of this work [74].

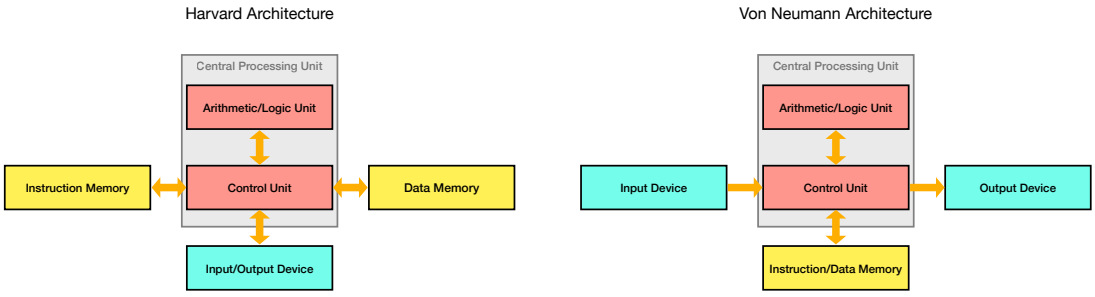

Figure 4.1: Computer architectures developed by Harvard and Princeton Universities. The main difference between these approaches is the access to memory. The Princeton architecture is better known as the von Neumann architecture.

The Harvard architecture had two different ways of transferring and storing instruction and data. In this case, memory, for example, for storing instructions and storing data could have different specific properties.

The Princeton University development (now better known as the von Neumann architecture) [75] had a central processor handling instructions and data that were stored in the same memory.

In the von Neumann architecture, an electronic digital computer consists of the following parts: a processing unit containing an arithmetic logic unit and processor registers, a control unit containing an instruction register and a program counter, memory for storing data and instructions, an external storage, and input and output mechanisms.

The main difference between these architectures [76] was that in the Harvard architecture the processor could simultaneously read instructions and access memory with data, whereas in the von Neumann architecture the instructions and data in memory were accessed sequentially. This limitation on computer system performance in Princeton University's approach is often referred to as the "von Neumann bottleneck".

Although the von Neumann architecture was chosen at the time as being simpler to implement, most modern computers, having shared memory for storing both instructions and data, present a mixture of both approaches at the cache memory level, providing separate caches or separate access paths for data and instructions (the so-called modified Harvard architecture), to more efficiently load the CPU.

Cache memory is a smaller, faster memory that stores copies of often-used data from main memory. Cache memory is used by the computer's CPU to reduce the time it takes to access data from main memory. To speed up data access, many computers use multiple levels of caches where small fast caches are expanded by larger but slower caches. These multilevel caches usually work in a way that the fastest first level cache (L1) is checked first; if data is found, the processor

continues to run at high speed. If there is a miss, the next slower cache (L2) is checked, and so on, until the main memory is checked at the very end if necessary. As the difference in access speed between the main memory and the fastest cache became larger and larger, some processors began to use up to three levels of cache.

In 1965, Electronics Magazine asked Gordon Moore, then director of research and development at Fairchild Semiconductor, to predict what would happen in the semiconductor industry over the next 10 years. And in a paper that was published on April 19, 1965 [77], Moore made the statement that the number of components in an integrated circuit was doubling about every year, and predicted that this would continue for the next ten years. He subsequently revised the predicted rate slightly to an approximate doubling every two years. This prediction later became known as "Moore's Law" and had a widespread impact on the development and miniaturization in many areas of the semiconductor industry. This progress in miniaturization of semiconductor components then led to the possibility of multiple computing cores in a single central processing unit.

The creation of multi-core processors again raised the question of structure and organization of different levels of cache memory and their distribution between processor cores. As a result, for example, in an 8-core processor with three levels of cache memory, it was decided that each core has a first level L1 cache, one intermediate level L2 cache is created for each pair of cores and a common L3 cache is created for all cores of the central processor. To increase concurrency level when L3 cache (so called last level cache, LLC) is shared by several cores, additional techniques can be used such as splitting it into several parts which correspond to certain main memory address ranges and can be available for cores independently of each other. The use of multilevel caches also leads to other more complex memory cache storage organizations. For example, in some processors all data in the L1 cache must be in the L2 cache as well. These are what are called strictly inclusive caches. Other processors have exclusive caches where the data can be in no more than one of the L1 and L2 caches but never in both. One advantage of strictly inclusive caches is that in a multiprocessor system it is sufficient to remove data from L2 cache memory in the processor and the removal from L1 memory will be done automatically. In exclusive caches, the L1 memory must also be checked.

Multiprocessor computer systems can be organized as a symmetric hardware and software architecture, where two or more of the same processors are connected to a common memory, have full access to all input and output devices, and are controlled by the same operating system. The operating system in this case sees all processors equally, without allocating any of them to any special purpose. The disadvantage of such symmetric multiprocessing (SMP) with increasing number of processors is increasing competition between processors to access shared memory,

and thus to significantly slow down the whole system.

Another approach in the architecture of computer systems, more effective with a large number of processors or cores, is the so-called non-uniform memory access (NUMA). In this case each processor has its own memory and can also access the memory of other processors. With this memory organization a processor has fast access to its own local memory and slower access to the local memory of other processors. This NUMA architecture has significant scalability advantages over symmetric multiprocessor SMP architectures.

Simultaneously with the development of multicore CPUs, GPU graphics cards were also rapidly evolving for computational purposes. While multicore CPUs have a large fraction of transistors dedicated to control and caching, multicore GPUs have a large fraction of transistors dedicated to computing modules. As a consequence of this, the computational performance of many-core graphics cards can exceed the computational performance of many-core CPUs in many cases significantly, if not by an order of magnitude. The bottleneck here, however, is the data transfer between many-core CPUs and many-core GPUs over the PCIe (Peripheral Component Interconnect Express) bus, which determines the maximum bandwidth. Therefore, in order to use graphics cards more effectively, they must be organized so that data exchange between the CPU and GPU is done as less as possible, and the graphics cards themselves work as long as possible independently of the CPU.

4.2 Levels of parallelism in computer systems

In 1966, Stanford University professor Michael Flynn proposed a four-category classification of multiprocessor computer architectures [78] (Fig. 4.2). This classification later became popular and is now used in the discussion and design of modern processors, as well as approaches in programming for such architectures. Within this classification there are usually four categories.

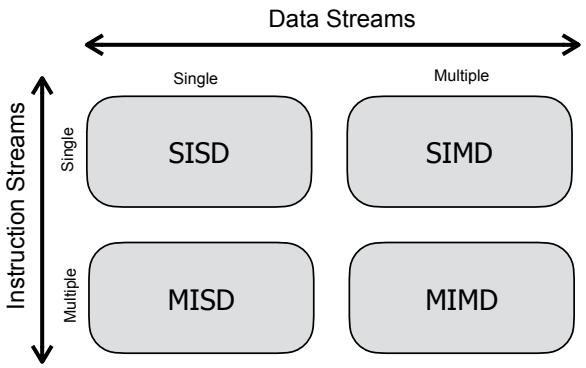

Figure 4.2: Flynn's classification of multiprocessor computer architectures.

The first, SISD, is when one processor performs one operation over the data stored in one memory cell. These are normal scalar operations.

Second, SIMD — when several processors perform the same operation on data stored in several memory cells. This is so called vector calculations.

The third one, MISD — when some processors execute some operations on data stored in one memory location. This includes, for example, pipelining architectures.

And the fourth, MIMD — when several processors perform several operations on data stored in several memory locations. These are common asynchronous parallel computations, e.g., on a computer farm in a batch mode.

The SISD model of a subscalar processor performs instruction execution in five steps:

instruction fetch, instruction decoding, execution, memory access, write back.

In this model only one instruction is executed per clock cycle and the processor must wait for the instruction to complete before executing the next instruction. Although this model allows for scalar performance (one instruction per clock cycle), in practice it is almost always subscalar (less than one instruction per clock cycle).

The easiest way to improve performance is to create an instruction pipeline, where execution of the next instruction begins before the previous one finishes. Instruction pipelining is used in almost all modern general purpose processors.

However, in this approach, situations may arise where the result of the previous operation must be present in order to execute the next operation. This is the so-called data dependency conflict condition. To solve such problems, additional checks for such conditions are needed, as well as delaying the execution of the remainder of the instruction pipeline.

In superscalar SISD models, in addition to the long instruction pipeline, several identical execution blocks are added. In this model, instructions that are independent and can be executed in parallel are distributed across available execution blocks, where they are executed simultaneously. It is clear that this requires the instruction pipeline to be filled as often as possible, which means that superscalar architectures require significant amounts of processor cache memory. In addition, to maintain a high level of performance, speculative execution, out-of-order instruction execution and branch prediction, which already belongs to the MISD category, are required. This requires even more complex CPU architectures and very advanced compilers capable of maximizing code optimization and efficient use of CPU computing resources.

Single-instruction, multiple-data parallelism (SIMD) refers to computers with multiple computational elements, which perform the same operation on multiple

data elements simultaneously. In such parallelism, only one process (an instruction) is executed at a given time at the data level. Most modern processors incorporate SIMD architecture to significantly improve performance, for example, when performing multimedia tasks.

Some of the challenges of SIMD architectures are that they require long register files, which increases power consumption. Also, not all algorithms can be easily vectorized, so it requires intensive work by programmers to solve numerous low level problems, since auto-vectorization in compilers gives a low algorithm acceleration factor and may not be stable even with minor code changes.

The extensive development of computer technologies resulted in the fact that in the beginning of 2000s, central processors became large and power-consuming devices, an example of which is the Intel Pentium 4. By this time there were two important problems that needed to be solved. The first was the growing discrepancy between the operating clock frequencies of the CPU and the main memory. Secondly, it was an increasing thermal dissipation of CPU power, which made it impossible to increase CPU performance further by increasing their clock frequency.

One solution to these problems was the development of multi-threading. This approach is more economical than the development of multi-processing because only a small number of CPU components need to be duplicated to support multi-threading, as opposed to duplicating the entire CPU in the case of multi-processing. Also with multi-threading, some modules, such as execution and memory, including the cache, are shared by multiple threads, which can significantly improve system performance when threads work in parallel with the same data.

One type of multi-threading is so-called block multi-threading, where one thread is executed until it stops waiting to obtain data from the (slow) main memory. At that point the processor can switch in one clock cycle to another thread ready to execute.

It is believed that, on average, multi-threading leads to a 30% increase in CPU performance at the expense of a 5% increase in its semiconductor components.

The disadvantage of multi-threading is that its effective support requires significant changes in operating systems.

Another strategy to increase the performance of computer systems was the development of multi-processing. At first it was symmetric multi-processing (SMP), where a small number of CPUs work in parallel, using shared memory. It became clear fairly quickly that SMP systems were limited by a small number of processors and could not be scalable. To further improve performance with more processors running concurrently and in parallel, the non-uniform memory access (NUMA) scheme described above was proposed. Such NUMA systems were well

scalable and could reach tens or even hundreds of processors working simultaneously and in parallel.

Such multi-processor systems could be built, for example, as several processors on one motherboard with connections between them. If implemented on a single silicon chip, such a CPU is called a many-core processor. Many-core processors are MIMD machines.

An important subcategory of the MIMD class is SPMD (Single Program, Multiple Data), when several co-operating processes execute one program. GPUs are examples of SPMD. SPMD has a lot in common with SIMDs as well. A SIMD machine executes a program on different data in a synchronous mode, whereas an SPMD machine also executes the same program on multiple data, but unlike SIMD, not necessarily in a synchronous mode. Therefore, SPMD is sometimes also called SIMT (Single Instruction, Multiple Threads) to emphasize its similarity to SIMD.

4.3 Parallel programming methods

In order to effectively use computer resources with multiple levels of parallelism, appropriate software is also needed.

In particular, modern CPUs, especially GPUs, require the special creation of parallel data streams to effectively use the parallelism at the data level. For example, in CPU architectures the processing of such parallel streams is implemented by SIMD-registers and instructions. One SIMD-register can store 4, 8 or 16 values in single precision depending on the register length, and one SIMD-instruction can perform respectively 4, 8 or 16 operations with these values which potentially can lead to the corresponding speed-up of the algorithm.

Modern compilers, such as C++, can automatically convert scalar codes to SIMD instructions in a process called auto-vectorization. However, compilers are not able to vectorize any code to its most effective parallel version without active participation of the developer of this algorithm. This refers, first of all, to large loops with potentially high level of parallelization when they include calls of functions or other code blocks.

One of the highly efficient ways to solve the problem of parallel vector programming using SIMD instructions is the Vc library, developed at the University of Frankfurt by Matthias Kretz. In the Vc library, parallelism is added through a system of variable types and control structures.

To parallelize algorithms between threads or cores, the most convenient approach is provided by OpenMP (Open Multi-Processing) technology. OpenMP works with a ready sequential program, which is parallelized using a set of compiler

directives, environment variables and library procedures for creating multi-threaded tasks on multi-processor systems with shared memory. OpenMP supports shared data for concurrently executed threads without transferring data between processors.

The advantage of OpenMP is that it allows developing parallel programs step by step, gradually transforming sequential blocks of programs into their parallel equivalents. This greatly simplifies the process of creating and debugging a parallel program on the basis of an already existing and well tested sequential program.

Since not all the program blocks are suitable for parallelization, the program created with the help of OpenMP technology consists of sequential (single-threaded) and parallel (multi-threaded) blocks. In this case, "Fork – Join" parallelization model is used in OpenMP when at first only one main thread works and after that a group of parallel threads is created. In the created group, all the parallel threads, including the main thread, execute the same program code. After execution of the parallel construction, all the parallel threads are joined back to the main thread.

To evaluate the efficiency of paralleling algorithms, the American computer architect Gene Amdahl formulated a rule which later became known as Amdahl's law [76] (Fig. 4.3).

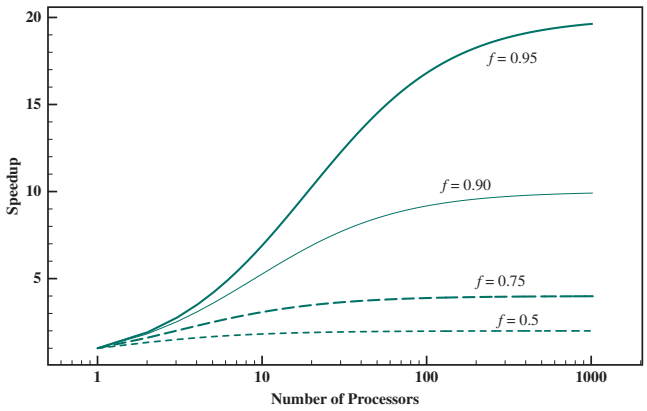

Figure 4.3: Amdahl's law for multi-processors [76].

In his approach, the performance growth of a program with a sequential fraction f is characterized by the speedup factor S when the program is executed in parallel on N processors:

$$S(N) = \frac{1}{f - (1 - f)/N}. \tag{4.1}$$

In the ideal case it is possible to get a perfect linear speedup, when as the number of processors used increases, the speed of the program increases by the same factor. Even faster superlinear speedup is possible, if processors use a common cache memory, where data are stored on demand of the first processor, and others

can use this cache-loaded data already and thus they do not need to access the slow main memory. Otherwise, the maximum speedup is determined by the size of the sequential part of the program, which by definition cannot be accelerated by adding other processors. Thus, if the sequential part of the program takes 50%, the maximum speedup by adding other processors can only be a factor of 2, even with the addition of an infinite number of processors.

Chapter 5

Search for short-lived particles

As it was mention in Chapter 1, Introduction, one of possible classifications of the elementary particles is according to their lifetime, that has a direct relation to the particle detection.

Stable particles and particles with a lifetime of up to 10^{-8} seconds, sufficient for a full or partial traverse of the detector system, are usually registered, and their trajectories, and hence the parameters of the particles, are then directly estimated by the software reconstruction algorithms. These are, for instance, electrons and positrons, muons $\mu^{\pm}$, $\pi^{\pm}$ and $K^{\pm}$ mesons, and protons.

On the other hand, particles with a shorter lifetime as well as resonances can not be registered in the detector system because of their very short lifetime, such that they simply do not have enough time even to reach the first detector stations. Such particles and resonances (so-called short-lived particles) are found by using their decay products, which usually have a sufficient lifetime for their registration in the detector system. Here among others are particles of particular interest for the CBM experiment: strange hyperons (Λ, Ξ, Ω), low-mass vector mesons (ρ, ω, ϕ), charmed particles (D mesons, J/ψ), and hypernuclei (${}^{3}_{\Lambda}\mathrm{H}$, ${}^{4}_{\Lambda}\mathrm{H}$, ${}^{4}_{\Lambda}\mathrm{He}$).

5.1 The KF Particle package

The KF Particle package [65, 66, 67] for reconstruction of short-lived particles is based on the Kalman filter (KF) approach, hence the name of the package. In the package the daughter and mother particles are described with the same set of parameters and are treated in exactly the same way, therefore the reconstruction of decay chains is simple and straightforward. The package is geometry independent and, therefore, portable to other experiments.

Since the KF Particle package based on the Kalman filter, it defines the state vector [65], which includes eight parameters for description of real physics particles:

three coordinates of the particle (x, y, z), three components of its momentum (p_x, p_y, p_z), the energy of the particle (E) and, in case a production point of the particle is known, the time between the production and decay points measured as a distance normalized to the particle momentum ($s = l/p$):

$$\mathbf{r} = \{x, y, z, p_x, p_y, p_z, E, s\}. \tag{5.1}$$

The covariance matrix is calculated in the Kalman filter approach together with the state vector estimation that allows to obtain the accuracy of the estimated particle parameters and to calculate the χ^2-value, which gives the quality of the mother particle reconstruction.

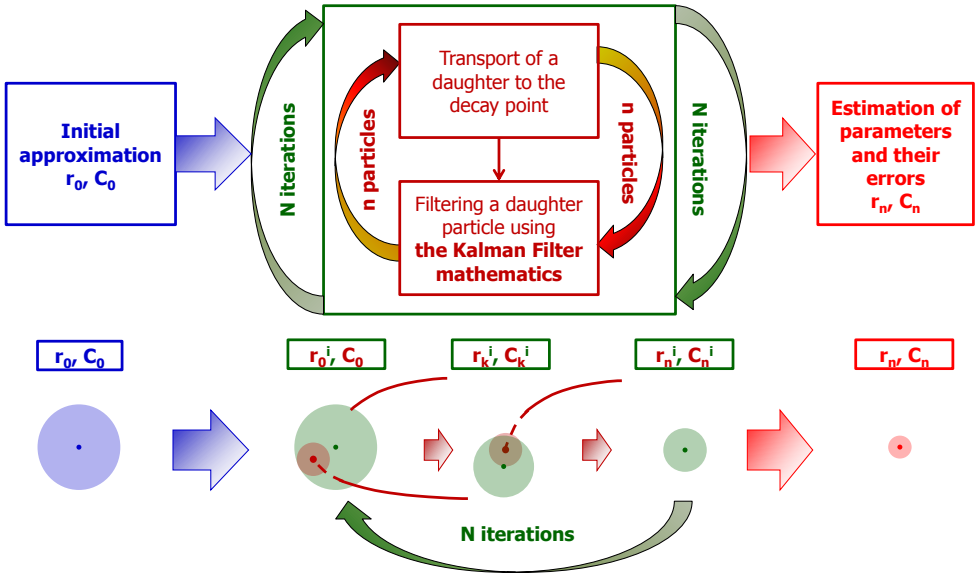

Figure 5.1: Block diagram of short-lived particle reconstruction in the KF Particle package [65].

In the KF Particle package the standard Kalman filter approach is used for the reconstruction of short-lived particles (Fig. 5.1):

1. initialization of the mother particle parameters;
2. extrapolation of the daughter particle to the point of the closest approach to the estimated decay point;
3. correction of the mother particle parameters using the daughter particle as a measurement in the Kalman filter procedure.

The KF Particle package provides rich functionality, some of which are listed below:

- construction of the mother particle from the daughter particles;
- transport of any particle to any arbitrary point, to the decay and production points, to another particle or on a certain distance;
- calculation of the deviation from another particle or from the decay point in terms of χ^2;
- setting constraints in the state vector on the particle mass and on the production point of the mother particle.

In addition, the KF Particle package provides a simple and intuitive access to the physics parameters of the reconstructed particles, like the mass, momentum, decay length, lifetime and rapidity, together with their errors for further physics analysis.

5.2 The KF Particle Finder package

For a comprehensive study of the properties of the quark-gluon plasma, it is necessary to analyze all, without exception, collisions of heavy ions. This imposes a requirement to reconstruct all stable and short-lived particles, both the participants and those produced in the process of the collision. Moreover, the high interaction rate in the CBM experiment makes it possible to analyze rare signal particles, signatures, which have very low yields (multiplicity $\times$ branching ratio, as shown in Fig. 3.3, left) and, therefore, are produced in collisions with very small probabilities. This, in turn, requires also the selection of collisions with such rare particles in real time on line with the experiment. Both of these requirements were raised the need to develop on the basis of the KF Particle a new package, called KF Particle Finder [65], for the search and selection of short-lived particles of particular interest for the investigation of the properties of the quark-gluon plasma.

Stable and short-lived particles, registered in the detector system, are reconstructed by the Cellular Automaton (CA) Track Finder [63, 69] and their parameters are estimated by the Kalman Filter (KF) Track Fitter [63, 70]. The subsequent particle identification is done with downstream PID subdetectors, such as the Time-Of-Flight detector.

Finally, the search for short-lived particles, which are not registered in the detector system, is performed by the KF Particle Finder package. First, all particles are divided into groups of primary and secondary particles. The primary particles are those participated or produced in the collision. Their reconstructed trajectories should point to the (already reconstructed) primary interaction point (the

primary vertex) within the errors of the propagated track parameters. As a quantity of the cut a so-called χ^2_{prim} is used, which is the deviation of the propagated trajectory (track) from the primary vertex in terms of χ^2. If $\chi^2_{\text{prim}} > 18.4$, then the track can originate from the primary vertex with the probability $< 0.01\%$ and, therefore, can be reliably considered as secondary. With this cut on χ^2_{prim} the contribution of the primary tracks to the background of the reconstructed short-lived particles will be minimized. After that all tracks (primary and secondary) are sorted separately according to their electric charge (negative or positive).

In addition, grouping according to their PID is performed within each of these four groups. In case no PID is associated with a particle, it is considered a pion as the most abundant particle produced in the collisions. This assumption allows to use in physics analysis also those particles, which are not within the acceptance of the PID detectors. Being pions with high probability these particles increase the signal with pions in the decay channels, but do not contribute significantly to the background formation due to a possible misidentification keeping the signal-to-background ratio stable.

After all preparations are done, the KF Particle Finder searches for short-lived particles following the (simplified) block-diagram shown in Fig. 5.2. The daughter particles are combined into the mother particle candidates according to their PID hypothesis and the corresponding decay channels.

First, two-body decays are considered and their candidate mother particles are constructed from one positive and one negative secondary tracks. These are mainly strange particles and open charm.

Mother particles, that decay at the collision point, including resonances, low-mass vector mesons and charmonium, are constructed by combining one positive and one negative primary tracks.

For reconstruction of $\gamma \to e^+e^-$ conversions all electrons are combined with all positrons, since the conversion can happen everywhere in the detector volume, especially in the detector material.

The background sample is formed from the mother particle candidates of two types. First, the combinatorial background, these are arbitrary combinations of daughter tracks originating from different decays. Second, the physical background of the mother particle candidates constructed from the daughter tracks with an incorrectly assigned PID hypothesis. While the combinatorial background can be suppressed using the cuts on the fit quality and the decay topology, the physical background can be reduced only by improving the particle identification.

In order to suppress the background a set of cuts is applied to select the candidates:

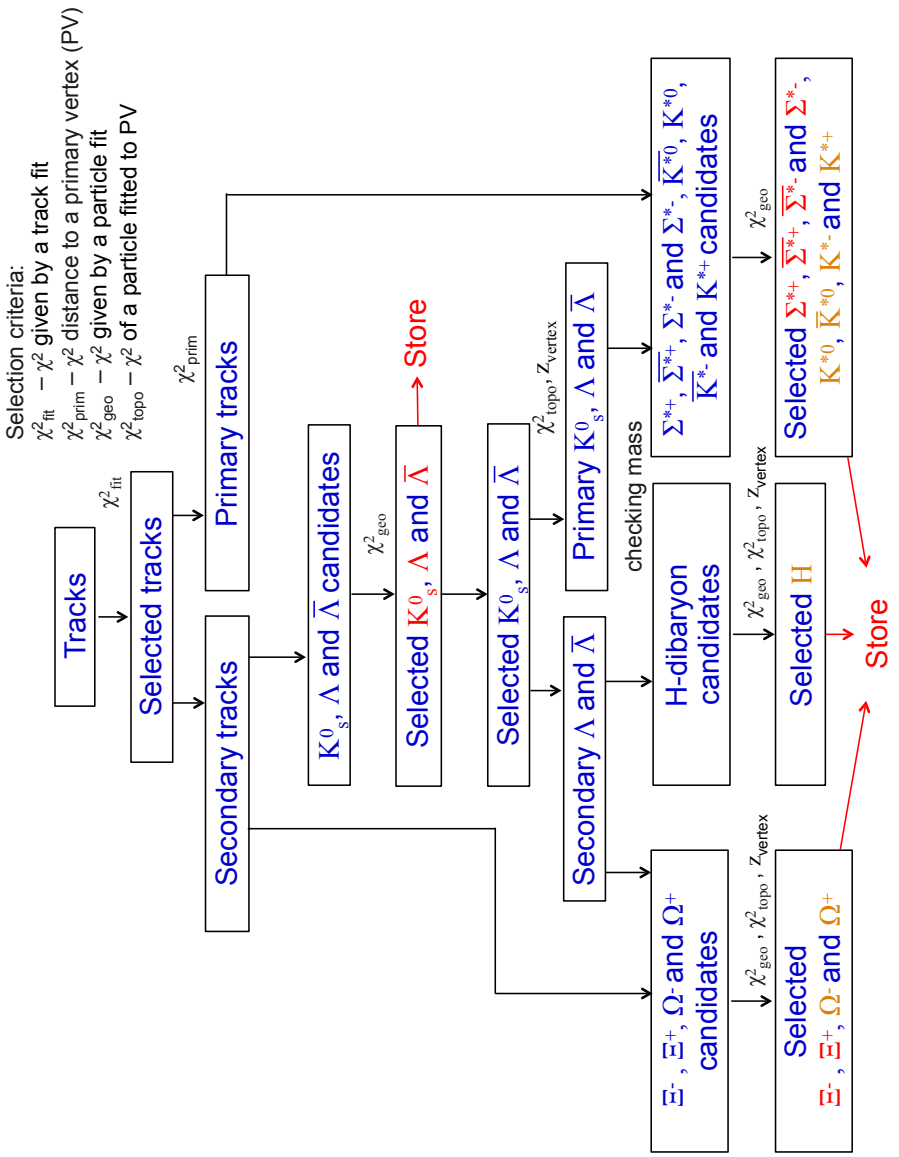

Figure 5.2: A simplified block diagram of the KF Particle Finder package, illustrated with some decay channels.

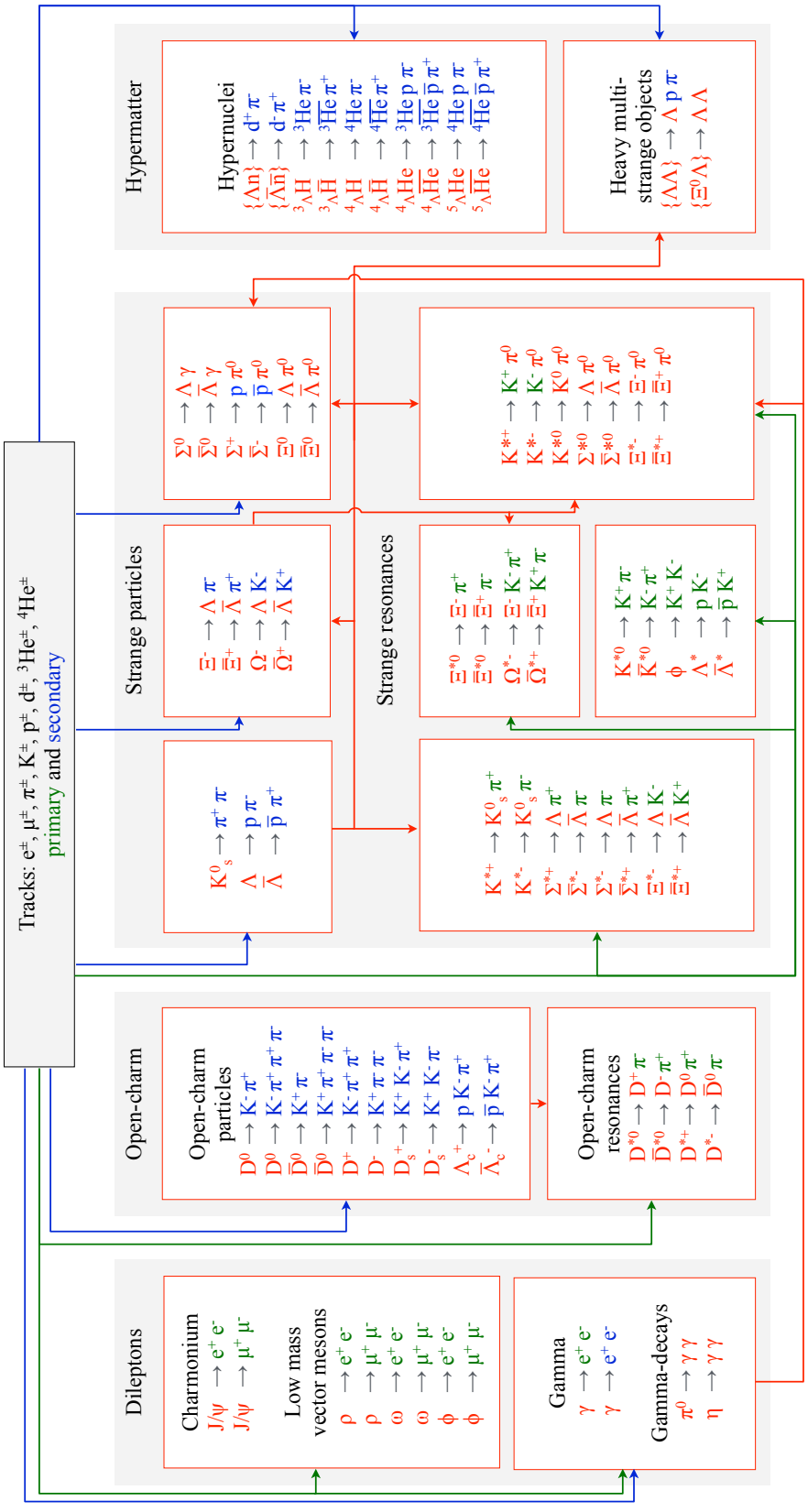

Figure 5.3: Block diagram of the KF Particle Finder [65].

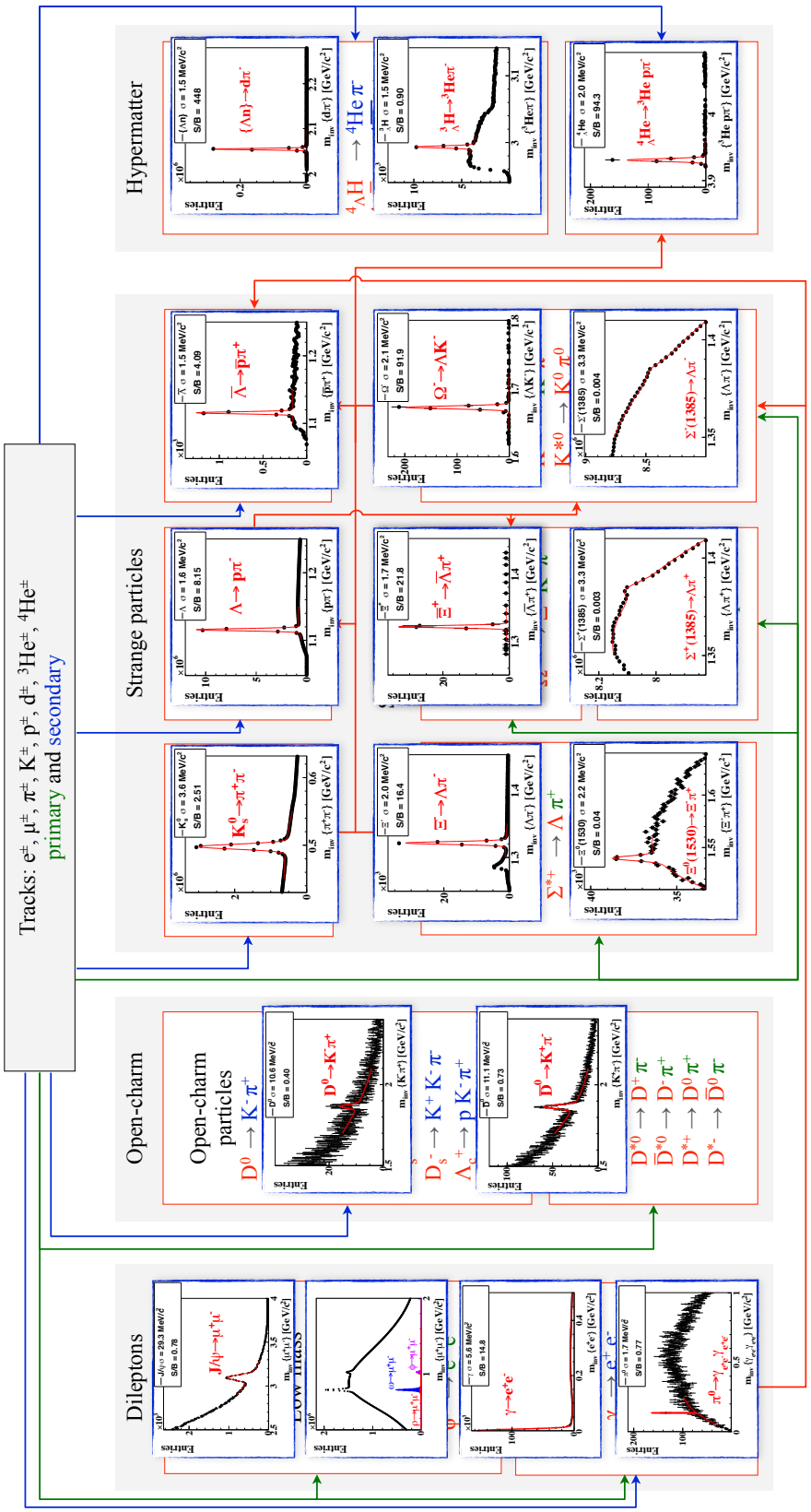

Figure 5.4: Some histograms produced by the KF Particle Finder package [65].

- a cut on the χ^2_{fit}/ndf (here ndf is the number of degrees of freedom) criterion, which characterizes whether the trajectories of the daughter particles intersect within their errors;
- a cut on the χ^2_{topo}/ndf, which characterizes whether the particle is produced in the primary vertex region: the smaller the obtained value, the larger probability, that the trajectory of the particle overlaps the primary vertex area within the errors;
- a cut l/σ_l on the distance from the primary vertex to the decay point normalized on its error, that shows how well the decay point is separated from the primary vertex.

The cuts for different groups of decays are optimized with respect to the corresponding particle yields, branching ratios and decay properties. The particle candidates, which pass all cuts, are stored.

For the reconstruction of decay chains, that appears, for instance, in decays of multi-strange hyperons, the already reconstructed secondary Λ and $\bar{\Lambda}$ are selected and then considered as daughter particles for further analysis in a similar way as described above.

The KF Particle Finder package includes the search for several dozens of short-lived particle decays (see Fig. 5.3). The package is developed to reconstruct signals from all the physics cases of the CBM experiment, including strange particles, strange resonances, hypernuclei, low-mass vector mesons, charmonium and open-charm particles. This makes the KF Particle Finder a universal platform for short-lived particle reconstruction and physics analysis.

5.3 Tools for analysis of particle spectra

The main purpose of analyzing short-lived particles is to extract the physics characteristics that describe the system produced by heavy ion collisions. One of such characteristics is the yield of particles as a function of momentum, rapidity, transverse mass, etc. To solve this problem in the KF Particle Finder package two methods are implemented:

1. side-bands method,
2. multi-differential analysis method.

The *side-bands method* is intuitive and easy to understand. It is based on the assumption (which is verified by observation in the presence of sufficient statistics) that the background in the signal peak region ($\pm 3\sigma$) has properties very similar

to those of the background immediately outside the peak region $(-6\sigma, -3\sigma)$ and $(3\sigma, 6\sigma)$ in terms of shape of spectra in momentum and rapidity. In this case, the similar background of the side-band parts can be subtracted from the central region to obtain a clean signal. Obviously, in the simplest case, when the background has the form of a straight line, the integral under the peak is equal to the integral in the vicinity of the peak. That is, the main task here is to estimate the ratio of the background inside and outside the signal area and calculate the correction factor before subtracting the background from the peak area to keep the proportion equal.

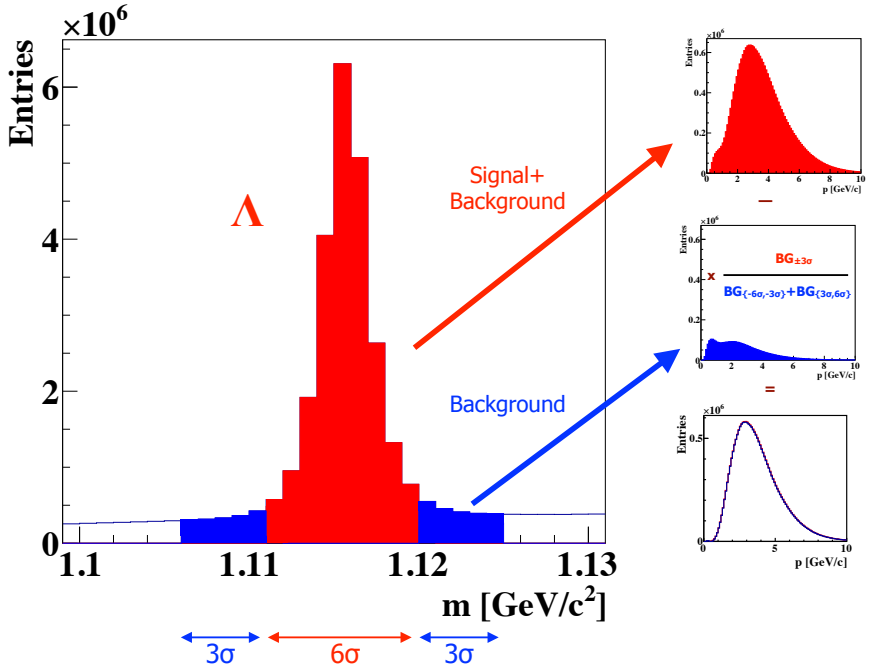

Figure 5.5: A visual representation of the side-bands method. In the final spectrum on the bottom right, one can see that the reconstructed spectrum (blue line) is almost indistinguishable from the simulated spectrum (red line).

The side-bands method is implemented in the KF Particle Finder package as the following procedure (Fig. 5.5):

1. spectra of particles by mass, momentum, transverse momentum, rapidity, as well as the distribution of decay vertices along the axis z are produced;
2. the mass spectrum is approximated in the peak region to estimate the signal along with the background, and in the side-bands around it to estimate the background;
3. a correction factor is calculated to determine the background in the area of the signal peak;

4. the corrected background of the side-bands is subtracted from the signal peak area;

5. the spectra of particles by mass, momentum, transverse momentum, and rapidity, as well as the distribution of decay vertices along the z-axis, are produced cleaned from the background contribution.

The side-bands method is very fast, does not require much data, and gives a good overall result based on an average approximation, which, however, does not take into account the local features of the (y, p_t) space.

As an alternative approach for solving this problem in the KF Particle Finder package, the *multi-differential analysis* method is also implemented. This method is more complex and allows taking into account the features of spectra in different regions (y, p_t), which, however, requires much more statistics, as well as more time for calculations, as it depends on the number of bins when splitting the spectrum. To obtain the following results, a partitioning of (y, p_t) into 10 000 bins was used.

The implementation of the multi-differential analysis method consists of the following steps:

1. The entire phase space (y, p_t) is partitioned into sufficiently small bins;

2. individual mass spectra are produced in each of the bins;

3. in each individual bin, the mass spectrum is approximated by a function of the form "signal + background";

4. from the approximation parameters an estimate of the number of signal inputs in each bin is taken;

5. the whole region (y, p_t) is filled in each bin with the obtained corresponding number of signal inputs;

6. since the obtained distribution $y - p_t - m$ also contains information about other physics parameters, we can further select any of them $(y, p_t, p, m, m_t, z_{decay})$ and build the histograms of interest.

The multi-differential analysis, similar to the side-bands method, also shows very good agreement with the original simulated data (Fig. 5.6), especially in regions where bins have statistically many inputs.

Also added to the KF Particle Finder is the ability to set efficiency plots that allow one to reconstruct the distributions of particles produced by the collision. The $K_s^0 \to \pi^+\pi^-$ decay efficiency-corrected spectra obtained by both methods are shown in Fig. 5.7 (left) for example m_t and y–m_t for 5 M central Au+Au events

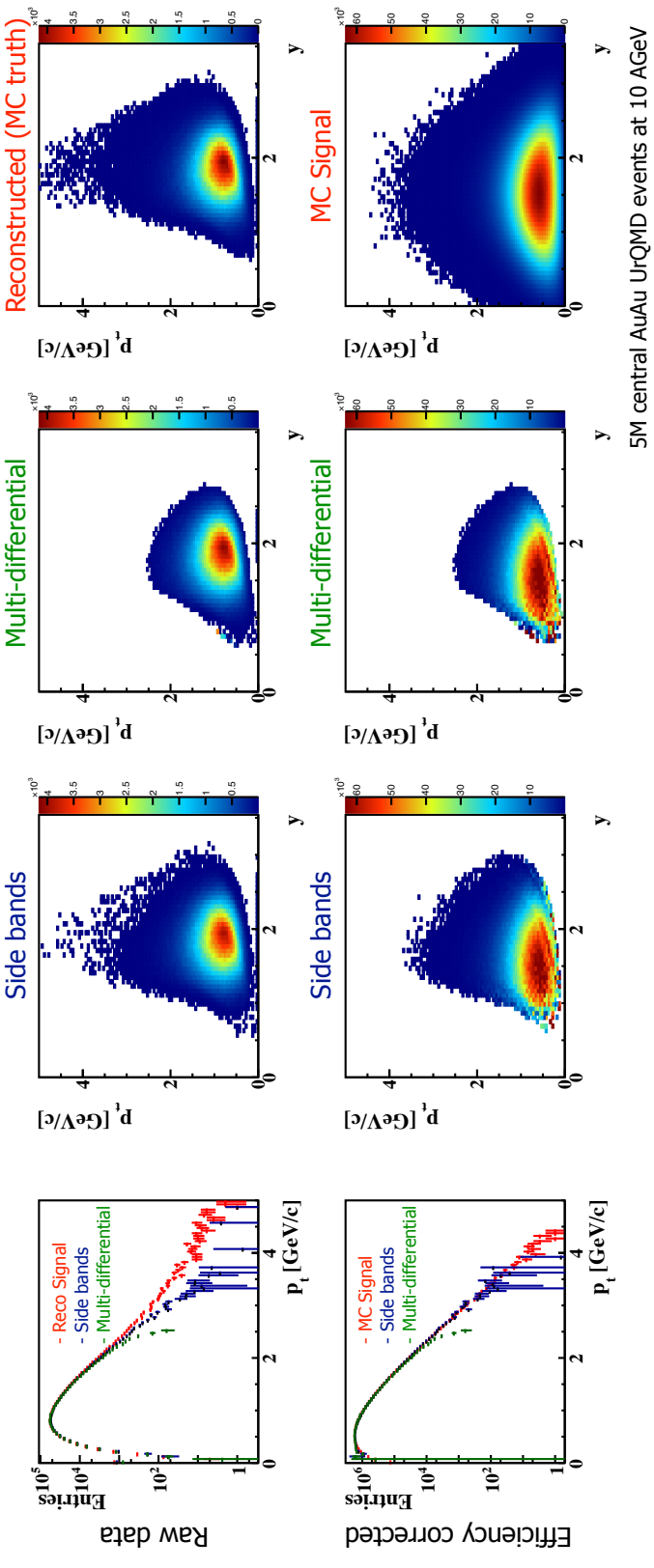

Figure 5.6: Comparison of the results of the side-bands method and the multi-differential analysis method in the reconstruction of spectra for $\Sigma^- \rightarrow n\pi^-$ decay. The bottom row shows histograms corrected for 4π efficiency, which when compared to the top row gives an idea of the CBM experiment [A12, A13] detector system acceptance.

in UrQMD model at 10 GeV/n collision energy. The reconstructed spectra are in good agreement with each other and with the simulated Monte Carlo spectra.

The resulting m_t spectra can be further analyzed, for example, in different bins of rapidity, as shown in Fig. 5.7 (left): both reconstructed and simulated distributions are fitted by exponential functions, giving the slope parameter. Assuming that the generated particles have a thermal distribution, the temperature can be extracted from the slope parameter. As an example, the resulting efficiency-corrected y–m_t and m_t spectra for Σ^- obtained for 5 M central Au+Au events in the UrQMD model at 10 GeV/n collision energy are shown in Fig. 5.7 (right).

To summarize, new methods for physics analysis have been developed and implemented for the KF Particle Finder package to reconstruct efficiency-corrected spectra as well as to extract the inverse slope or effective temperature. Since these methods are completely independent, they also allow the systematic errors of the acquired spectra to be studied.

As a universal software package, the KF Particle Finder allows the developed methods of spectrum analysis to be applied to all decays obtained directly within its scheme of the search and reconstruction of short-lived particles.

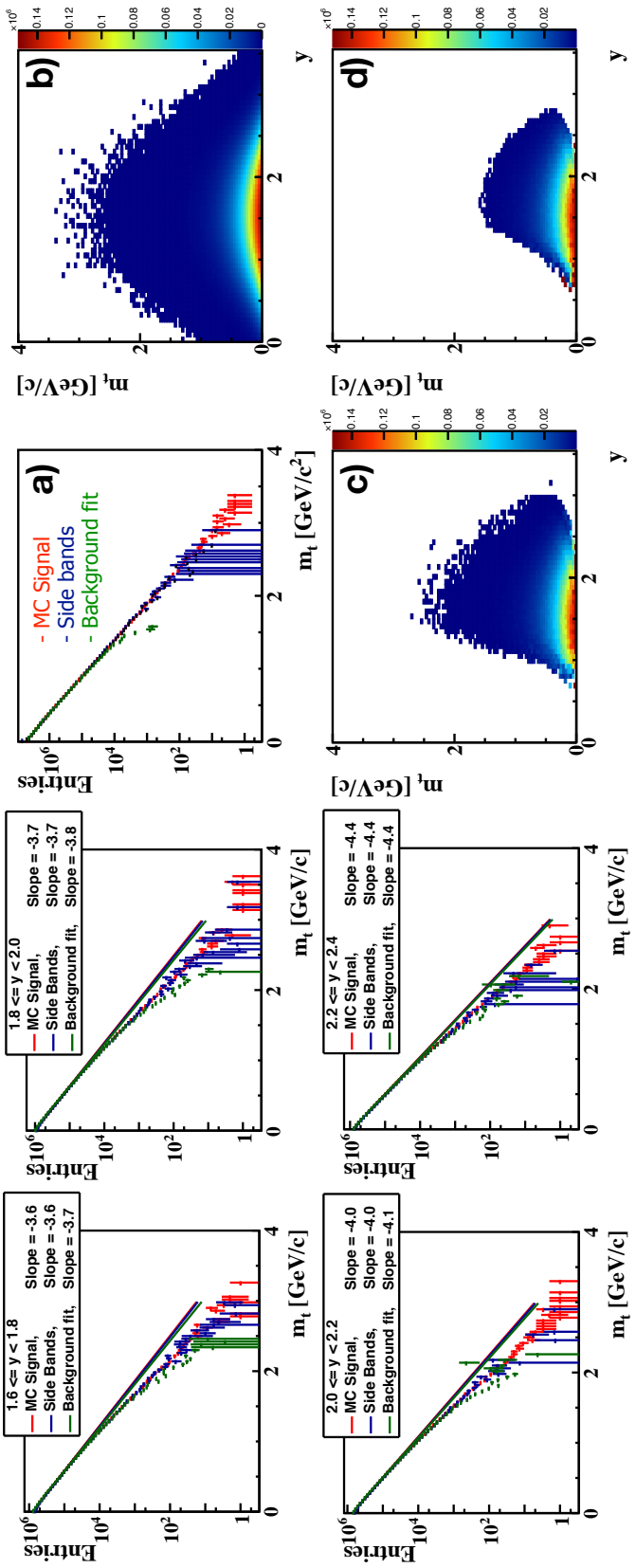

Figure 5.7: Left: Reconstructed m_t signal vs. simulated signal in various bins of rapidity at $K^0_s \to \pi^+\pi^-$ example, obtained from 5 M central Au+Au collisions in UrQMD model at 10 GeV/n collision energy [A12, A13]. Right: The Σ^- hyperon spectra as a function of (a) m_t obtained by the side-bands method and multi-differential analysis for the simulated signal, (b) y–m_t for the simulated signal, (c) y–m_t — side-bands method, (d) y–m_t — multi-differential analysis [A12, A13].

Chapter 6

The missing mass method

6.1 The relativistic kinematics

Let us start with the energy-momentum-mass relation for a particle with the rest mass m:

$$E^2 = m^2c^4 + \mathbf{p}^2c^2\,|_{\hbar=c=1} = m^2 + \mathbf{p}^2. \tag{6.1}$$

From the standard Lorentz transformation with the z-axis along the beam one can get:

$$\begin{aligned} ct' &= \gamma(ct - \beta z) & \qquad E'/c &= \gamma(E/c - \beta p_z) \\ x' &= x & \qquad p'_x &= p_x \\ y' &= y & \qquad p'_y &= p_y \\ z' &= \gamma(z - \beta ct) & \qquad p'_z &= \gamma(p_z - \beta E/c). \end{aligned}$$

Working with relativistic energies it is useful to operate with the *rapidity* instead of the particle *velocity* [82]:

$$y = \frac{1}{2}\ln\frac{E + p_zc}{E - p_zc} = \tanh^{-1}\left(\frac{p_zc}{E}\right) = \tanh^{-1}(v_z)\,, \tag{6.2}$$

with the energy of a particle E, and $v_z = p_z/E$ is the longitudinal component of the velocity.

Rapidity is additive under Lorentz boost along the beam axis:

$$y' = y - \tanh^{-1}\beta. \tag{6.3}$$

Important is that the difference between the rapidities of two particles is invariant with respect to Lorentz boost along the beam axis z:

$$y'_1 - y'_2 = (y_1 - \tanh^{-1}\beta) - (y_2 - \tanh^{-1}\beta) = y_1 - y_2. \tag{6.4}$$

Rapidity of a particle is often used together with the azimuthal angle (y, ϕ), then the angular separation of two particles $(y_2 - y_1, \phi_2 - \phi_1)$ is invariant with respect to the Lorentz boost.

In real (especially collider) experiments it is often hard to estimate the total momentum p of a particle and its z-component p_z at large rapidities, when the particle trajectory is close to the beam axis. Therefore, for relativistic particles the pseudorapidity η is introduced instead in the similar way:

$$y = \frac{1}{2} \ln \frac{E + p_z c}{E - p_z c} \simeq - \ln \tan \frac{\theta}{2},$$

hence

$$\eta = - \ln \tan \frac{\theta}{2}, \tag{6.5}$$

with $p_z/p = \cos\theta$, where θ is the angle of the particle trajectory with the beam axis, and $y \simeq \eta$ for highly relativistic particles.

Since the p_x and p_y components of the momentum and the rest mass of a particle are invariant with respect to the Lorentz boost along the beam, one can collect them and define the transverse mass of a particle as [82]:

$$\begin{aligned} m_T^2 c^4 &= m^2 c^4 + \mathbf{p}_T^2 c^2, \\ m_T &= \sqrt{m^2 + \mathbf{p}_T^2/c^2}. \end{aligned} \tag{6.6}$$

Thus, the transverse mass is invariant under Lorentz boost along the beam axis. The measured m_T-distribution of the produced particles has typically an exponential form

$$\frac{dN}{2\pi m_T dm_T} = A \cdot \mathrm{e}^{-m_T/\lambda}. \tag{6.7}$$

The parameters A and λ are usually obtained from the fit to the experimental data, particularly

$$\lambda = - \left[\frac{d}{dm_T} \ln \left(\frac{dN}{m_T dm_T} \right) \right]^{-1}, \tag{6.8}$$

with a typical λ value for pions about 200 MeV, reflecting the fact that most of the produced pions have small transverse momenta.

Similarity of the distribution (6.7) to the Boltzmann thermal factor is the reason why the *inverse slope parameter* λ is often called as an *effective temperature* of the spectrum.

6.2 Search for strange and multi-strange particles

Since colliding nuclei are composed only of u and d quarks, strange s and $\bar{s}$ quarks are created directly in the heavy ion collision process, and having a relatively

small mass of 95 MeV/c^2 they are abundantly produced particles. As already mentioned, according to the theoretical predictions the enhanced strangeness production can be an indicator of the deconfined state of the strongly interacting matter, or QGP, in the heavy ion collisions. According to the current knowledge strange and multi-strange hyperons can be produced in sequential collisions involving Ks and Λs, and, therefore, are sensitive to the density of the medium in the colliding system. This sensitivity is expected to increase towards lower beam energies close to or even below the production threshold [29]. Thus, strange and multi-strange particles are well suited for the investigation of hot and dense baryonic matter.

Table 6.1: Decay channels of strange particles analyzed in the KF Particle Finder together with their branching ratio and the lifetime ($c\tau$) [65].

Particle	Antiparticle	Branching ratio, %	$c\tau$, cm
$K^0_s \to \pi^+\pi^-$	—	69.2	2.7
$\Lambda \to p\pi^-$	$\bar{\Lambda} \to \bar{p}\pi^-$	63.9	7.9
$\Sigma^+ \to p\pi^0$	$\bar{\Sigma}^- \to \bar{p}\pi^0$	51.6	2.4
$\Sigma^0 \to \Lambda\gamma$	$\bar{\Sigma}^0 \to \bar{\Lambda}\gamma$	100.0	$2.2 \cdot 10^{-13}$
$\Xi^0 \to \Lambda\pi^0$	$\bar{\Xi}^0 \to \bar{\Lambda}\pi^0$	99.5	8.7
$\Xi^- \to \Lambda\pi^-$	$\bar{\Xi}^+ \to \bar{\Lambda}\pi^+$	99.9	4.9
$\Omega^- \to \Lambda K^-$	$\bar{\Omega}^+ \to \bar{\Lambda}K^+$	67.8	2.5

The KF Particle Finder [65] searches for the decay channels of strange particles, as listed in Table 6.1 together with their decay parameters.

The high quality of the parameters together with $c\tau$ of several cm allow reconstruction of strange particles both with the high signal-to-background (S/B) ratio and efficiency. The mass spectra of K^0_s, Λ, $\bar{\Lambda}$, Ξ^-, $\bar{\Xi}^+$, and Ω^-, obtained by the conventional KF Particle Finder method, for 5M central AuAu UrQMD events at 10 GeV/n using TOF PID are shown in Fig. 6.1. The S/B ratio is calculated in $\pm 2\sigma$ of Gaussian fit of the signal peak, the background was approximated by the second order polynomial function [65].

6.3 Basics of the missing mass method

In most cases strange particles are reconstructed using their decay products registered in the detector system. On the other hand, charged kaons K^+ and K^- have a very long lifetime with $c\tau = 3.71$ m, thus, many of them can be fully reconstructed in the tracking detectors and identified in the PID detectors. In 1992 in the NA35 experiment [7, 79] it was shown that their decays in flight,

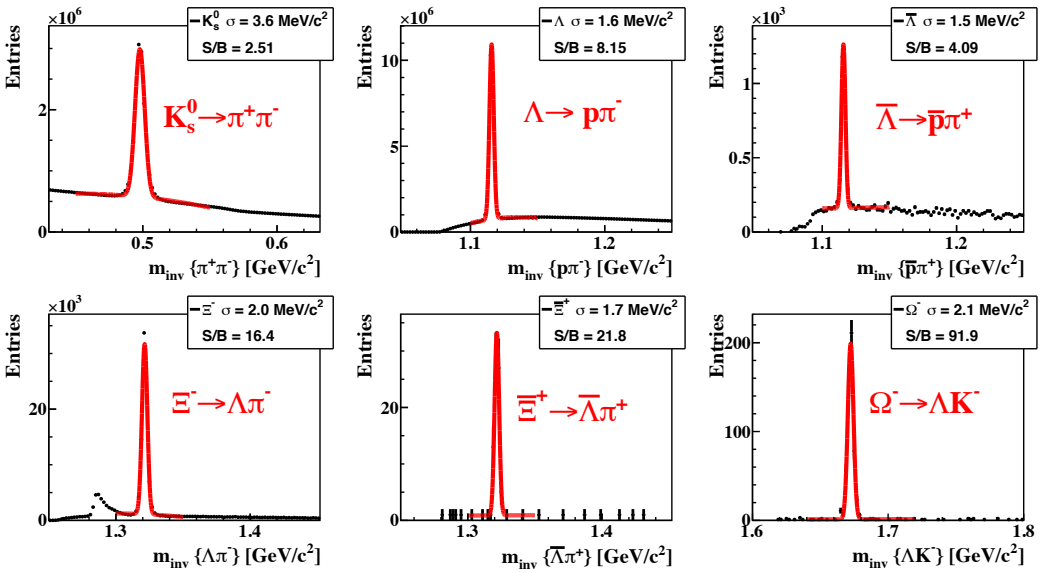

Figure 6.1: Mass spectra of K_s^0, Λ, $\bar{\Lambda}$, Ξ^-, $\bar{\Xi}^+$, and Ω^-, obtained by the conventional KF Particle Finder method, together with their signal-to-background (S/B) ratios for 5M central AuAu UrQMD events at 10 GeV/n using TOF PID [65].

appearing as *kinks* in the reconstructed trajectories, can also be used for their identifications. In the dominant kaon decays $K^\pm \to \mu^\pm\nu$ and $K^\pm \to \pi^\pm\pi^0$ transverse momenta of the decay products can take values up to, correspondingly, 236 and 205 Mev/c, which is substantially higher than the maximum transverse momentum of 30 MeV/c in the matching pion decay $\pi^\pm \to \mu^\pm\nu$ which constitute main background when search for the kaon decays. Therefore all kinks with transverse momentum exceeding 30 MeV/c can only be decays of kaons, and the loss of kaons due to this cutoff can be easily corrected for.

The developed missing mass method can be used to reconstruct decays of short-lived charged particles, when one of the daughter particles is neutral and not registered in the detector system. The method is based on the laws of conservation of energy and momentum.

As one of the important areas of research, where the application of the missing mass method plays a crucial role, let us consider the main decay channels and their probabilities for Σ^- and Σ^+ particles, as well as their antiparticles:

$$\begin{aligned}
&\Sigma^- \to n\pi^- && \overline{\Sigma}^+ \to \overline{n}\pi^+ && BR = 99.8\% \\
&\Sigma^+ \to p\pi^0 && \overline{\Sigma}^- \to \overline{p}\pi^0 && BR = 51.6\% \\
&\Sigma^+ \to n\pi^+ && \overline{\Sigma}^- \to \overline{n}\pi^- && BR = 48.3\%
\end{aligned}$$

As can be seen, they all have a neutral particle in the decay products, and the missing mass method is the only method for their reconstruction and subsequent

analysis.

Let's illustrate how the missing mass method works [A9, A10, A14, A17, A19] using decay as an example

$$\Sigma^- \rightarrow n\pi^-. \tag{6.9}$$

In this decay, the daughter pion is registered in the tracking detector and identified in one of the PID detectors, whereas the neutron, being a neutral particle, is not registered in the detector system. However, Σ^-, although it has a short lifetime $c\tau_{\Sigma^-} = 4.4$ cm, but in fixed-target experiments the average trajectory length in the laboratory coordinate system can reach 15–20 cm due to relativistic boost. In this case Σ^- can cross several tracking stations, be registered and then reconstructed. Thus, in this decay it becomes possible to reconstruct the trajectories of both charged particles, but Σ^-, unlike π^-, still cannot be identified, since it does not reach the PID detectors (Fig. 6.2, left).

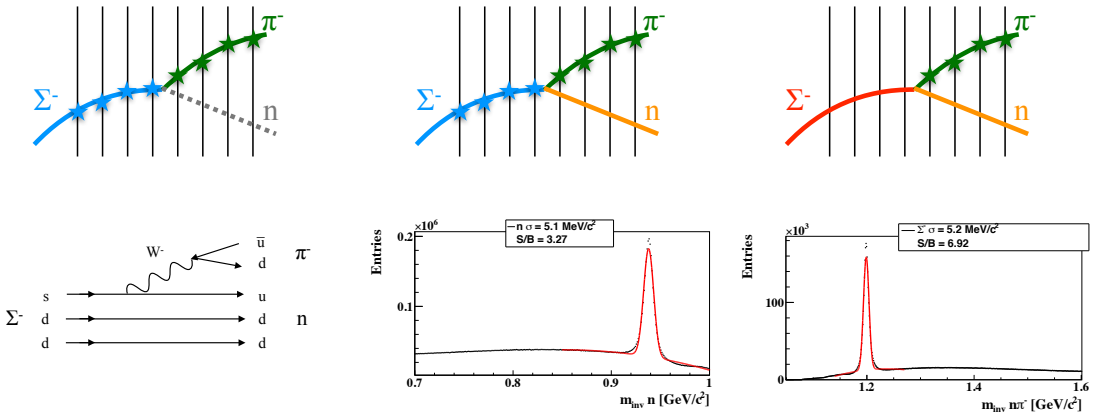

Figure 6.2: Three stages of implementing the missing-mass method in the CBM experiment: 1) reconstruction of charged particle trajectories — the parent Σ^- and the daughter π^- (left); 2) reconstruction of the neutral daughter n (middle); 3) final reconstruction of the mother Σ^- (right).

Using the parameters of the reconstructed charged particles and assuming at this stage that it is a Σ^- decay, we can find the invariant mass of the daughter neutron.

As already noted, a feature of the missing mass method is that the short-lived mother track usually cannot be identified, which makes it impossible to directly calculate the mass of the neutron. However, the momentum of the Σ^- mother particle, unlike its mass, can be determined from the curvature of its trajectory. Therefore, we can assume and apply the hypothesis about the type and mass of the mother track, and then analyze the resulting neutron mass spectrum.

Two cases are possible here (Fig. 6.2, the mass spectrum on the histogram in the middle bottom):

1. if the mother particle was indeed Σ^-, the result will be in the region of the tabulated neutron mass (0.939 GeV), where a peak-shaped distribution statistically is formed;

2. if the hypothesis is not true, such cases will give a contribution to a continuous combinatorial background in the neutron mass spectrum, created by the contribution of primary particles and secondary particles from other decays, as well as incorrectly reconstructed particles.

Then, to get the Σ^- mass spectrum, use the calculated neutron mass and determine the Σ^- mother particle state vector from the two daughter tracks n and π^-. The peak from the neutron mass spectrum will form a peak in the Σ^- mass region (1.197 GeV), while the background will keep its continuous shape and form a background in the Σ^- mass spectrum (Fig. 6.2, the mass spectrum on the histogram in the bottom right).

Thus, the reconstruction of a short-lived charged particle by the missing mass method is performed in three steps (Fig. 6.2):

1. reconstruction of the trajectories of the charged mother particle Σ^- and its charged daughter particle π^- in the tracking system;

2. reconstruction of the parameters of the neutral daughter particle n based on the parameters of the mother Σ^- and the charged daughter π^- particles;

3. reconstruction of the mass spectrum of Σ^- using the parameters of the n and π^- daughter particles.

Technically, the method is implemented as follows. The primary particles are assigned a mass hypothesis corresponding to the particle in question, for example, in the case of Σ^- the mass is 1.197 GeV, while the secondary ones — the mass corresponding to the hypothesis derived from measurements of the identification detectors. If the secondary particle, for whatever reason, has not been identified, it is treated as a pion, which is the most abundant particle produced in heavy ion collisions. The method combines all primary particles with corresponding secondary particles depending on the current hypothesis of the decay being searched for, e.g., all π^- in the case of Σ^-, or all K^- in the case of Ω^-.

Two basic conditions are checked before calculating the neutral particle parameters:

1. the first measurement of the charged daughter particle is farther away than the last measurement of the mother particle;

2. energy of the primary particle is greater than that of the secondary particle, where for the mother particle the energy is calculated according to the current hypothesis.

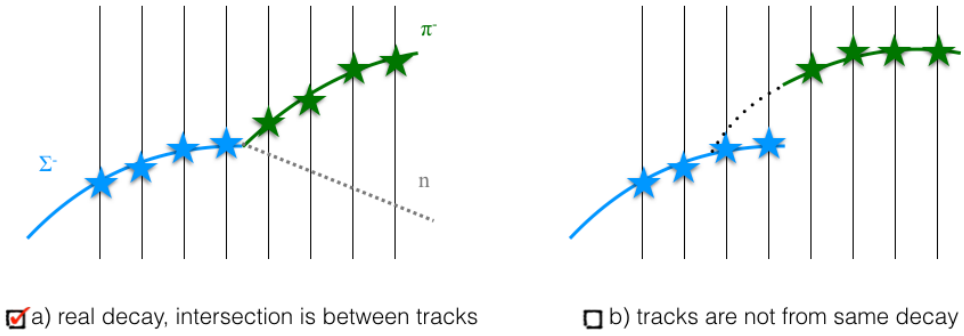

Figure 6.3: Searching for a possible decay point using reconstructed primary and secondary tracks

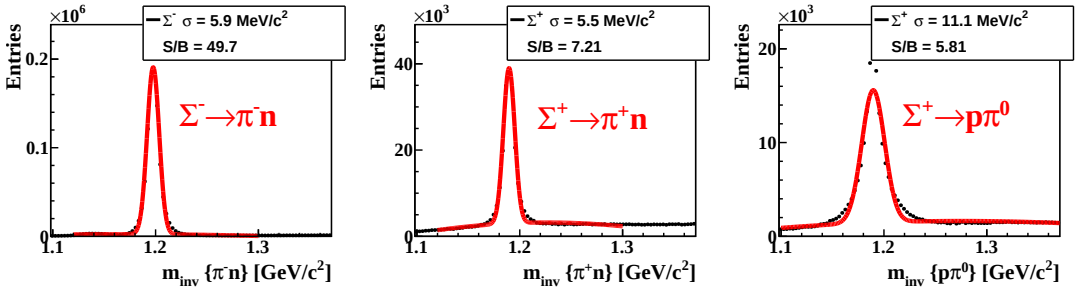

Figure 6.4: Mass distributions of $\Sigma^{\pm}$ decays with PID TOF at 5 M central Au+Au collisions at 10 GeV/n energy with increased signal-to-background ratio S/B after optimization of the selection procedure [64, A10].

If both conditions are satisfied, then the Kalman filter is applied to calculate the parameters of the neutral daughter particle at the point of closest approach of the trajectories of the charged particles. Then, checking the quality of the fitting using the χ^2 value, the cases of non-intersecting tracks are discarded. It is also checked that the decay point is located after the last measurement of the mother track and before the first measurement of the daughter track (Fig. 6.3). These requirements for the geometric position of the reconstructed decay point suppress much of the combinatorial background and have therefore been added to the KF Particle Finder package. Fig. 6.4 shows the corresponding $\Sigma^{\pm}$ decay mass distributions with PID TOF for 5 M central Au+Au collisions at 10 GeV/n energy. This study significantly improved the signal-to-background ratio, keeping the efficiency at the same level [64, A9, A10].

In the process of developing the method, the problem of clone suppression arose. In common terminology, a clone is a (second) part of an already partially reconstructed track. The study of the distribution (y, p_t) for the neutral particle and its comparison with the simulated data showed, that clones are in most cases

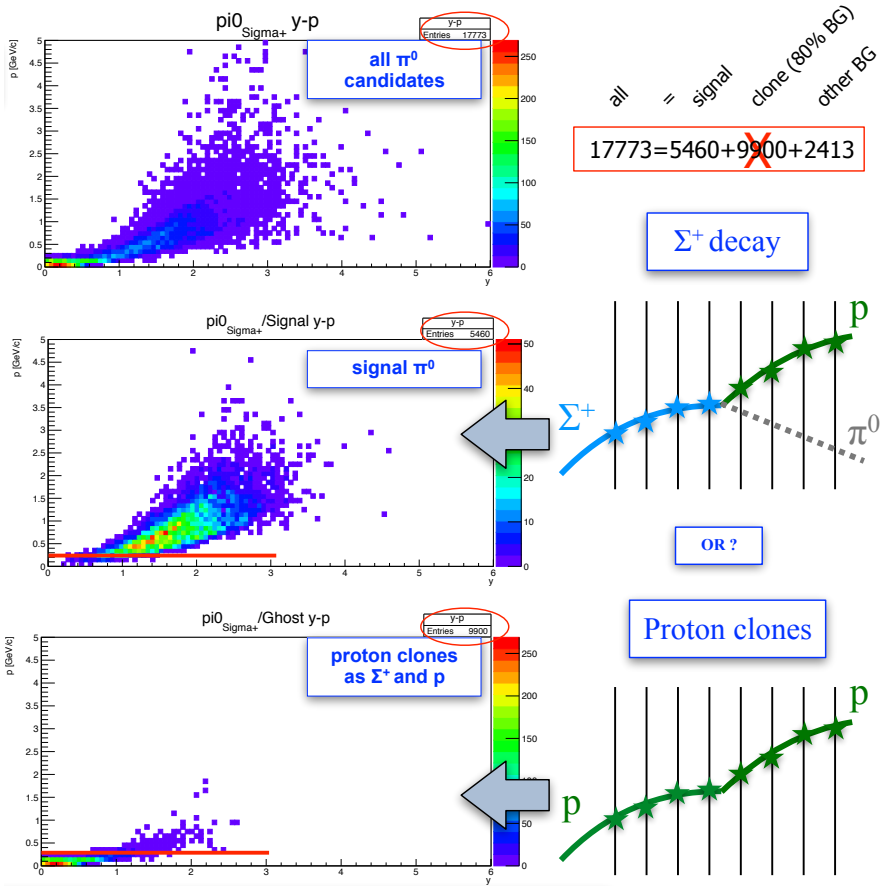

Figure 6.5: The momentum and rapidity distributions for the reconstructed π^0 from the $\Sigma^+ \to p\pi^0$ decay. Applying minimal thresholds allowed suppression of up to 80% of the background from clones [A10].

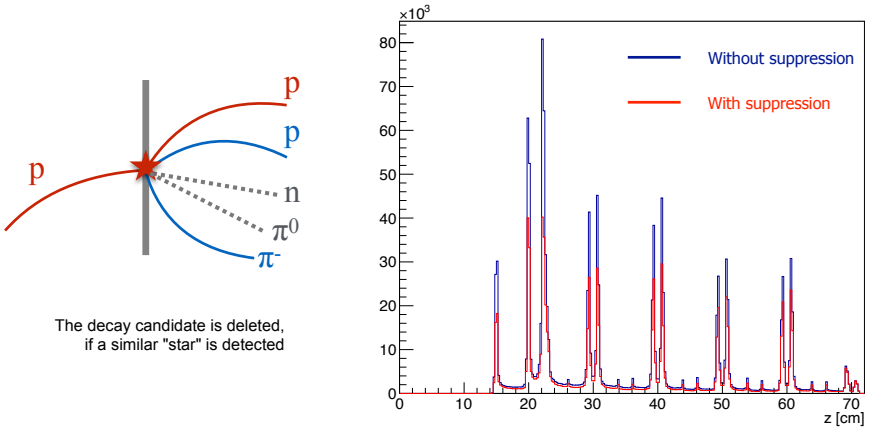

Figure 6.6: On the left is an example of particle knockout from material in an STS detector station. On the right is the background distribution of the π^+ search from the $\Sigma^+ \to n\pi^+$ decay, where the double structure of the STS stations can be seen. For this decay, the background was suppressed by 33% and the signal was reduced by only 1.5%.

short parts of proton trajectories, and almost all of them located in the region of low momenta and rapidities. This makes sense, since two parts of the same track have very close parameters. With this in mind, a minimum momentum and rapidity threshold was applied to the neutral particle, which suppressed 60–80% of the background (Fig. 6.5) [A10].

Another problem that had to be solved in the implementation of the missing mass method was the large amount of background produced from the interaction of particles with material of the stations in the STS detector system. Therefore, a procedure was added to the implementation of the missing mass method to search for so-called "stars" — cases where more than three tracks overlap in the station area (Fig. 6.6, left). When such cases are discarded by the star search procedure, the background is reduced by 20–40% and the efficiency is reduced by only 1–2%, which is quite acceptable (Fig. 6.6, right).

As part of the implementation of the missing mass method, a search for 18 decays with a neutral daughter particle (Fig. 6.7) has been added to the KF Particle Finder package compared to the previous version of the package (Fig. 5.2). This implementation of the missing mass method has been repeatedly and successfully tested within the KF Particle Finder package on simulated data in the CBM experiment, demonstrating the importance of the method for the physics program of the experiment [64].

6.4 Improvement of the method

At the initial stage of the missing mass method development, it was important to demonstrate its applicability in the CBM experiment. This was done first with the example of reconstruction of a neutral daughter particle, which was technically possible to do in a reasonably short time if, in addition to the new algorithms being created, the already existing and proven functionality of the KF Particle package was also used. For this very purpose, the neutral particle mass distributions were constructed as a direct confirmation of the algorithm's performance. Indeed, at this stage, clear mass peaks of neutral particles were immediately visible. The logical continuation was to find the parameters of the mother particles from directly measured parameters of the daughter charged and just calculated neutral particles, in order to be able thus to check at each step the correctness of the current realization of the method.

Since the mass of the neutral particle was calculated with some error, if one applies to it the method of mass constraint [65] and sets the table mass, the inaccuracy of mass determination will pass into inaccuracy of momentum determination. Then the state vector of the neutral particle was added to the initial state vector of the charged daughter particle. Since such an operation of adding

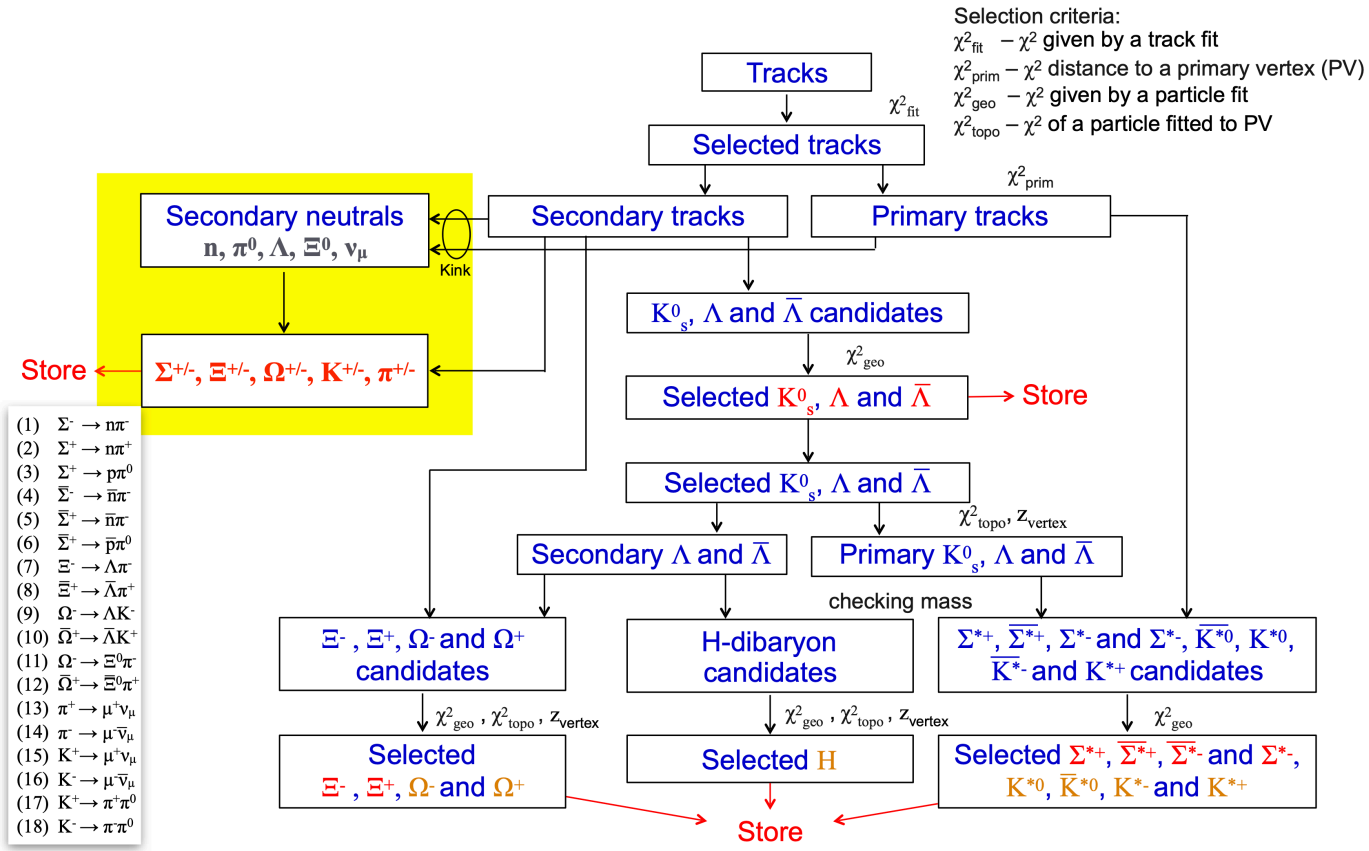

Figure 6.7: A simplified block diagram of the KF Particle Finder package with an additional search for 18 decays with a neutral daughter particle after adding the missing mass method (the corresponding block is highlighted in yellow).

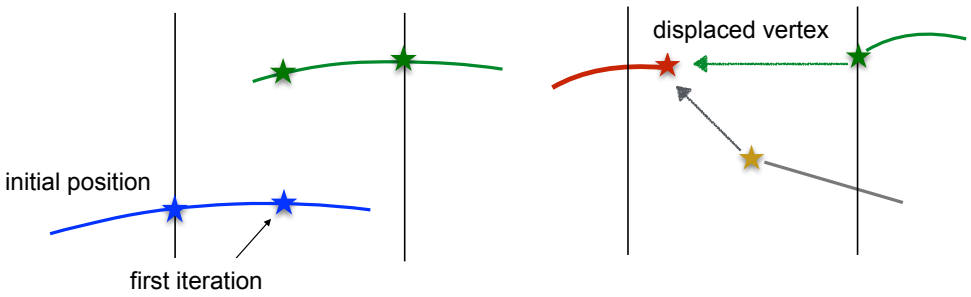

Figure 6.8: Illustration of how the initial version of the missing mass method works. Extrapolation to the point of closest approach of the mother track and the daughter track is done in only one iteration (left). The decay point, already found on the subtraction step, is searched extra time, which turns out to be not optimal (right) [A9, A10].

two daughter particles functionally involved determination of their point of production as well, it turned out that the point of decay of the mother particle was calculated a second time (Fig. 6.8). Thus, in this implementation the mother track was involved once, and the charged daughter track twice, which is not quite correct from a mathematical point of view. Nevertheless, for practical reasons, this approach was chosen for implementation at the initial stage due to the tight time frame for development of the method, as well as the need for step-by-step development of the method with finding parameters of neutral particles, as an important intermediate result for testing the applicability of the method in the CBM experiment.

As a result, already at the initial stage of development of the missing-mass method it showed good results (Fig. 6.9), although it had some drawbacks in implementation, such as the presence of additional calculations and not quite mathematically correct determination of the decay vertex of short-lived particles.

After the successful validation of the applicability of the missing mass method in the CBM experiment and its intensive and comprehensive investigation, numerous improvements have been made to its initial implementation.

First of all, in the improved implementation of the method, the position of the decay point of the charged mother particle is determined immediately by two-step extrapolation and an updated particle subtraction procedure and does not require further correction and recalculation, which is mathematically accurate (Fig. 6.10). The mathematical part of the method implementation has also been significantly improved using a more accurate and faster approach. In particular, all basic calculations are now performed with 6×6 matrices instead of the former 7×7 matrices due to the fact, that the particle energy parameter has been removed from the state vector and from the covariance matrix.

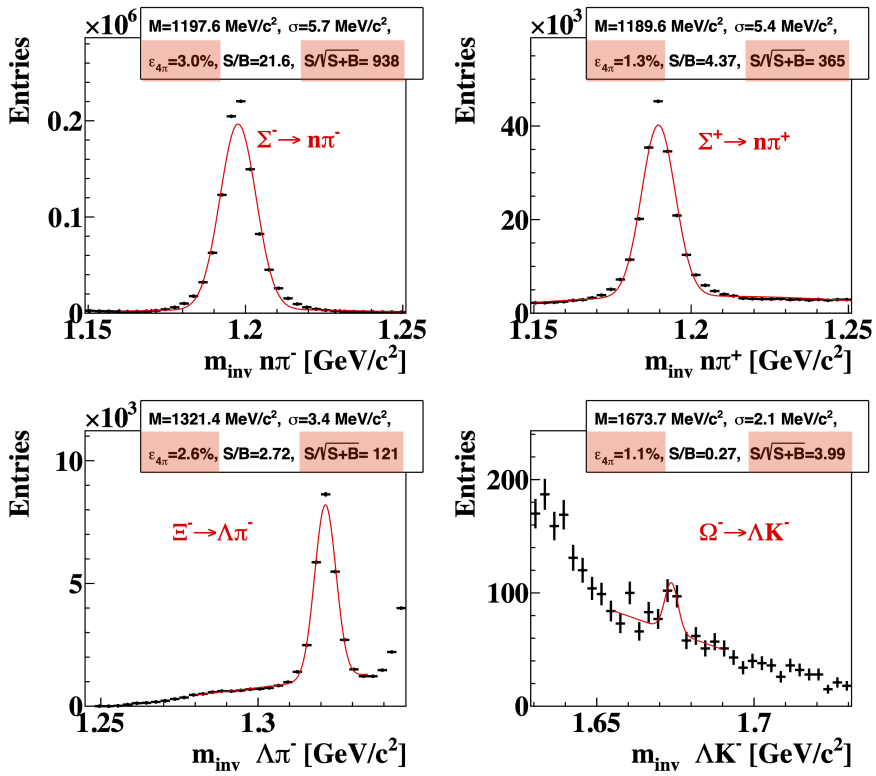

Figure 6.9: Mass distributions of strange particles reconstructed by the initial version of the missing mass method for 5 M simulated central Au+Au collisions in the UrQMD model at 10 GeV/n energy in the CBM experiment [A9, A10].

The energy and mass calculations are now performed separately in the last step, and the parameters of all short-lived particles are estimated in one iteration of the Kalman filter subtraction instead of the previous two, subtraction and then addition, as was done in the initial version. This also eliminated the need to use a very resource-intensive mass constraint method that balanced the particle parameters at a certain stage of the computation, which also introduced additional inaccuracies and significantly slowed down the computation process.

As an illustration, let us look at some formulas for the improved version of the missing mass method, using the example of $\Sigma^- \to n\pi^-$ decay.

The subtraction operation is performed with the Σ^- and π^- particle state vectors with parameters at the points of closest approach on the particle trajectories. These points are searched in advance as a result of extrapolation of the original particle trajectories using the Kalman filter method.

The Kalman filter method [66] is intended to find the optimal estimate $\mathbf{r}$ of the unknown state vector $\mathbf{r}^t$ from the measurement results $\mathbf{m}_k$, $k = 1 \ldots n$ of vector $\mathbf{r}^t$.

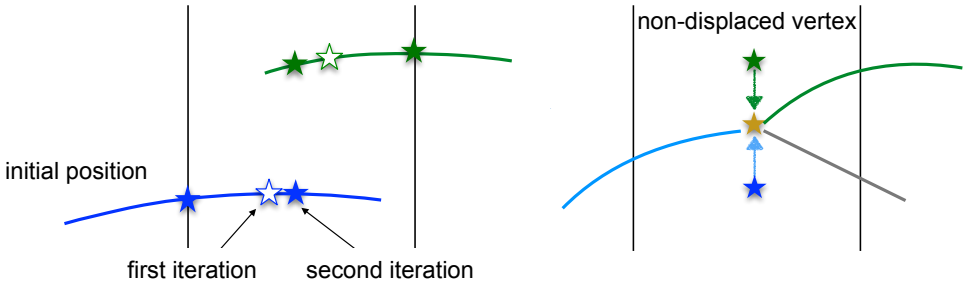

Figure 6.10: Illustration of how the improved version of the method works. Extrapolation to the point of closest approach of tracks is done in two steps (on the left). The decay point and the parameters of all its particles are determined in one loop of the algorithm, which is faster and more accurate (right)) [A9, A10].

The Kalman filter algorithm starts with some initial approximation $\mathbf{r} = \mathbf{r}_0$ and refines the vector $\mathbf{r}$ by progressively adding one measurement after another. The optimal estimate of $\mathbf{r}$ is determined after adding the last measurement.

In general, the unknown vector $\mathbf{r}^t$ may change from one measurement to another:

$$\mathbf{r}_k^t = A_k \mathbf{r}_{k-1}^t + \boldsymbol{\nu}_k \,, \tag{6.10}$$

where A_k is the linear extrapolation operator, and $\boldsymbol{\nu}_k$ is the process noise between the $(k-1)$-th and k-th measurements.

The measurement $\mathbf{m}_k$ is linearly dependent on $\mathbf{r}_k^t$:

$$\mathbf{m}_k = H_k \mathbf{r}_k^t + \boldsymbol{\eta}_k \,, \tag{6.11}$$

where $\boldsymbol{\eta}_k$ is the error of the k-th measurement. The measurement errors $\boldsymbol{\eta}_i$ and process noise $\boldsymbol{\nu}_j$ are assumed to be uncorrelated and unbiased ($< \boldsymbol{\eta}_i > = < \boldsymbol{\nu}_j > = \mathbf{0}$) and the covariance matrices V_k, Q_k are known:

$$\begin{array}{rcl} < \boldsymbol{\eta}_i \cdot \boldsymbol{\eta}_i^T > & \equiv & V_i \,, \\ < \boldsymbol{\nu}_j \cdot \boldsymbol{\nu}_j^T > & \equiv & Q_j \,. \end{array} \tag{6.12}$$

The fitting algorithm consists of several steps:

1. Initialization. An approximate value of the vector $\mathbf{r}_0$ is chosen. Its covariance matrix has the form $C_0 = \mathrm{I} \cdot \mathrm{inf}^2$, where inf denotes a large positive number.

2. Extrapolation. If the initial vector $\mathbf{r}^t$ is known to change between the $(k-1)$-th and k-th measurements (6.10), then when moving to the k-th

measurement its current estimate $\mathbf{r}_{k-1}$ is also transformed in a similar way:

$$\begin{aligned} \widetilde{\mathbf{r}}_k &= A_k \mathbf{r}_{k-1} \,, \\ \widetilde{C}_k &= A_k C_{k-1} A_k^T + Q_k \,, \end{aligned} \tag{6.13}$$

where $\widetilde{\mathbf{r}}_k$ is the optimal estimate of the vector $\mathbf{r}_k^t$ from the first $k-1$ measurements. In contrast to the extrapolation operator A_k, which describes deterministic changes of the vector $\mathbf{r}^t$ in time, the process noise Q_k describes probabilistic deviations of the vector $\mathbf{r}^t$.

3. Filtering. For each measurement $\mathbf{m}_k$ a vector $\mathbf{r}_k$ is calculated, which is the optimal estimate of the vector $\mathbf{r}_k^t$ from the first k measurements.

$$\begin{aligned} K_k &= \widetilde{C}_k H_k^T (V_k + H_k \widetilde{C}_k H_k^T)^{-1} \,, \\ \mathbf{r}_k &= \widetilde{\mathbf{r}}_k + K_k (\mathbf{m}_k - H_k \widetilde{\mathbf{r}}_k) \,, \\ C_k &= \widetilde{C}_k - K_k H_k \widetilde{C}_k \,, \\ \chi^2_k &= \chi^2_{k-1} + (\mathbf{m}_k - H_k \widetilde{\mathbf{r}}_k)^T (V_k + H_k \widetilde{C}_k H_k^T)^{-1} (\mathbf{m}_k - H_k \widetilde{\mathbf{r}}_k) \,. \end{aligned} \tag{6.14}$$

Here $\widetilde{\mathbf{r}}_k$, $\widetilde{C}_k$ — the optimal estimate of the state vector and its covariance matrix obtained in the previous step and extrapolated to the k-th measurement; $\mathbf{m}_k$, V_k — k-th measurement and its covariance matrix; $\boldsymbol{\zeta}_k$ — residual parameter; matrix H_k — measurement model; matrix K_k — so-called gain matrix; the value χ^2_k — the total χ^2-deviation of the resulting estimate $\mathbf{r}_k$ from the measurements $\mathbf{m}_1, \ldots \mathbf{m}_k$.

The vector $\mathbf{r}_n$ obtained after filtering the last measurement is the required optimal estimate with the covariance matrix C_n.

When the measurement $\mathbf{m}_k$ nonlinearly depends on $\mathbf{r}_k^t$, it is necessary to linearize the measurement model. As a linearization point, some vector $\mathbf{r}_k^0$ is taken:

$$\mathbf{m}_k(\mathbf{r}_k^t) = \mathbf{h}_k(\mathbf{r}_k^t) + \boldsymbol{\eta}_k \approx \mathbf{h}_k(\mathbf{r}_k^0) + H_k(\mathbf{r}_k^t - \mathbf{r}_k^0) + \boldsymbol{\eta}_k \,, \tag{6.15}$$

where H_k is the Jacobian $\mathbf{h}_k(\mathbf{r}_k)$ in $\mathbf{r}_k^0$:

$$H_{k\,(ij)} = \left. \frac{\partial \mathbf{h}_k(\mathbf{r}_k)_{\,(i)}}{\partial \mathbf{r}_{k\ (j)}} \right|_{\mathbf{r}_k = \mathbf{r}_k^0} . \tag{6.16}$$

A Kalman filter with a nonlinear measurement model is called an extended Kalman filter. The filtering equations for the extended Kalman filter are the same as in the linear case (6.14), except for the residual parameter $\boldsymbol{\zeta}_k$, which is calculated by the formula:

$$\boldsymbol{\zeta}_k = \mathbf{m}_k - \left(\mathbf{h}_k \left(\mathbf{r}_k^0 \right) + H_k \left(\widetilde{\mathbf{r}}_k - \mathbf{r}_k^0 \right) \right) . \tag{6.17}$$

The result of nonlinear fitting depends on the linearization point $\mathbf{r}_k^0$. Taking the current value of $\widetilde{\mathbf{r}}_k$ as the linearization point for the k-th measurement, the extended Kalman filter is the same as the standard one. But to get more reliable and accurate results, the fitting procedure must be repeated several times, using the optimal estimate of $\mathbf{r}_n$ as the linearization point for all measurements in the next iteration.

In our problem of searching for short-lived particles, the particle state vectors have the following form:

$$\mathbf{r} \;\equiv\; (x,\, y,\, z,\, p_x,\, p_y,\, p_z)^T \;. \tag{6.18}$$

For a better understanding of further formulas, we present their corresponding error matrices C in block form, where the index v denotes the elements associated with the coordinate, and the index p — with the momentum:

$$C \;\equiv\; \begin{pmatrix} C^v & C^{vp\,T} \\ C^{vp} & C^p \end{pmatrix} . \tag{6.19}$$

We also denote by S the following expression for convenience:

$$S \;\equiv\; \left(C^v_{\Sigma^-} + C^v_{\pi^-}\right)^{-1} . \tag{6.20}$$

In this approach, the decay point common to the charged mother Σ^- and daughter π^- particles is determined, taking into account the accuracy of their parameters, and will not be recalculated later. At the same time, all their track vector parameters and corresponding errors are refined:

$$\begin{aligned}
K_{\Sigma^-} &= \begin{pmatrix} C^v_{\Sigma^-} \\ C^{vp}_{\Sigma^-} \end{pmatrix} S\,, \qquad K_{\pi^-} \;=\; \begin{pmatrix} C^v_{\pi^-} \\ C^{vp}_{\pi^-} \end{pmatrix} S\,, \\
\boldsymbol{\zeta} &= \mathbf{v}_{\pi^-} - \mathbf{v}_{\Sigma^-}\,, \\
\mathbf{r}^{\,filtered}_{\Sigma^-} &= \mathbf{r}_{\Sigma^-} + K_{\Sigma^-}\boldsymbol{\zeta} \;=\; \begin{pmatrix} \mathbf{v}_{\Sigma^-} + C^v_{\Sigma^-} S\boldsymbol{\zeta} \\ \mathbf{p}_{\Sigma^-} + C^{vp}_{\Sigma^-} S\boldsymbol{\zeta} \end{pmatrix}, \\
\mathbf{r}^{\,filtered}_{\pi^-} &= \mathbf{r}_{\pi^-} - K_{\pi^-}\boldsymbol{\zeta} \;=\; \begin{pmatrix} \mathbf{v}_{\pi^-} - C^v_{\pi^-} S\boldsymbol{\zeta} \\ \mathbf{p}_{\pi^-} - C^{vp}_{\pi^-} S\boldsymbol{\zeta} \end{pmatrix}, \\
C^{\,filtered}_{\Sigma^-} &= C_{\Sigma^-} - K_{\Sigma^-}\left(C^v_{\Sigma^-},\, C^{vp\,T}_{\Sigma^-}\right) \;=\; \begin{pmatrix} C^v_{\Sigma^-} - C^v_{\Sigma^-} S C^v_{\Sigma^-} & C^{vp\,T}_{\Sigma^-} - C^v_{\Sigma^-} S C^{vp\,T}_{\Sigma^-} \\ C^{vp}_{\Sigma^-} - C^{vp}_{\Sigma^-} S C^v_{\Sigma^-} & C^p_{\Sigma^-} - C^{vp}_{\Sigma^-} S C^{vp\,T}_{\Sigma^-} \end{pmatrix}, \\
C^{\,filtered}_{\pi^-} &= C_{\pi^-} - K_{\pi^-}\left(C^v_{\pi^-},\, C^{vp\,T}_{\pi^-}\right) \;=\; \begin{pmatrix} C^v_{\pi^-} - C^v_{\pi^-} S C^v_{\pi^-} & C^{vp\,T}_{\pi^-} - C^v_{\pi^-} S C^{vp\,T}_{\pi^-} \\ C^{vp}_{\pi^-} - C^{vp}_{\pi^-} S C^v_{\pi^-} & C^p_{\pi^-} - C^{vp}_{\pi^-} S C^{vp\,T}_{\pi^-} \end{pmatrix}, \\
D^f &= K_{\pi^-}\left(C^v_{\Sigma^-},\, C^{vp\,T}_{\Sigma^-}\right) \;=\; \begin{pmatrix} C^v_{\pi^-} S C^v_{\Sigma^-} & C^v_{\pi^-} S C^{vp\,T}_{\Sigma^-} \\ C^{vp}_{\pi^-} S C^v_{\Sigma^-} & C^{vp}_{\pi^-} S C^{vp\,T}_{\Sigma^-} \end{pmatrix}, \\
\chi^2 &= \boldsymbol{\zeta}^T S \boldsymbol{\zeta}\,.
\end{aligned} \tag{6.21}$$

Here K — the gain matrix, $\boldsymbol{\zeta}$ — the difference of coordinate vectors, D — the auxiliary matrix for calculating the covariance matrix of the neutral particle, and χ^2 — the parameter by which one can judge the probability that the tracks belong to the same decay.

The next part of the formulas refers to the calculation of the parameters of the neutron. since the decay coordinate is common to all particles and it has already been found. So it only remains to calculate the part of the state vector $\mathbf{r}_n$ relating to the momentum using the matrix A and correctly account for errors:

$$\begin{aligned} \mathbf{r}_n &= \mathbf{r}_{\Sigma^-}^{filtered} - A\mathbf{r}_{\pi^-}^{filtered}, \\ C_n &= C_{\Sigma^-}^{filtered} - AD^f - D^{f\,T}A^T + AC_{\pi^-}^{filtered}A^T, \end{aligned} \tag{6.22}$$

$$A = \begin{pmatrix} \mathrm{O} & \mathrm{O} \\ \mathrm{O} & \mathrm{I} \end{pmatrix}. \tag{6.23}$$

By making the necessary substitutions in (6.22), one can obtain expressions for the neutron state vector and its error matrix:

$$\begin{aligned} \mathbf{r}_n &= \begin{pmatrix} \mathbf{v}_{\Sigma^-} + C^v_{\Sigma^-}S\boldsymbol{\zeta} \\ \mathbf{p}_{\Sigma^-} - \mathbf{p}_{\pi^-} + \left(C^{vp}_{\Sigma^-} + C^{vp}_{\pi^-}\right)S\boldsymbol{\zeta} \end{pmatrix}, \\ C_n &= \begin{pmatrix} C^v_{\Sigma^-} - C^v_{\Sigma^-}SC^v_{\Sigma^-} & C^{vp\,T}_{\Sigma^-} - C^v_{\Sigma^-}S\left(C^{vp}_{\Sigma^-} + C^{vp}_{\pi^-}\right)^T \\ C^{vp}_{\Sigma^-} - \left(C^{vp}_{\Sigma^-} + C^{vp}_{\pi^-}\right)SC^v_{\Sigma^-} & C^p_{\Sigma^-} + C^p_{\pi^-} - \left(C^{vp}_{\Sigma^-} + C^{vp}_{\pi^-}\right)S\left(C^{vp}_{\Sigma^-} + C^{vp}_{\pi^-}\right)^T \end{pmatrix}. \end{aligned} \tag{6.24}$$

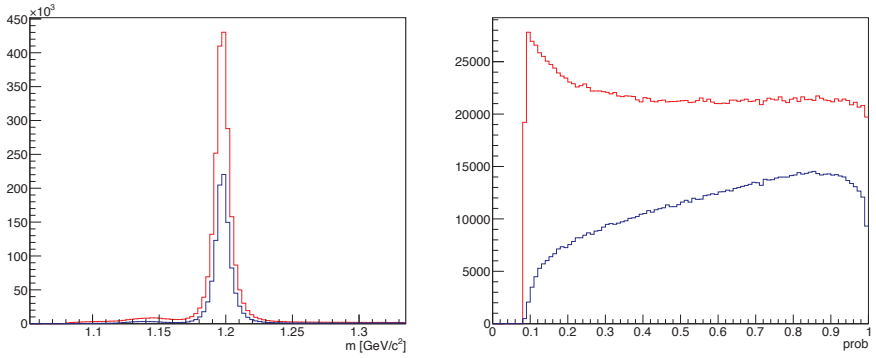

Figure 6.11: The Σ^- mass distribution (left) and the χ^2 *prob* function distribution (right) for the $\Sigma^- \to n\pi^-$ decay. The blue color shows the results of the initial and the red one — the improved implementation of the missing mass method [A14].

This mathematically more accurate implementation of the missing mass method significantly improved the quality of the reconstruction of short-lived particles, resulting in a 2-fold increase in the reconstruction efficiency of $\Sigma^- \to n\pi^-$ decays

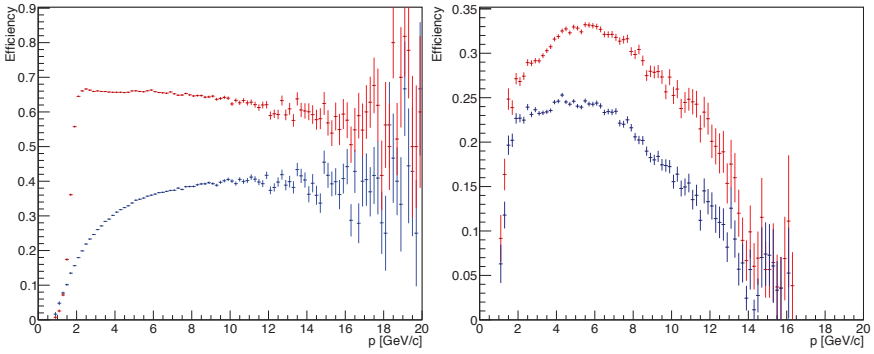

Figure 6.12: Comparison of decay reconstruction efficiencies $\Sigma^- \to n\pi^-$ (left) and $\Sigma^+ \to p\pi^0$ (right) for the initial (blue) and improved versions (red) of the missing mass method [A14].

and improved *prob* distribution, which became flatter, corresponding to a more correct behavior of χ^2 distribution (Fig. 6.11).

Fig. 6.12 compares the reconstruction efficiencies of $\Sigma^- \to n\pi^-$ (left) and $\Sigma^+ \to p\pi^0$ (right) decays for the initial and improved versions of the missing mass method. For these decays, the significance was increased by 40% and 10%, respectively, using 5 M central UrQMD events at 10 GeV/n energy with particle identification in the TOF detector [A14].

Table 6.2: Comparison of 4π efficiencies in the initial and improved versions

Version	$\Sigma^- \to n\pi^-$	$\Sigma^+ \to n\pi^+$	$\Xi^- \to \Lambda\pi^-$	$\Omega^+ \to \Lambda K^-$
Initial	3.0%	1.3%	2.6%	1.1%
Improved	6.1%	2.8%	6.5%	1.4%
Factor	2.03	2.15	2.50	1.27

The results of the improved implementation of the missing mass method for 5 M simulated central Au+Au collisions in the UrQMD model at 10 GeV/n energy in the CBM experiment using TOF detector data are shown in Fig. 6.13 (compare with Fig. 6.9) and Tab. 6.2. The mathematically more accurate implementation of the missing mass method resulted in a 2-fold increase in their reconstruction efficiency and a 25–30% increase in the significance of the signal data.

Thus, the missing mass method is implemented as an extension of the KF Particle Finder package (Fig. 6.14, compared to Fig. 5.3), which is currently actively used to search and reconstruct short-lived particles both online and offline in large heavy ion experiments such as CBM (FAIR/GSI), ALICE (CERN) and STAR (BNL).

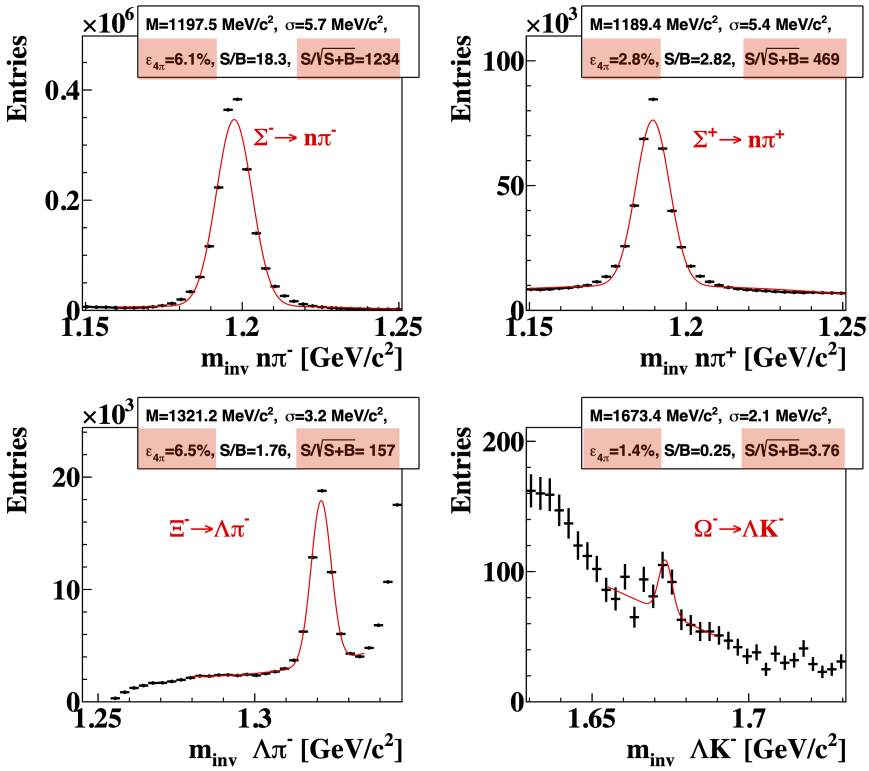

Figure 6.13: Mass distributions of strange particles reconstructed using the improved implementation of the missing mass method for 5 M simulated central Au+Au collisions using the UrQMD model at 10 GeV/n energy in the CBM experiment [A9, A10].

Like all other algorithms in the KF Particle and KF Particle Finder packages, the missing mass method is implemented with extensive use of vector (SIMD) instructions and is optimized for parallel operation on modern many-core high performance computing facilities, which can include both processors and coprocessors. The set of algorithms implementing the method was tested on computers with dozens of cores and showed high speed and almost linear scalability with respect to the number of cores involved.

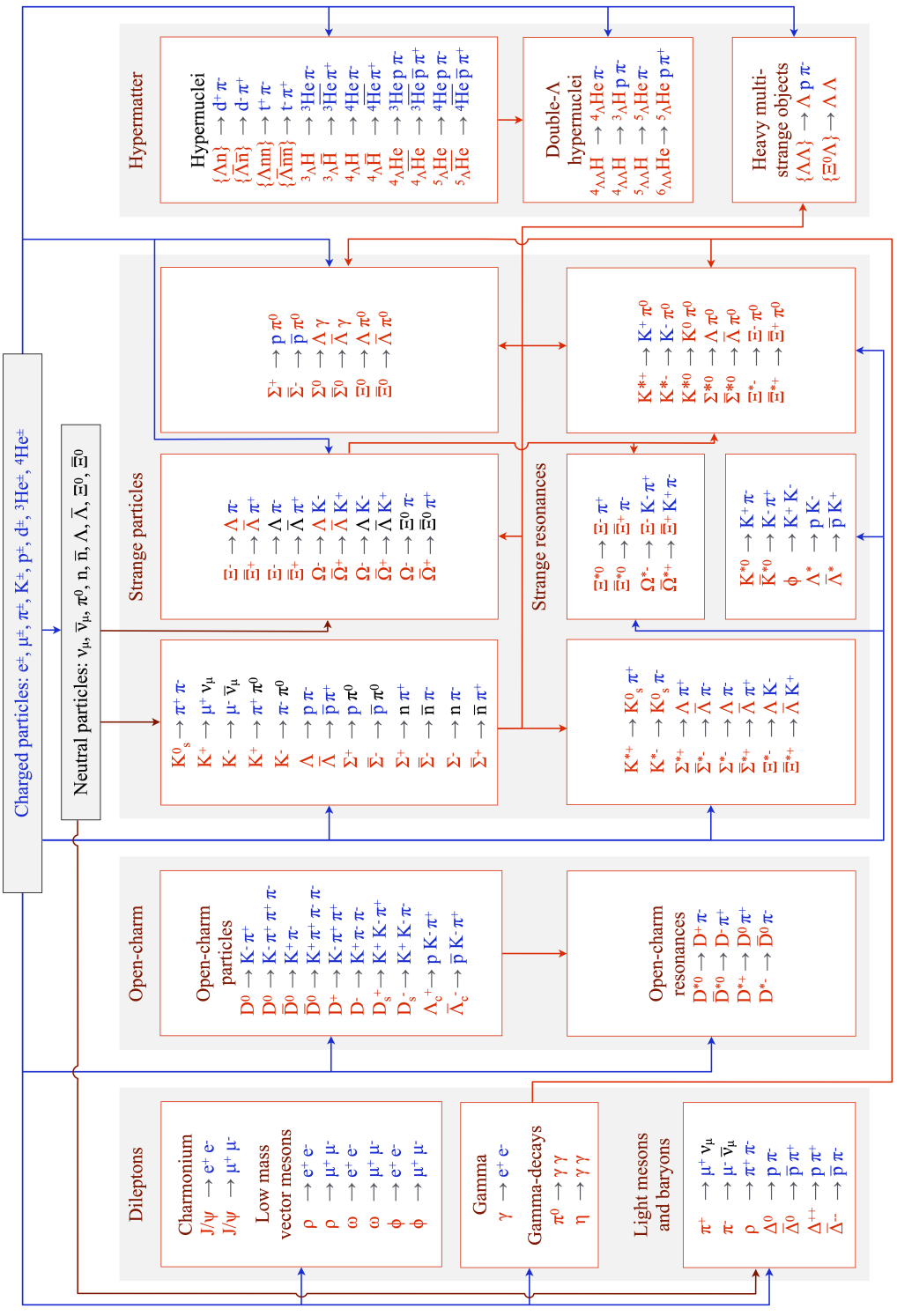

Figure 6.14: A block diagram of the KF Particle Finder package with an implemented missing mass method for finding decays of short-lived particles with a neutral particle in the daughter channel (highlighted in black).

Chapter 7

Approbation in the STAR experiment

It is important, especially for the first stage of the CBM experiment, to demonstrate on real data the proof of concept of the developed approach, reliability and efficiency of its current implementation. Such an opportunity is given by the FAIR Phase-0 program, providing members of the CBM Collaboration to participate in the STAR experiment at BNL (USA).

7.1 The STAR experiment

At the acceleration facility RHIC (Relativistic Heavy Ion Collider, Fig. 7.1) it is possible to study the collisions of relativistic ions of various nuclei, as well as protons. The Electron Beam Ion Source (EBIS) serves as a source of heavy ions and protons, which replaced the Van de Graaff accelerator in 2012. Both ions and protons are accelerated by the booster to 37% of the speed of light and then injected into the AGS synchrotron, where the ions are accelerated to 99.7% of the speed of light. The ion beam is then directed into a 2.4 mile (3.8 km) long RHIC ring, switched by a magnetic field between rings with opposite beam directions. Two oppositely directed beams can collide in six interaction regions, four of which are intended for experimental studies at the STAR, PHENIX, PHOBOS, and BRAMS detectors. Three detectors have now completed their physics programs and only the STAR detector continues to be active on acquiring experimental data.

Since 2000, the RHIC facility has accelerated and collided the following systems at various energies: p+p, Cu+Cu, p+Au, d+Au, Cu+Au, Au+Au, U+U. The maximum RHIC accelerator energy for heavy ions is $\sqrt{s_{NN}} = 200$ GeV per nucleon-nucleon pair and $\sqrt{s_{pp}} = 500$ GeV for proton-proton collisions. Since

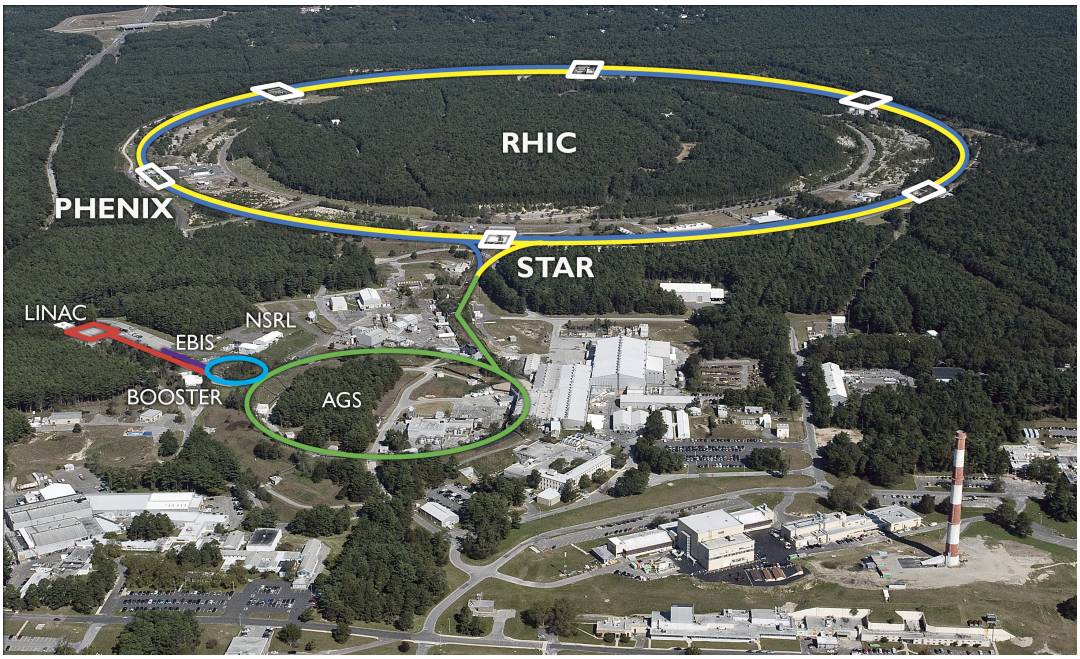

Figure 7.1: View of the RHIC acceleration facility [101].

the total energy of the ion in the beam is $E_{\text{acc}} \cdot Z/A$, where Z is the number of protons in the nucleus and A is the mass number, protons and light nuclei can be accelerated to higher energies per nucleon because their Z/A ratio is larger compared to heavier nuclei.

The STAR experiment is designed to study nuclear matter under extreme conditions of relativistic heavy ion collisions, including hadron production, search for signatures of quark-gluon plasma formation, and study its properties.

Most of the detectors in the STAR experimental setup (Fig. 7.2, left) are located inside a large solenoidal magnet with an approximately uniform magnetic field (B = 0.5 Tl at maximum) directed parallel to the beam axis. The main tracking detector is a large volume Time Projection Chamber (TPC) with an inner radius of 0.5 m, outer radius of 2 m, and length of 4.2 m. The TPC covers the pseudo-rapidity range $|\eta| < 1.8$ and is designed to reconstruct very high multiplicity events with up to 1000 charged particles per rapidity unit produced by heavy ion collisions. The detector is also used for particle identification by measuring the particle energy loss dE/dx in the gas volume of the detector. Other particle identification detectors include the Barrel Electromagnetic Calorimeter (BEMC), the Time-Of-Flight (TOF) detector, and the Muon Tracking Detector (MTD). The Heavy Flavor Tracker (HFT) detector was installed around the interaction region and was used in 2014–2016 for more accurate measurements of mesons and baryons with heavy quarks.

With full azimuthal coverage and good pseudo-rapidity $|\eta| < 1.8$ coverage, the

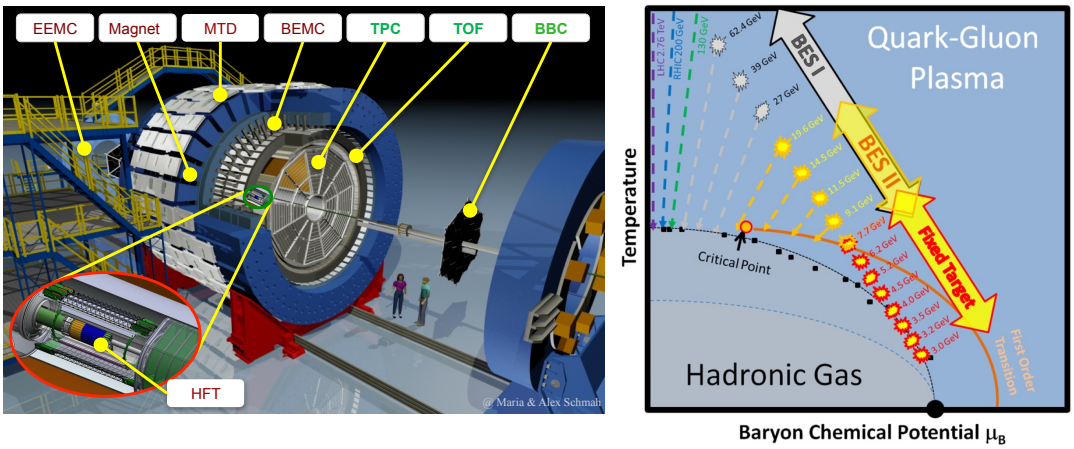

Figure 7.2: Left: The STAR [83] detector setup with its main detectors: Endcap Electromagnetic Calorimeter (EEMC), Magnet, Muon Tracking Detector (MTD), Barrel Electromagnetic Calorimeter (BEMC), Time Projection Chamber (TPC), Time-Of-Flight detector (TOF), Beam-Beam Counter (BBC) and Heavy Flavor Tracker (HFT). Right: Phase diagram of the QCD for the beam energy scan program (BES) [86].

STAR detector is capable of investigating a wide range of physics phenomena.

A very important feature of the RHIC acceleration facility is the ability to study the entire range of the μ_B baryonic chemical potential from 20 to 420 MeV within the Beam Energy Scan (BES) program of the STAR experiment (Fig. 7.2, right). The BES-I studies from 2010–2014 further confirmed the evidence for the discovery of the QGP at the highest RHIC energy $\sqrt{s_{NN}} = 200$ GeV. The range of energies investigated included Au+Au collisions from 200 to 7.7 GeV, which covers the critical point region, the end of the first-order phase transition between the hadronic gas and the QGP. The results of the search for the critical point and the first-order phase transition boundary have narrowed the region of interest to collision energies below $\sqrt{s_{NN}} = 20$ GeV. The second phase of the beam energy scan BES-II was done in 2019–2021 [85] and covers the $\sqrt{s_{NN}} < 20$ GeV range of energies. Current lattice QCD calculations assume that key features of the phase diagram, such as the critical point and first-order phase transition, are within the reach of the BES-II program.

Let us focus in more detail on the main elements of the STAR detector system.

7.1.1 Solenoid magnet

For many years now, magnets have been integral and often the most expensive parts of detection systems in high energy physics experiments.

A strong magnetic field is needed to bend the trajectories of charged particles produced by collisions and flying through tracking detectors. Measuring the

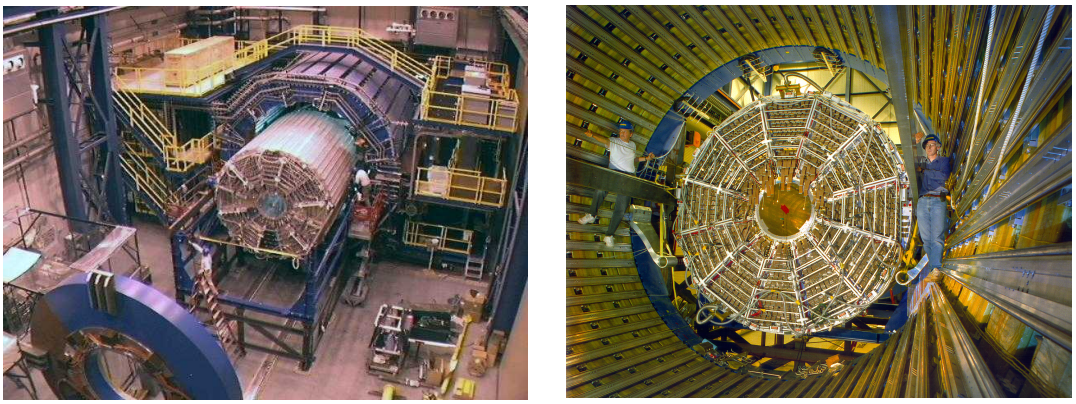

Figure 7.3: The process of installing the TPC detector inside the solenoid magnet [101]

curvature of particle trajectories makes it possible to determine their momentum, and additional knowledge of their velocity also makes it possible to determine their mass. Particles of different charge sign are deflected in the magnetic field in opposite directions, while the trajectories of neutral particles are not affected by the magnetic field. The strength of this effect, which was studied by the Dutch physicist Hendrik Lorentz, depends on the magnitude of the magnetic field as well as the charge and velocity of the particle. Let's write down the expression he derived in 1892:

$$\mathbf{F_L} = q \cdot (\mathbf{E} + [\mathbf{v} \times \mathbf{B}]). \tag{7.1}$$

The electric field $\mathbf{E}$ is the driving force for the drift toward the sides of the TPC detector of electrons generated by the ionization of gas atoms, but its effect on relativistic particles can be neglected. However, the magnetic field, whose magnitude varies in the range $0.25 < \mathrm{B} < 0.5$ Tl [102], significantly bends their trajectories. The magnitude of the field is chosen so as to have sufficient influence on high energy particles and, at the same time, to allow particles with relatively low momentum to exit the TPC and reach the TOF. In order to determine the momentum of a particle it is necessary to determine the radius of curvature of its trajectory r in the TPC detector. Recalling the expression for centripetal acceleration and Newton's second law, we obtain

$$\mathbf{a} = \frac{v^2}{r}\mathbf{e_n} = \frac{\mathbf{F_L}}{m} = \frac{q[\mathbf{v} \times \mathbf{B}]}{m}. \tag{7.2}$$

From here, through simple transformations, we can derive a scalar expression for the transverse momentum p_T:

$$p_T = rqB. \tag{7.3}$$

To determine the mass, knowing the momentum, the Time-Of-Flight detector will help. By calculating the transverse projection of the path length S_T from the point of creation to the detector TOF and the time of flight t, we find the mass of the particle:

$$m = \frac{p_T}{v_T} = \frac{rqBt}{S_T}. \tag{7.4}$$

The geometry of the detection system is usually chosen so that the direction of the magnetic induction vector is perpendicular to most of the flying particles. In contrast to the CBM dipole magnet discussed earlier, the STAR experiment uses a solenoid type magnet. The cylindrically symmetric field is excellent with the TPC barrel tracking detector and the TOF detector wall located directly inside the circular coils of the magnet (Fig. 7.2 left, Fig. 7.3). The field created in this way is almost homogeneous inside the TPC volume and is directed along the Z axis. It does not act on colliding beams, and does not prevent clusters of secondary electrons from ionizing gas atoms from drifting toward the ends of the TPC. A great advantage of the TPC detector is the absence of material in the path of the particles, which significantly reduces their multiple scattering and knocking out of secondary particles by them.

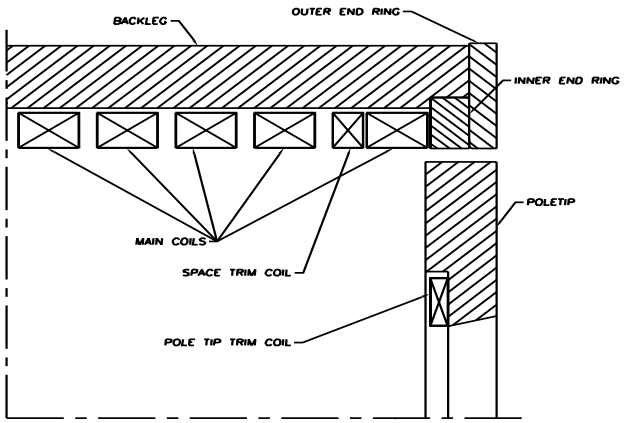

Figure 7.4: Schematic representation of the main elements of the STAR magnet (longitudinal view) [102].

The STAR magnetic system is based on the following elements: ten main coils, four adjustment coils, thirty steel rods, four steel end rings, and two pole tips. The layout of these elements is shown in Fig. 7.4. Two adjustment coils (space trim) are on the side surface next to the main coils, the other two are on the ends next to the poles (pole tip trim). The supporting structure is the steel rods (30 pieces, 6.85 m long, 18 t each), which are parallel to the axis of the magnet over the coils, and the end rings: two inner rings (diameter 5.27–6.28 m, 25 t each) and two outer rings (outer diameter 7.32 m, 35 t each). The entire structure weighs 1100 t and is mounted by the bottom nine rods on special hangers [102].

7.1.2 The Time Projection Chamber (TPC)

An important event in particle physics was the invention in 1968 by Georges Charpak of the Multi-Wire Proportional Chamber (MWPC), which replaced the spark chamber. The new type of detector made it possible to increase the number of detected particles from several to thousands per second. It brought many other advantages, including a contribution to particle identification by measuring ionization losses dE/dx [88]. Georges Charpak was awarded the Nobel Prize in 1992 for this invention.

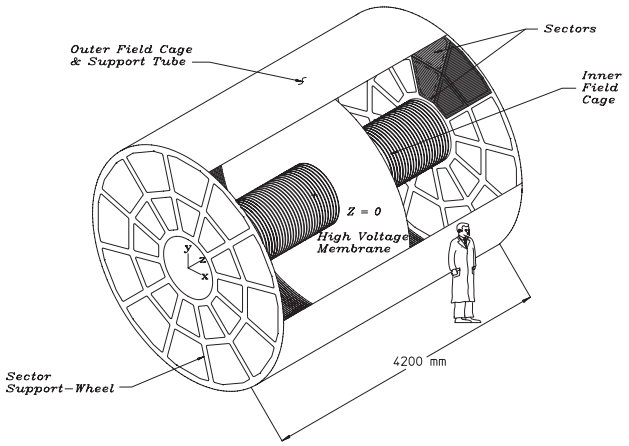

Figure 7.5: Schematic representation of the main elements of the TPC detector [89].

The next important invention occurred in 1974 when David Nygren developed the Time Projection Chamber. It combined the principles of the proportional and drift chambers. Its main feature is a large volume of gas with a constant electric field. Drifting electrons, knocked out as a result of ionization of gas atoms by a charged particle, form small clusters and under the influence of the field reach the side panel, similar to one layer of the multi-wire chamber, form there a projection — information about two track coordinates in the plane perpendicular to the field direction. Their drift time, on the other hand, makes it possible to determine the third coordinate. Thus, it became possible to register three-dimensional data about the trajectories of particles that have passed through the chamber [88].

The TPC (Time Projection Chamber) is the main tracking detector of the STAR setup and is designed for tracking and identifying charged particles. A schematic representation of the TPC is shown in Figure 7.5. The sensitive volume of the chamber is located between inner and outer cylindrical systems of gradient rings (Inner and Outer Field Cages). Their radius is 50 cm and 200 cm, respectively, and the length along the beam axis Z is 420 cm. The geometry covers the acceptance range of the full azimuthal angle and pseudo-rapidity $|\eta| < 1.8$. The chamber is filled with an inert purified gas (90% argon, 10% methane), the presence of impurities would cause the drifting electrons to slow down. The pressure inside the detector's working volume is 2 bar higher than atmospheric [89]. This

small difference in pressure is due to the need to avoid foreign gases entering the chamber from the outside, but also to prevent the chamber from breaking.

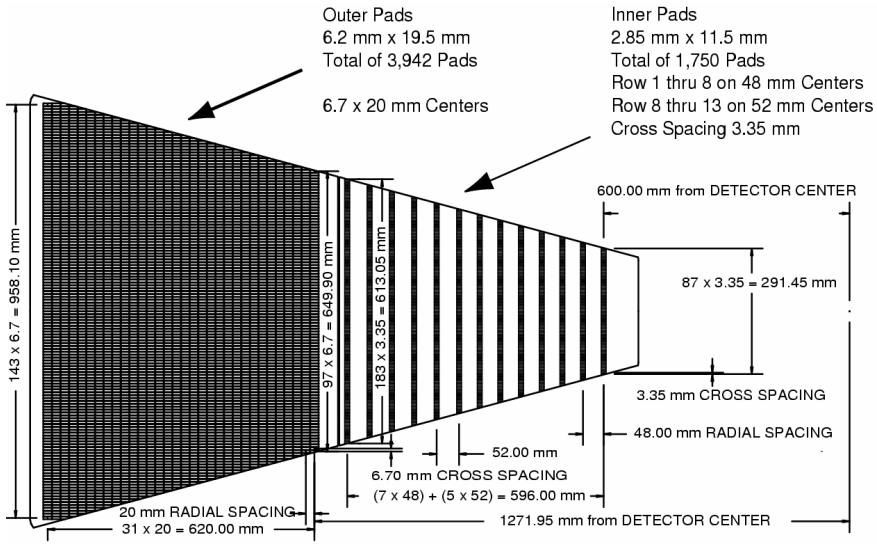

Figure 7.6: A sector of the readout panel. The inner and outer parts have different architecture [89].

The detector is divided in two equal parts by a flat cathode membrane under high voltage of 28 kV. Parallel to this, grounded panels with readout electronics are mounted on aluminum wheel-shaped supports on both end sides. An electric field is generated between the central membrane and the side plugs. A system of equipotential rings is installed on the inner and outer walls of the cylindrical cells. They provide a uniform field gradient along the Z axis, contributing to its homogeneity. The central ring is connected to the cathode membrane and the outer rings are connected to the anode panels [89].

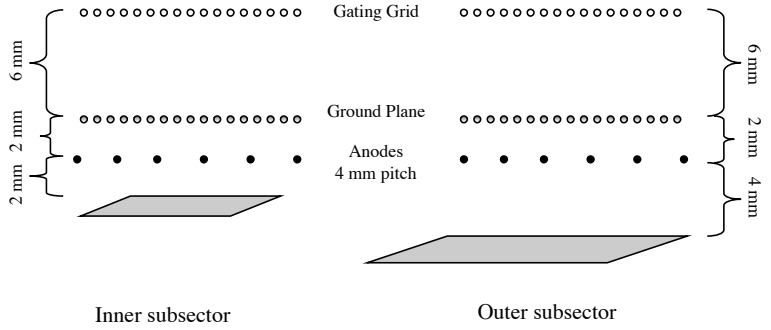

Figure 7.7: Simplified structure of the multi-wire proportional chambers MWPC of the TPC. Locking grid, grounded and anode wire planes, readout pads [90].

Charged particles produced after beam collisions in the central region of the TPC detector enter the sensitive volume of the chamber and ionize gas atoms along

their path. The clusters of electrons created along the particle trajectories then drift to the nearest end wall, where they are registered. The readout electronics system is based on the use of multi-wire proportional chambers with a pad-type readout. There are 12 sectors on each end panel, for a total of 24 sectors. The sectors are divided into outer and inner subsectors (Fig. 7.6). The inner subsectors are in the area of the highest track density, so they are made to have the highest double-hit resolution. The pads on them are smaller (12 mm vs. 20 mm on the outer ones), but their rows are separated by larger gaps relative to their size. This is due to the density limitation of the front-end electronic channels. The outer part of the sector contains larger pads without significant gaps between the rows. This dense arrangement is aimed at optimal determination of the ionization losses dE/dx of charged particles [89]. The multi-wire proportional chamber of the TPC is a circuit board consisting of three wire layers for signal amplification as well as a pad plane for signal readout (Fig. 7.7).

7.1.3 The Time-Of-Flight system (VPD/TOF)

The Time-Of-Flight (TOF) system in the STAR experiment is designed to identify charged hadrons by the measured time it takes them to fly from their origin to the detector wall. The hadron mass can be calculated using information on the particle's momentum determined from the curvature of the trajectory in the TPC detector, trajectory length, and time of flight (see Eqs. 7.1 – 7.4). The STAR TOF system consists of two detectors: VPD (Vertex Position Detector) and TOF (Fig. 7.8). The VPD measures the start time of the event and hence the start time of the particles passing through the detector, and the TOF measures the finish time of the particles.

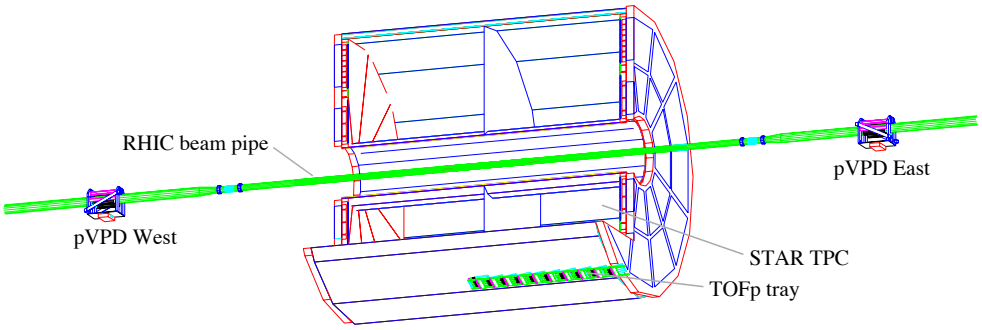

Figure 7.8: The TOF detector is located inside the magnet and around the TPC. Both parts of the VPD — along the pipe on different sides of the TPC [91].

The VPD consists of two scintillation-type subdetectors spaced 5.4 m each on either side of the intended center of the collision region along the beam pipe. Any interesting event is associated with powerful bursts of high energy forward

photons directed in opposite directions from the collision point along the beam pipe region. Each VPD subdetector measures the flash registration time with a resolution of about 30 pc and covers 19% of the full solid angle in the pseudo-rapidity range of $4.4 < |\eta| < 4.9$ [98]. Thus, the time difference between them allows to determine the position of the primary vertex on the Z axis (which explains the name of the detector), and their arithmetic mean — the time of the event start.

The end time of the particle passage through the detector is determined by the TOF detector, whose cylindrical wall has a radius of 220 cm and almost exactly surrounds the TPC, itself being inside the magnet. The basic elements of the TOF are Multi-gap Resistive Plate Chambers (MRPCs), which were developed at CERN for the LHC experiments in the early 2000s. Inside the gaps is a gas with an applied electric field, and particles passing through it ionize atoms, creating electron avalanches that are then registered. The detector covers the full azimuthal angle and pseudo-rapidity range $|\eta| < 1$, and the resolution is on the order of 100 pc [99].

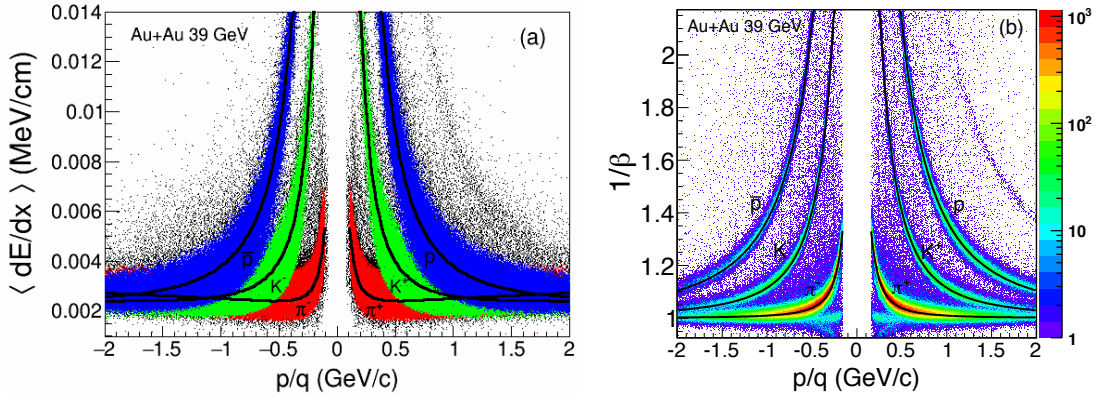

Figure 7.9: Identification of charged particles: on the left — by the dE/dx ionization loss method in TPC, on the right — by time of flight in the VPD/TOF system. The results are given for Au+Au collisions at energies $\sqrt{s}_{NN} = 39$ GeV and for rapidity $y < 1$ [100]. The curves correspond to theoretical values.

Several ways to identify charged particles are available in the STAR experiment. The dE/dx ionization loss detection method used in the TPC has already been mentioned above. TPC acceptance allows the separation of particles of relatively low momentum ($0.1 < p < 0.7$ GeV/c for kaons and $0.1 < p < 1.0$ GeV/c for protons). The TOF system is used to improve the identification of hadrons in the TPC, as well as to extend the range in terms of momentum. Fig. 7.9 shows the dependences of the ionization losses dE/dx for TPC (left) and the inverse-to-rapidity value for TOF (right) on the particle momentum p/q [100]. One can see that TOF significantly complements the identification of hadrons in the region of higher momentum values. This makes it possible to further investigate the

quark composition and dynamics of quarks in the soft part of the spectrum, as well as to study the processes that dominate the transition to the hard part of the spectrum, where fragmentation mechanisms through parton interactions that produce particles with higher transverse momentum are prevalent [91]. The combined use of TPC and TOF makes it possible to identify electrons from dilepton decays of charmed particles, many resonances, study flows and fluctuations, find particle/antiparticle ratios and many other important physics observables. Of particular note is the important role of the TOF in the task of detecting weakly decaying multistrange hyperons under pion-dominated background conditions. Thus, by determining the locations of secondary vertices using the TPC, one can then calculate the trajectory lengths of the daughter particles and establish their masses using the time-of-flight technique.

7.1.4 High Level Trigger (HLT)

The STAR experiment has been running its data acquisition for more than 20 years, since the year 2000. Over this time, the luminosity achieved during single heavy ion collision increased by more than 3 orders of magnitude.

The main STAR detector is the Time Projection Chamber (TPC) installed inside a solenoid magnet. Since the TPC is a gas detector, it cannot work fast enough to record every collision of RHIC accelerator beams. Therefore, it only collects and provides information about the charged particles that have passed through its volume when the detector's readout electronics are turned on. This readout electronics is controlled by a system of triggers, which, based on processing information from the faster STAR detectors, decide whether a given collision can be of interest for further analysis or should be discarded.

The trigger system [92, 93, 94] has evolved in parallel with the evolution of the STAR experiment detector system to effectively exploit the growing range of beam types, energies and luminosities of the RHIC accelerator facility in the STAR physics research program.

Initially, the trigger system consisted of four levels. Working sequentially one by one, the triggers filtered out events according to specific criteria, thus reducing the amount of data at each level and increasing the time to process the data in the subsequent level trigger.

Level 0 was designed to work synchronously with the RHIC beam crossing cycle and to select potentially interesting events. Level 1 could analyze coarse event features and interrupt data collection for 40 μs of secondary electron drift time in the TPC. Level 2 could already analyze the calorimeter data in more detail and interrupt data collection within 5 ms of the TPC data being transferred from the detector. Finally, after all the STAR data had been collected in the DAQ, the level 3 trigger could reconstruct the tracks in the TPC and use this information

to make a final decision on whether to accept or reject that collision.

The Level 3 trigger was developed by a group of physicists at the University of Frankfurt am Main and first launched in 2002. The track reconstruction in the TPC detector was based on a conformal transformation algorithm [95], where circular trajectories of charged particles in the TPC detector volume were transformed into straight lines, making them much easier to find.

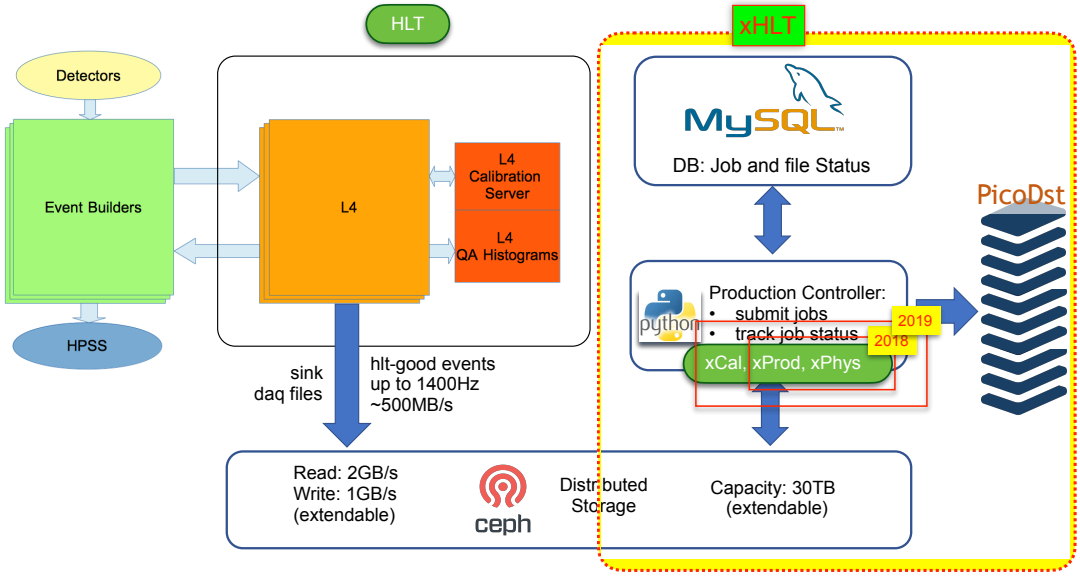

Figure 7.10: Block diagram and basic modules of the High Level Trigger HLT [97] .

In 2009, the STAR experiment upgraded the DAQ1000 data acquisition system, increasing the data acquisition capability to 1 KHz for Au+Au collisions at $\sqrt{s}_{NN} = 200$ GeV. A High Level Trigger (HLT) [96] (Fig. 7.10) was developed as a further development of the Level 3 trigger to enable fast reconstruction and real-time event selection. Measurements from each of the 24 sectors of the TPC were processed independently and in parallel, but scaling the computations was not technically possible due to the computer farm architecture.

In 2013, the HLT was equipped with its own autonomous computer farm, and both the speed and efficiency of track reconstruction were significantly improved by replacing the old conformal transformation algorithm with a new one based on Cellular Automaton (CA). The new track search algorithm, while faster, also has significant scalability, making it ideal for running on modern parallel many-core computer architectures. In addition, the track search algorithm based on the cellular automaton has demonstrated significantly higher track reconstruction efficiency under conditions of high track multiplicity, especially for central heavy ion collisions, outperforming even the standard track search algorithm in STAR, based on the track following procedure, by 10%. Also, the cellular automaton-based algorithm is capable of reconstructing both primary and secondary tracks,

regardless of which region of the detector system they were produced in. As a result, the use of the CA tracker has made it possible to do complete event reconstruction already at the stage of event selection in HLT.

In 2018, the KF Particle Finder package based on the Kalman filter was experimentally incorporated into the HLT chain of processing algorithms. And in 2019, a functionality was added to the HLT to calibrate and align the detector system STAR [97] (Fig. 7.10).

Thus, the High Level Trigger is now a universal platform for full processing and comprehensive analysis of heavy ion collisions in real time. During the work on the BES-II program, the KF Particle Finder package has demonstrated its high efficiency and speed, enabling online physics analysis of collisions on the HLT computer farm.

7.2 Application of the method to real data of STAR

Very important, especially for the initial stage of the CBM experiment, which is planned for the year 2025, to demonstrate already now on real data the reliability of the developed approach, as well as the high efficiency of the current implementation of both the entire KF Particle Finder package, and its integral part, implementing the missing mass method. Such an opportunity was provided by the FAIR Phase-0 program, which allows the use in the STAR experiment of software packages originally developed for the CBM experiment.

Since the track reconstruction in the STAR experiment assumes measurements in the TPC detector at a distance of more than 50 cm from the collision point, the Σ hyperon tracks cannot be found due to the short lifetime of these particles: $c\tau_{\Sigma^+} = 2.4$ cm, $c\tau_{\Sigma^-} = 4.4$ cm. However, the correctness of the missing mass method can be tested by reconstructing the decays of numerous strange mesons, such as $K^+ \to \pi^+\pi^0$ and $K^- \to \pi^-\pi^0$, with significantly longer lifetimes.

Therefore, to prove the feasibility of the missing mass method in the STAR experiment, the method was first applied offline to data already collected in 2016, obtained in collider mode (opposite-beam collision mode), on a set of 700 K Au+Au collisions at $\sqrt{s_{NN}} = 200$ GeV collision energy. These are quite challenging events with a large multiplicity of particles produced in the collision. An example of such a collision is shown in Figure 7.11. Reliable reconstruction of strange meson decays by the missing mass method with such high particle multiplicity and high track density is a non-trivial task.

The results obtained (Fig. 7.12) showed the high quality of the reconstructed mother particles and their neutral daughter particles [A11] even under such difficult conditions. This demonstrated that the missing mass method works reliably

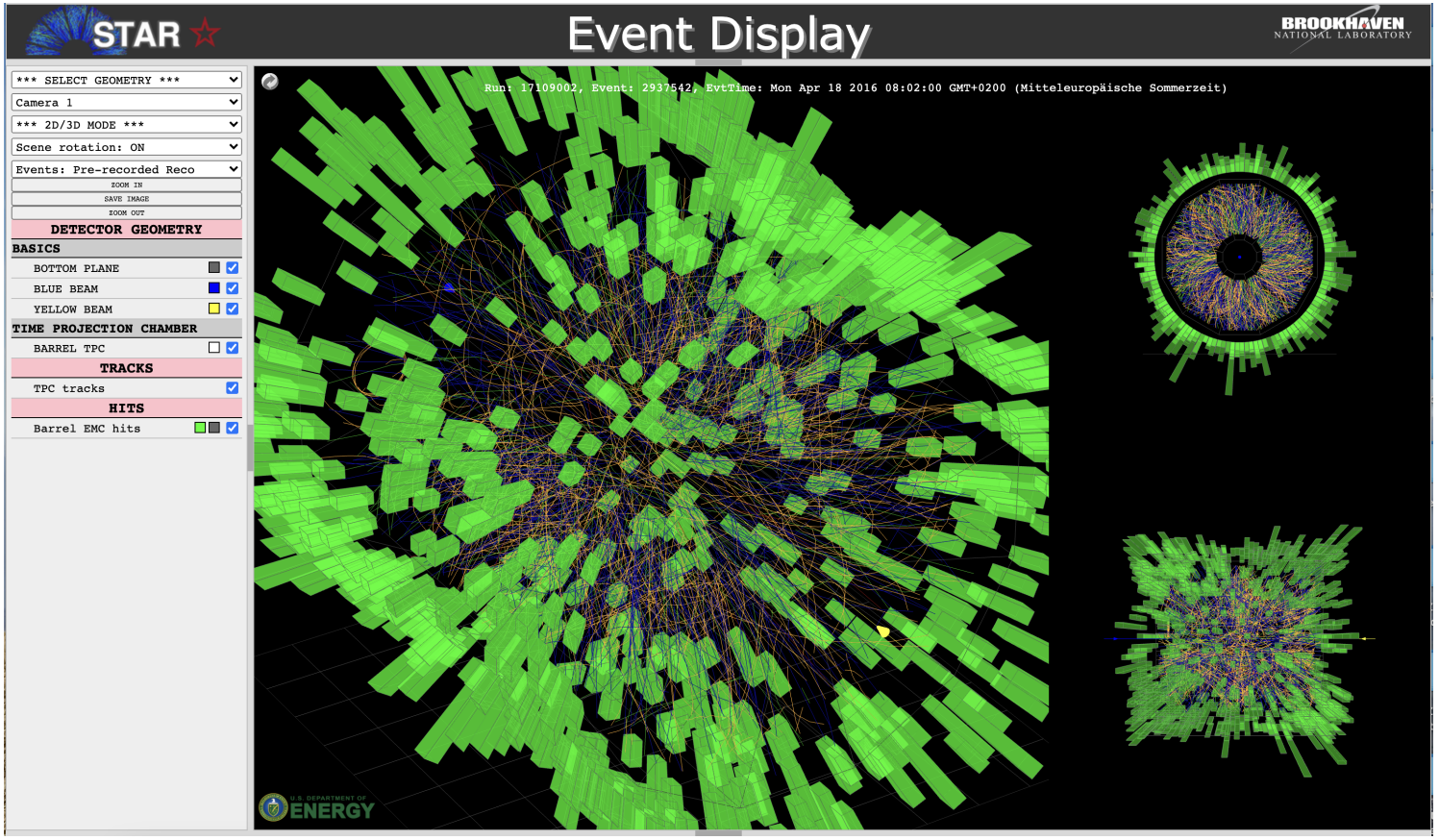

Figure 7.11: Example of a collision of two gold nuclei (Au+Au) at 200 GeV in the STAR experiment (Run-2016). The reconstructed event is presented as a so-called three-dimensional image, with the top right being the frontal view and the bottom right being the side view. The tracks of different types of particles reconstructed in TPC are shown with lines of different colors. The tracks of low-energy particles in the magnetic field have a bigger curvature, while the tracks of high energy particles appear as almost straight lines. The green color shows the triggered blocks of the electromagnetic calorimeter.

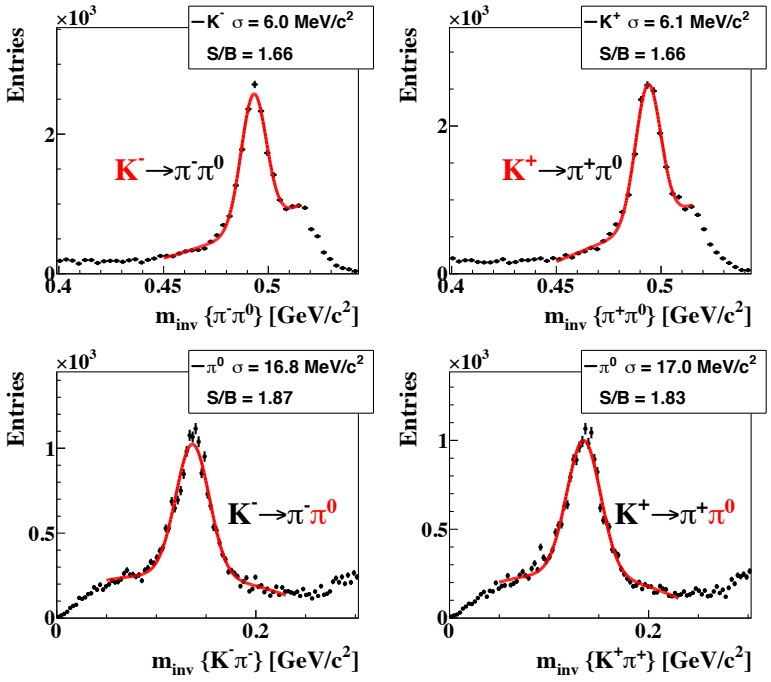

Figure 7.12: Mass spectra of K^- and K^+ obtained by the missing mass method, together with their reconstructed neutral daughter particles π^0 on a set of 700 K Au+Au collisions at collision energies $\sqrt{s_{NN}}$ = 200 GeV (2016 experimental data) [A11].

and efficiently within the KF Particle package on real data in the STAR experiment.

The second phase of the RHIC beam energy scan BES-II (2019–2021) [85] aims to investigate in Au+Au collisions the high-baryon density region of the QCD phase diagram. The BES-II physics program is a continuation and refinement of the BES-I program, which was conducted in 2010-2014. Key measurements include net-proton kurtosis, which can indicate precisely the position of the critical point, directional flow, which can confirm EOS softening, and recovery of chirality in the dilepton channel.

The fixed-target program achieves larger μ_B values and with higher luminosity compared to the collider mode. The inner target is a thin gold foil inserted into the beam pipe at a distance of 2 m from the nominal beam collision point, and only one circulating beam is directed to collide with it.

More accurate measurements in BES-II are possible due to the order of magnitude better statistics provided by the upgrade of the electron cooling system in the RHIC as well as the detector upgrades, primarily upgrading the inner part of the Time Projection Chamber (iTPC) [103] and the endcap Time Of Flight (eTOF)) [104] detector.

The main goals of the iTPC upgrade, replacing all 24 existing inner TPC sectors

with new ones, are greater rapidity coverage, lower p_T cutoff, better momentum resolution, and better dE/dx resolution. This increases the $|\eta|$ coverage from 1 to 1.5, and the lower threshold for the reconstructed particle momentum p_T in the iTPC is decreased from 125 MeV/c to 60 MeV/c.

The eTOF was also upgraded as part of the FAIR Phase-0 program by the CBM and STAR collaborations to install at STAR 10% of the full TOF detector system of the CBM experiment. The eTOF detector covers the -1.1 to -1.6 rapidity range, that is, only one side of the STAR detector setup. Combined with the iTPC upgrade, the eTOF upgrade provides additional forward particle identification capabilities, significantly improving the fixed-target program at BES-II.

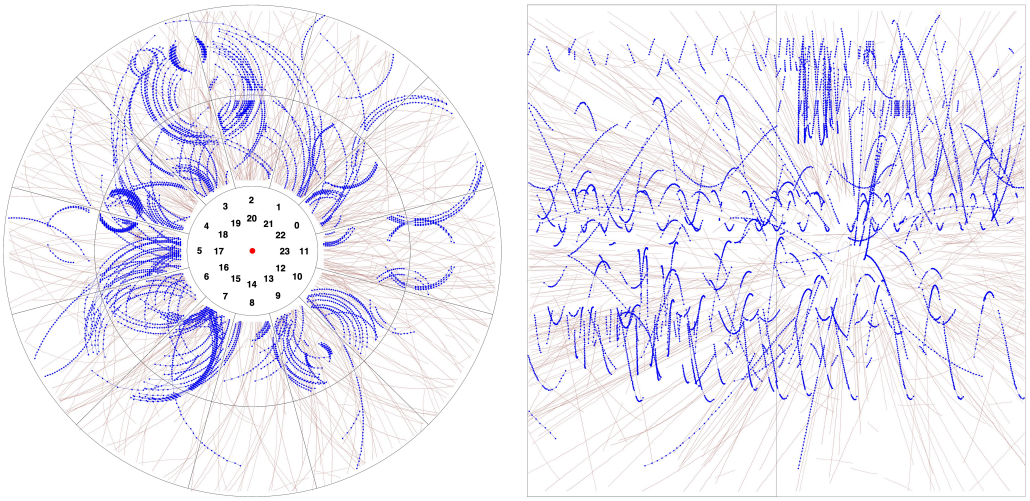

Figure 7.13: Example of a cellular automaton track search on a reconstructed event with 30 low-momentum return tracks, and other 346 reconstructed tracks shown in background color.

The iTPC and eTOF upgrades required significant modifications to all event reconstruction algorithms.

For example, in the track reconstruction algorithm based on the cellular automaton, the reconstruction efficiency of low-momentum particles, including low-energy particles that make several turns inside the TPC, the so-called loopers, has been increased to meet the requirements for reconstruction in the extended acceptance of the iTPC detector, as well as in the forward direction of the eTOF detector. The difficulty in reconstructing such particles is due both to their typical difficulties, such as long generated clusters, significant multiple scattering, and energy losses, and to the fact that the track model itself fundamentally involves particle travel from the center of the detector system to the outer PID detectors.

Figure 7.13 shows a reconstructed event with 30 return tracks as an illustration of the complexity of the problem. In this event, all phases of the return trajectories

are merged in the merge phase into long tracks, which, however, is not shown in the figure because of the technical requirement to follow the traditional track model. The other 346 tracks reconstructed in the standard way are also shown in the background color to represent the completeness of the collision topology. In addition, in the front view, the middle circle shows the division of the TPC detector into the inner (iTPC) and outer parts.

Running iTPC and eTOF detectors in STAR, as well as working online in fixed-target mode, also required substantial adaptation of the KF Particle Finder package. For example, a modification was made to the algorithm for cleaning the background from particles knocked out of the detector material in the area of the beam pipe and the separator between the inner and outer parts of the TPC.

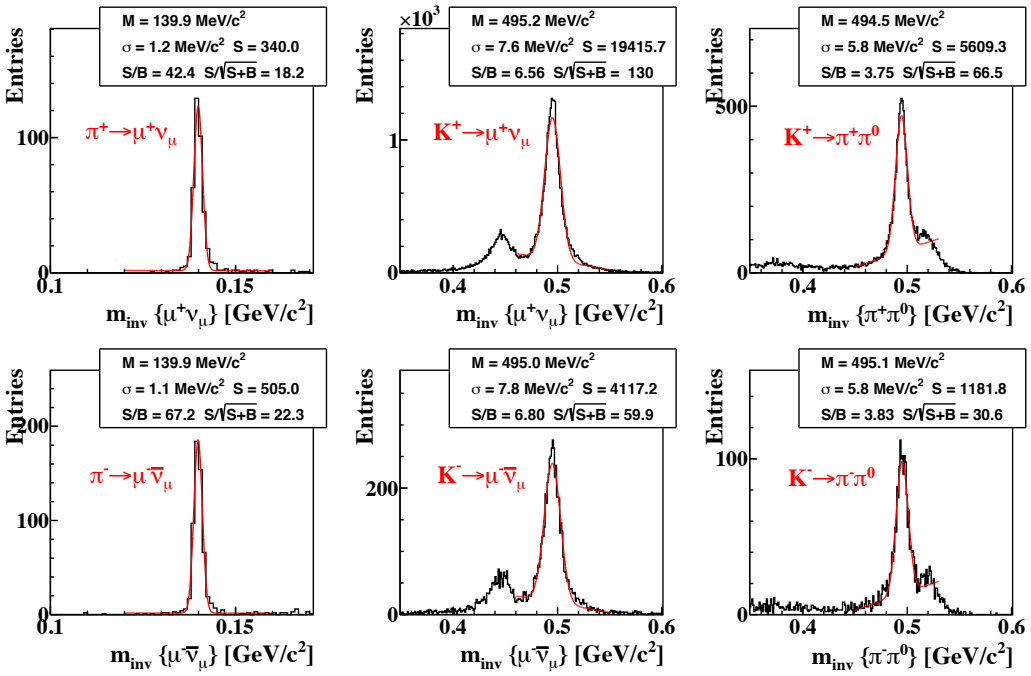

Figure 7.14: Results of the initial version of the missing mass method on 2020 data with a fixed target of 2 M Au+Au collisions at beam energies of 5.75, 7.3, 9.8 and 26.5 GeV/n [A15] (the second peak in $K^{\pm}$ decays is the result of misidentifying π as μ in an incomplete online calibration).

The missing mass method, both in its initial (Fig. 7.14) and then in its improved version (Fig. 7.15), has been used in real time to search for pion ($\pi^{\pm} \to \mu^{\pm}\nu$) and kaon ($K^{\pm} \to \mu^{\pm}\nu$ and $K^{\pm} \to \pi^{\pm}\pi^{0}$) decays in data from 2 M Au+Au collisions at energies 5.75, 7.3, 9.8, and 26.5 GeV/n fixed-target data collected in 2020 in the BES-II program and reconstructed online using a chain of express processing and data analysis algorithms on the STAR HLT computer cluster [A15].

The improvements of the missing mass method have led to a significant increase in

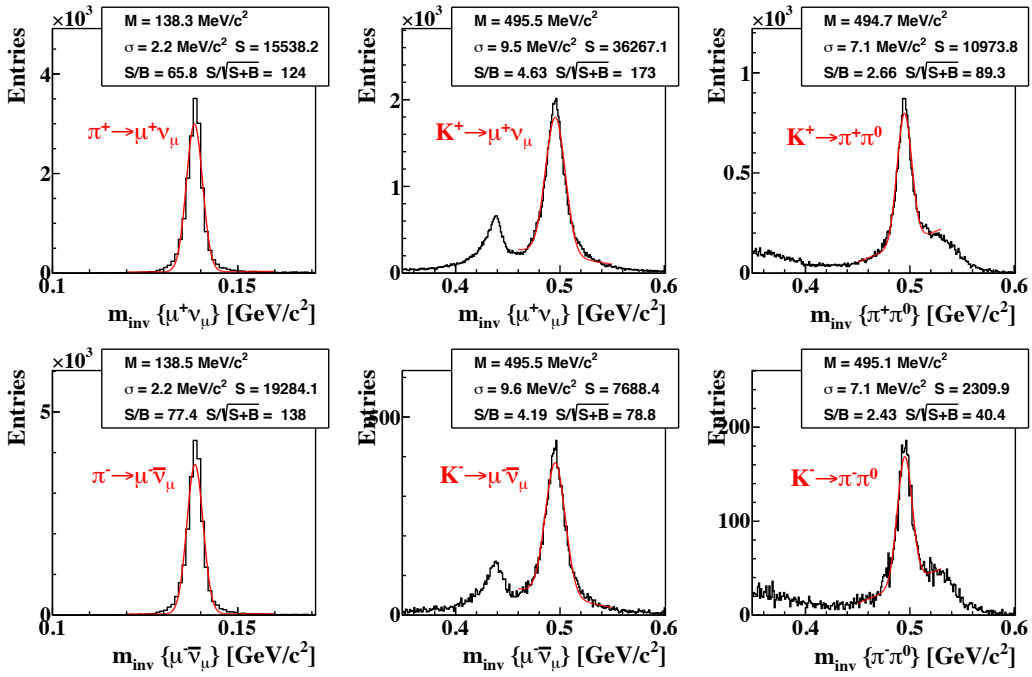

Figure 7.15: Results of the improved version of the missing mass method on 2020 data with a fixed target of 2 M Au+Au collisions at beam energies of 5.75, 7.3, 9.8 and 26.5 GeV/n [A15].

the efficiency of the search for short-lived particles in the STAR experiment when working with real data (Tab. 7.1). Thus, in the pion decay channels $\pi^{\pm} \to \mu^{\pm}\nu$ the signal increased by a factor of 40, and the significance by a factor of 7. In the $K^{\pm} \to \mu^{\pm}\nu$ and $K^{\pm} \to \pi^{\pm}\pi^0$ kaon decay channels, the signal increased by a factor of 2 and the significance by a factor of 1.5.

The rich physics program of BES-II also required fast data processing and preliminary real-time physics analysis in order to be able not only to monitor the quality of the collected data, but also to evaluate the achievement of the expected physics result during data acquisition, and if necessary to make adjustments to the accelerator operation plan.

For this purpose, the functionality of the High Level Trigger (Fig. 7.16) was significantly expanded, resulting in the so-called express chain of data processing and analysis in addition to the standard trigger tasks of selecting events to store them on the medium. Within the express chain, all necessary tasks, namely online calibration, reconstruction and analysis of the data, were performed on the free resources of the HLT computer cluster.

The express calibration was performed in real time using the same algorithms as the standard offline data processing. Therefore, the online data calibration was actually the first step in the full calibration process, which reduced the time

Table 7.1: Comparison of the number of reconstructed signal particles in the initial and improved versions

Version	$\pi^{\pm} \to \mu^{\pm}\nu_{\mu}$		$K^{+} \to \mu^{+}\nu_{\mu}$		$K^{\pm} \to \pi^{\pm}\nu^{0}_{\pi}$	
Initial	340.0	505.0	19415.7	4117.2	5609.3	1181.8
Improved	15538.2	19284.1	36267.1	7688.4	10973.8	2309.9
Factor	45.7	38.2	1.9	1.9	2.0	2.0

to achieve the final calibration. Track reconstruction was performed using the cellular automaton based track finder, which was a more advanced and faster version of the standard cellular automaton based track finder used in the standard offline data processing. Physics analysis of the data was also performed using the more advanced KF Particle Finder package compared to the offline data processing package.

It should be noted that the express processing and data analysis were performed with incomplete detector calibration and alignment, which created additional challenges for the reconstruction and analysis algorithms.

The express processing was performed on the HLT computer cluster under limited computing resources and disk space so as not to interfere with the traditional HLT tasks, namely, real-time analysis and selection of heavy ion collisions. Therefore, the express chain did not process and analyze all the data, but only a fraction, depending on the intensity of the data acquisition, but on average about 30%. If necessary, additional resources of the main RCF computer farm could be used, where fast real-time offline processing was also performed to control the detector systems during data acquisition.

The complete procedure of the express processing of new data from data acquisition to obtaining physics results usually took about an hour of work on the HLT cluster, but if there was a need for a more detailed study of the acquired data or the detector operation, additional processing cycles were performed, which could take up to one day.

The data processed in the express chain were copied in picoDST format to the RCF farm for possible further analysis by different physics groups as part of the standard offline analysis chain. It should be noted, however, that neither the express data processing nor the fast online data processing interfered with the standard offline data processing chain.

As a result, the need for fast online data processing and analysis led to the development of faster and better algorithms, which would later be incorporated into the structure of the standard offline data processing in the STAR experiment.

In addition, the use of similar, and often identical, algorithms in both online and

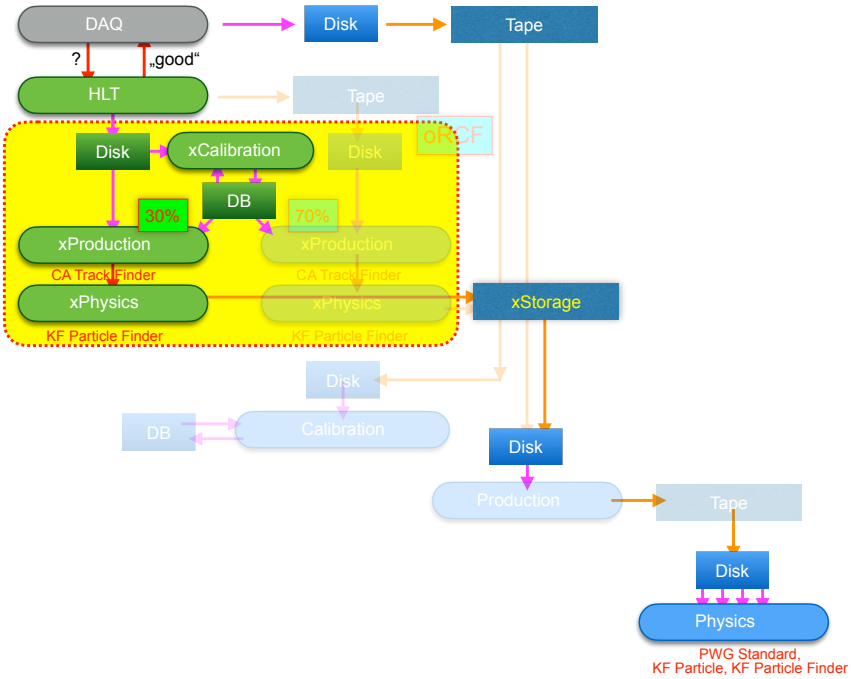

Figure 7.16: A diagram of the online data analysis in the express processing on the computer cluster of the STAR High Level Trigger [A18, A19].

offline data processing creates a bridge between the online and offline processing chains, which allows to consider the express data processing and analysis as the first stage of the standard data processing and analysis. Moreover, the results of data analysis in the express chain can serve as a reliable estimate of the final analysis that will be obtained after the final calibration is completed and the standard offline data processing is performed.

Figure 7.17 shows the results of applying the missing mass method within the express chain to 9 M Au+Au data obtained 1–2 May 2021 at beam energy 3.85 GeV/n in the fixed-target mode. The method was used to find decays $\pi^+ \to \mu^+\nu_\mu$, $\pi^- \to \mu^-\bar{\nu}_\mu$, $K^+ \to \mu^+\nu_\mu$, $K^- \to \mu^-\bar{\nu}_\mu$, $K^+ \to \pi^+\pi^0$ and $K^- \to \pi^-\pi^0$.

Application of the method to real data shows very good results with a high signal-to-background ratio and a large value of significance [A18, A19]. In the case of pion decays $\pi^\pm \to \mu^\pm\nu$ it was possible to obtain a nearly clean signal with almost complete absence of background. In the kaon decays $K^\pm \to \mu^\pm\nu$ a second peak from the kaon decay into two pions is observed, which is the result of misidentification of π as μ.

It should be noted again that these results were obtained during the online data analysis in the express chain on the HLT cluster, while the detector system was still undergoing calibration and alignment. With the standard offline data pro-

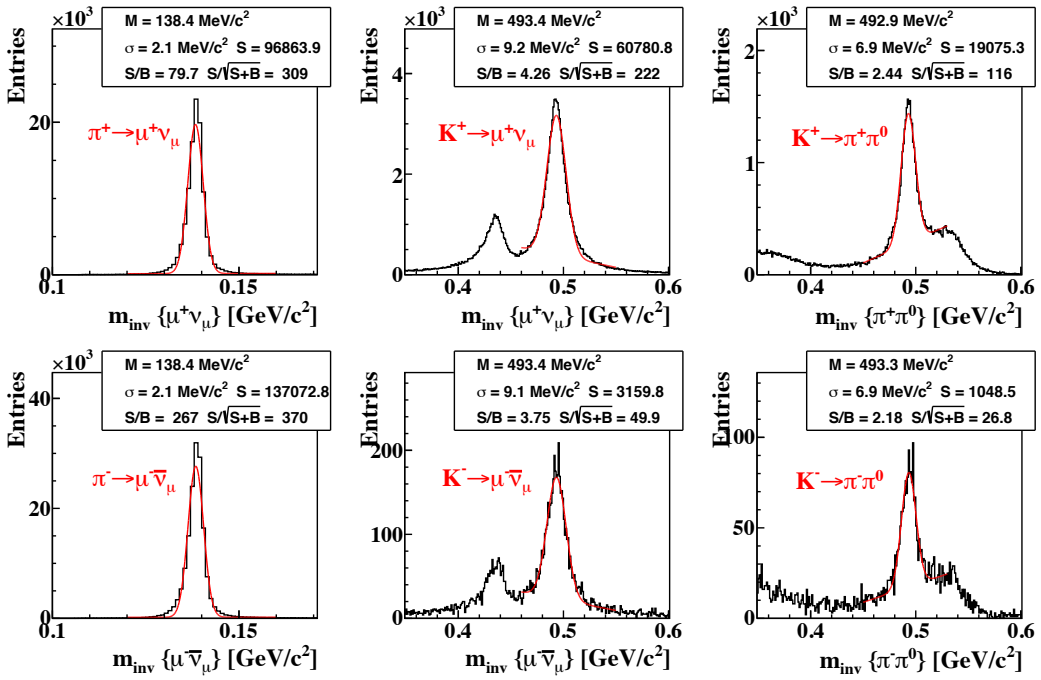

Figure 7.17: Mass spectra for $\pi^{\pm} \to \mu^{\pm}\nu_{\mu}$, $K^{\pm} \to \mu^{\pm}\nu_{\mu}$ and $K^{\pm} \to \pi^{\pm}\pi^{0}$ obtained by the missing mass method using 9 M Au+Au collisions with fixed target at beam energy 3.85 GeV/n, collected 1–2 May 2021 and processed online as part of the express chain on the HLT cluster [A19].

cessing, the results will be improved due to full calibration of all detector systems of the STAR setup.

The obtained results demonstrate the reliability and high efficiency of the implementation of the missing mass method in the reconstruction of both charged parent particles and their neutral daughter particles.

It should also be noted that the high quality of the results, obtained from the express analysis of the data, led to their status of preliminary physics results with the right to present them at international physics conferences and meetings on behalf of the STAR Collaboration.

The BES-II (2019–2021) physics program was very successful, also due to the timely and reliable real-time processing of the data on the HLT cluster in the express stream. All planned data for Au+Au collisions at energies of $\sqrt{s_{NN}} =$ 7.7–27 GeV in the collider mode and energies of $\sqrt{s_{NN}} =$ 3–7.7 GeV in the fixed target mode were successfully collected.

As an integral part of the KF Particle Finder package, now the primary approach for reconstruction and analysis of short-lived particles in the STAR experiment, the missing mass method will continue to be used for physics analysis in online

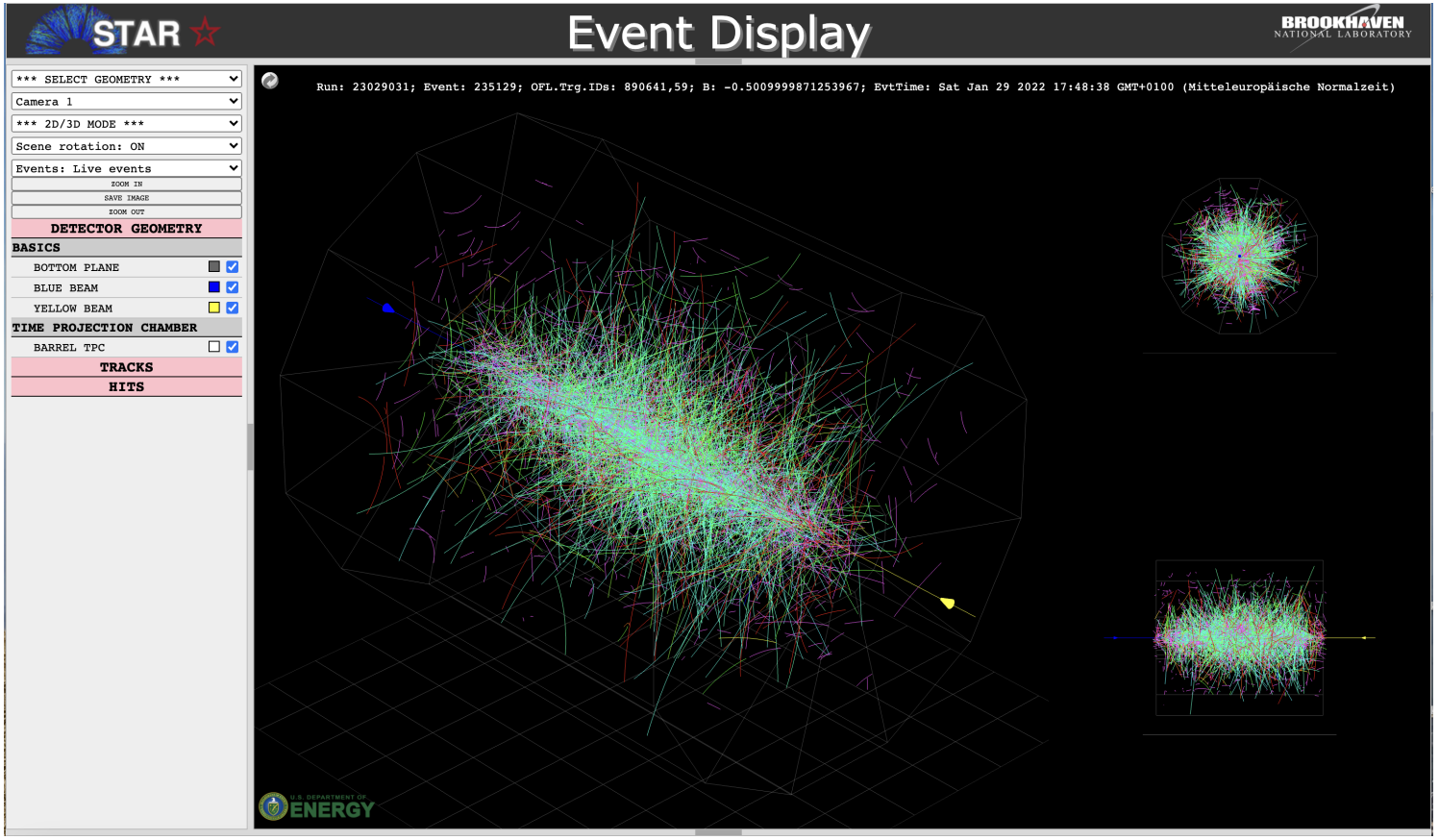

Figure 7.18: Example of multiple collisions of two transversely polarized proton beams (pp) at 510 GeV energy in the STAR experiment, reconstructed at the HLT cluster in real time (January 29, 2022). The reconstructed event is presented as a so-called three-dimensional image, top right — frontal view, bottom right — side view. The tracks of different types of particles reconstructed in TPC are shown by lines of different colors. The tracks of low-energy particles in the magnetic field have a large curvature, while the tracks of high energy particles appear as almost straight lines.

and offline modes.

In particular, the physics research program of the STAR experiment for 2022 includes, with the highest priority, studying the physics of proton-proton collisions of transversely polarized beams at 510 GeV. One of the complexities of these high energy collisions is the presence of a so-called pile-up, where an interesting trigger collision of particles is superimposed by several other simultaneous collisions of beam particles (Fig. 7.18).

Reconstructing the topology of many such collisions and then extracting exactly the trigger collision among them places high demands both on the algorithm for reconstruction of trajectories of stable and long-lived particles based on the cellular automaton and on the algorithms of the KF Particle package for searching short-lived particles in complex conditions of large particle multiplicity and high density of their trajectories. Preliminary processing of this data shows the reliability and high quality of the reconstruction algorithms.

Similar challenges will also arise for the collision reconstruction algorithms of the FLES package in the CBM experiment. Therefore, based on the results and experience of applying these algorithms to real data in the STAR experiment, one can be confident that the analysis of heavy ion collisions in the CBM experiment will be successful, starting from the very first day of the experiment in 2025.

Chapter 8

Conclusion

Here we briefly summarize the results of the research completed as part of this dissertation.

Scientific novelty

1. For fast search and reconstruction of short-lived particles with neutral particles in their decay products, especially rare decays of strange particles such as $\Sigma^- \to n\pi^-$, $\Sigma^+ \to p\pi^0$, $\Xi^- \to \Lambda\pi^-$ and $\Omega^- \to \Lambda K^-$, the missing mass method and a corresponding set of parallel algorithms, based on Kalman filter mathematics, for operation in modern and future high energy physics and heavy ion physics experiments have been developed.

2. Within the developed approach and during testing of the algorithm on simulated data of the CBM experiment, the principles and the most optimal values of the signature parameters that allow high accuracy signal extraction and minimization of the background are identified. In particular, methods were developed to suppress the physical background originating from the interaction of particles with the material and stations of the detector system, as well as the combinatorial background from incorrectly reconstructed tracks corresponding to the same particle, but interpreted as two particles, a mother and daughter, from the same decay.

3. For the purpose of this research, two methods independent of each other have been adapted and successfully implemented to study particle spectra: side-band and multi-differential analysis. Both methods allow to reliably calculate different kinds of efficiencies, as well as to extract important physics parameters, such as the effective temperature.

4. The missing mass method is implemented using vector (SIMD) instructions and optimized for parallel operation on modern many-core high

performance computer systems, which can include both processors and co-processors. The complex of algorithms was tested on computers with dozens of cores and showed high speed and almost linear scalability.

5. The missing mass method is implemented as a part of the software packages KF Particle and KF Particle Finder [65, 67], [A9]–[A19] for reconstruction and analysis of a wide range of short-lived particle decays based on the Kalman filter. The method has been used regularly in the CBM experiment to analyze simulated data, and as part of the FAIR Phase-0 program in the STAR experiment to analyze real data.

Practical value

Using Monte Carlo generated data simulated with UrQMD, PHSD, PLUTO, and GEANT3 packages for the case of the CBM setup, it has been shown that the missing mass method can reliably reconstruct and identify short-lived neutral particles in the decay channel using a set of trajectories (tracks) of mother and daughter charged particles and identification with the Time-Of-Flight TOF detector [32]. High values of efficiency, significance, and signal-to-background ratio have been achieved in numerous studies. For the planned operating conditions of the CBM experiment, the efficiency of the method itself is more than 60%. The full efficiency in 4π space without considering detector acceptance, for example, for $\Sigma^- \to n\pi^-$ decay is 6.1% with a signal-to-background ratio ≈ 20 and significance ≈ 1200, which is an indicator of the high performance of the method in the physics analysis of the decays of strange particles.

The missing mass method provides a unique opportunity to extend the physics program of high energy physics and heavy ion experiments to study strange particles, including coverage of an additional kinetic region, not visible in the standard approach, for such rare decays as $\Xi^- \to \pi^-(\Lambda \to n\pi^0)$ and $\Omega^- \to K^-(\Lambda \to n\pi^0)$. In addition, the reconstruction of the parameters of short-lived particles by two independent methods allows a detailed analysis of systematic errors.

Within the FAIR Phase-0 program, the KF Particle and KF Particle Finder packages for searching and reconstruction of short-lived particles, originally developed for the CBM experiment, have been adapted for the STAR experiment and applied to real data from the beam energy scan BES-II physics program with energy range from 20 to 3 GeV in collider mode and in fixed target mode [85]. As an integral part of these packages, a set of algorithms implementing the missing mass method has also been adapted for the STAR experiment, and has been successfully used to search and reconstruct the decays of $\pi^+ \to \mu^+\nu_\mu$, $\pi^- \to \mu^-\bar{\nu}_\mu$, $K^+ \to \mu^+\nu_\mu$, $K^- \to \mu^-\bar{\nu}_\mu$, $K^+ \to \pi^+\pi^0$ and $K^- \to \pi^-\pi^0$, thus demonstrating its high reliability and also its ability to process data fast in real time on the HLT [A11, A15, A18, A19] computer cluster using only free computing resources.

Like other algorithms of the KF Particle and KF Particle Finder packages, the missing mass method is implemented taking into account the complex architecture of modern many-core computer systems. Thus, the set of algorithms realizing the method is vectorized using the SIMD instruction set for parallel operation within a single processor core. Also, the set of developed algorithms runs in parallel on many CPU cores, including virtual cores of Intel Hyper-Threading technology, and shows close to linear scalability with increasing number of CPU cores.

Validity of the results

The validity and feasibility of the results obtained in the thesis have been confirmed by both the application to the reconstruction and physics analysis of events simulated using UrQMD, PHSD, PLUTO, GEANT3 and CBMROOT in the CBM experiment, and real data from the BES-II physics research program of the STAR experiment in online mode. A set of implemented algorithms has been used to analyze data of different types of collisions and energies. The characteristic distributions of the reconstructed parameters of the particles and their covariance matrices show the mathematically correct form, which confirms the high quality of the reconstruction of the physics parameters.

Presentation of the main concepts and results

The main concepts and results described in the thesis have been presented and discussed at international conferences and meetings:

- International Conference "Ultrarelativistic Heavy-Ion Collisions — Quark Matter" (QM 2017) (Chicago, USA, 2017);
- International Conference "Computing in High-Energy and Nuclear Physics" (CHEP 2019, 2021) (Adelaide, Australia, 2019; Geneva, Switzerland, 2021 (virtual));
- International Meeting "Advanced Computing and Analysis Techniques in Physics Research" (ACAT 2021) (Daejeon, South Korea, 2021 (virtual));
- International Conference "Mathematical Modeling and Computational Physics" (MMCP 2017) (Dubna, Russia, 2017);
- International conference "Distributed Computing and Grid Technologies in Science and Education" (Dubna, Russia, 2021);
- Annual Meetings "DPG-Frühjahrstagungen" (Germany, 2016, 2017, 2018, 2019);
- International Meetings of the CBM Collaboration (2013, 2015, 2016, 2017, 2018, 2019, 2021, Germany, Russia, Czech Republic, China);

- International meetings "Common CBM–STAR Reconstruction and Analysis Software Approaches" (BNL, Brookhaven, USA, 2015, 2016).

Publications

There are 19 scientific papers published on the topic of this dissertation, where the articles A[1] – A[5] were published in peer-reviewed journals:

- The European Physical Journal A ([A1]),
- Letters to the journal "Physics of elementary particles and atomic nuclei" ([A2] – [A4]),
- Bulletin of the Russian University of People's Friendship, series "Mathematics. Informatics. Physics" ([A5]),
- in the form of JINR Reports ([A6] – [A7]),
- in the materials of international meetings of the CBM Collaboration ([A8] – [A15]),
- in the proceedings of international conferences ([A16] – [A19]).

Personal contribution of the author

The statements and results presented in the thesis were obtained with the decisive participation of the author. The software implementation of the developed methods and algorithms was performed personally by the author.

The statements of the defense

1. Development of the mathematical apparatus of the missing mass method for searching and reconstruction of short-lived particles with neutral particles in their decay products.
2. Implementation of the missing mass method as a set of fast algorithms using SIMD (Single Instruction, Multiple Data) vector instructions and OpenMP (Open Multi-Processing) directives and procedures for efficient parallel operation on many-core computer architectures, which may include both processors and coprocessors.
3. Adaptation of the set of algorithms implementing the missing mass method to work as a part of the KF Particle and KF Particle Finder packages to search and reconstruct short-lived particles.

4. Development and optimization of a procedure for searching for short-lived particles with neutral particles in decay products based on the set of algorithms implementing the missing mass method for efficient reconstruction of strange particles in the KF Particle and KF Particle Finder packages for the heavy ion experiment CBM (FAIR/GSI, Germany).

5. Adaptation of the set of algorithms implementing the missing mass method and the procedure of searching for strange particles to process and analyze data in the heavy ion experiment STAR (BNL, USA) in real time on the High Level Trigger computer cluster.

6. Implementation of two independent methods to study particle spectra, side-band and multi-differential analysis, to reliably calculate different kinds of efficiencies, and to extract important physics parameters of the medium, such as the effective temperature.

Conclusion

Finally, here are the main results obtained in the dissertation:

1. In the CBM experiment with heavy ions, the missing mass method and the corresponding set of parallel algorithms, based on the Kalman filter mathematics, for the fast search and reconstruction of rare short-lived particles with neutral particles in their decay products have been implemented. Improvements in the mathematical apparatus of the method have led to a 2 fold increase in their reconstruction efficiency and a 25–30% increase in the significance of the signal data.

2. The missing mass method is implemented using vector (SIMD) instructions, and optimized for parallel operation on modern many-core high performance computing systems, which can include both processors and co-processors.

3. In the framework of the developed approach, the principles and the most optimal values of the feature variables, which allow to extract the signal with high accuracy and to minimize the background, are identified. In particular, methods have been developed to suppress the physical background originating from the interaction of particles with the material and stations of the detector system, as well as the combinatorial background from incorrectly reconstructed tracks corresponding to one particle, but interpreted as two particles, a mother and daughter, from the same decay.

4. For physics analysis of short-lived particle properties, two independent methods are implemented to study particle spectra: side-band and multi-differential analysis. Both methods provide a reliable calculation of various

efficiencies, as well as the extraction of important medium parameters, such as the effective temperature.

5. A set of algorithms implementing the missing mass method has been adapted for the STAR experiment with heavy ions and successfully used in the BES-II physics research program to search and reconstruct decays $\pi^+ \to \mu^+\nu_\mu$, $\pi^- \to \mu^-\bar{\nu}_\mu$, $K^+ \to \mu^+\nu_\mu$, $K^- \to \mu^-\bar{\nu}_\mu$, $K^+ \to \pi^+\pi^0$ and $K^- \to \pi^-\pi^0$ online on the High Level Trigger computer cluster using only free computing resources. In the improved version of the missing mass method, the signal in the $\pi^\pm \to \mu^\pm\nu$ channels increases by a factor of 40 and the significance by a factor of 7. In $K^\pm \to \mu^\pm\nu$ and $K^\pm \to \pi^\pm\pi^0$ channels, the signal increases by 2 times and the significance increases by 1.5 times compared to the initial version.

Acknowledgements

I would like to take this opportunity to express my gratitude to the many people who have helped and supported me along my difficult path in learning science and, in particular, in the preparation of this dissertation.

I want to sincerely thank Prof. Dr. Volker Lindenstruth for his strong support of me during this difficult (unfortunately for so many people) time. His support made it possible for me to submit my dissertation for defense.

I want to thank Prof. Dr. Peter Senger for his long and patient participation in the development of my scientific research on the search for strange particles in the CBM experiment. My sincere thanks to the entire GSI team of the CBM experiment, and especially to Dr. Iouri Vassiliev, Dr. Anna Senger, and Dr. Maksym Zyzak, with whom I worked together in our office for many years and will always remember with the kindest words.

My special thanks to Dr. Maksym Zyzak for his numerous detailed explanations of the mathematics of the Kalman filter, as well as the features of its implementation. Also my knowledge and skills of parallel programming are obtained by following his recommendations and hints.

I would also like to thank the members of the BNL group of the STAR experiment, especially Dr. Yuri Fisyak, for giving me the opportunity to work with this excellent team of passionate scientists.

My great appreciation goes to Prof. Victor Ivanov for his continuous and caring attention over the years to both my research work and my life in general.

I am very grateful to all my friends who have always accepted me as I am, especially Grigory Kozlov, Artemiy Belousov, Mykhailo Pugach, Dr. Maksym Zyzak and many others.

I want to thank my dear parents, Elena Konotopskaya and Ivan Kisel, for their unconditional support and help in my striving to become independent, as well as all my distant and close relatives, especially Elena Kisel for her inexhaustible positive vision of my future.

Thank you all!

Bibliography

[1] Particle Data Group, Lawrence Berkeley National Laboratory, picture from `http://www.particleadventure.org/history-universe.html`

[2] C. Flammarion, "L'atmosphère: météorologie populaire", 1888.

[3] The Particle Adventure, picture from `http://www.particleadventure.org`

[4] Standard Model, picture from `https://en.wikipedia.org/wiki/Standard_Model`

[5] S. Braibant, G. Giacomelli, M. Spurio, "Particles and Fundamental Interactions. An Introduction to Particle Physics", Springer, 2012.

[6] R. Vogt, "Ultrarelativistic Heavy Ion Collisions", Elsevier, 2007

[7] J. Bartke, "Introduction to Relativistic Heavy Ion Physics", World Scientific, 2009.

[8] C. Loizides, "From Heavy-Ion Collisions to Quark-Gluon matter", CERN summer student programme, 2016.

[9] F. Karsch, "Lattice results on QCD thermodynamics", Nuclear Physics A, 698 (2002) 199.

[10] N. Cabibbo and G. Parisi, "Exponential hadronic spectrum and quark liberation", Phys. Lett. 59B (1975) 67.

[11] E. Fermi, "High energy nuclear events", Progr. Theor. Phys. 5 (1950) 570.

[12] E. Fermi, "Angular distribution of the pions produced in high energy nuclear events", Phys. Rev. 81 (1951) 683.

[13] L. Landau, "On the multiple production of particles in high energy collisions", Izv. Akad. Nauk SSSR, Ser. Fiz. 17 (1953) 51.

[14] R. Hagedorn, "Statistical thermodynamics of strong interactions at high energies", Nuovo Cimento Suppl. 3 (1965) 147.

[15] N. Cabibbo, and G. Parisi, "Exponential Hadronic Spectrum and Quark Liberation", Phys. Lett. 59B (1975) 67.

[16] L. McLerran, "The phase diagram of QCD and some issues of large N_C", Nucl. Phys. B, 195 (2009) 275.

[17] E.V. Shuryak, "Quantum chromodynamics and the theory of superdense matter", Phys. Rep. 61 (1980) 71.

[18] J. Adams et al. (STAR Collaboration), "Experimental and theoretical challenges in the search for the quark-gluon plasma: The STAR Collaboration's critical assessment of the evidence from RHIC collisions", Nuclear Physics A 757 (2005) 102.

[19] Y. Oganessian, "Introduction to heavy-ion physics ", National Research Nuclear University MEPHI, ISBN 978-5-7262-1033-9, 2008.

[20] C.-Y. Wong, "Introduction to high-energy heavy-ion collisions", World Scientific, 1994.

[21] A. Chodos et al., "A new extended model of hadrons", Phys. Rev. D9 (1974) 3471.

[22] T.D. Lee and G.C. Wick, "Vacuum stability and vacuum excitation in a spin-0 field theory", Phys. Rev. D 9 (1974) 2291.

[23] R.J. Glauber, "Quantum optics and heavy ion physics", Nucl. Phys. A774 (2006) 3.

[24] G. Xie and the STAR Collaboration, "Nuclear modification factor of D^0 meson in Au+Au collisions at $\sqrt{s}_{NN} = 200$ GeV", Nuclear Physics A, 956 (2016) 473.

[25] P. Koch, B. Muller, and J. Rafelski, "Strangeness in relativistic heavy ion collisions", Phys. Rep. 142 (1986) 167.

[26] B.I. Abelev et al. (STAR Collaboration), "Enhanced strange baryon production in Au+Au collisions compared to p+p at $\sqrt{s}_{NN} = 200$ GeV", Phys. Rev. C 77 (2008) 044908.

[27] F. Becattini, and J. Manninen, "Strangeness production from SPS to LHC", J. Phys. G 35 (2008) 104013.

[28] A. Wroblewski, "On the strange quark suppression factor in high-energy collisions", Acta Phys. Polon. B16 (1985) 379.

[29] B. Friman, C. Hohne, J. Knoll, S. Leupold, J. Randrup, R. Rapp and P. Senger (editors), "The CBM physics book: Compressed Baryonic Matter in Laboratory Experiments", Series: Lecture Notes in Physics, Vol. 814 1st Edition., 2011, 960 p.

[30] FAIR — Facility for Antiproton and Ion Research. Green Paper. The Modularized Start Version. GSI. October 2009.

[31] T. Galatyuk, "Future facilities for high μ_B physics", Nucl. Phys. A 982 (2019) 163, update (2021).

[32] Compressed Baryonic Matter Experiment, Technical Status Report, GSI, Darmstadt (2005).

[33] P. Senger, "The Compressed Baryonic Matter Experiment at FAIR", JPS Conf. Proc. 8 (2015) 022001.

[34] I.C. Arsene et al., "Dynamical phase trajectories for relativistic nuclear collisions", Phys. Rev. C 75 (2007) 034902.

[35] V.D. Toneev et al., "Strangeness production in nuclear matter and expansion dynamics", Eur. Phys. J. C 32 (2003) 399.

[36] S. Salur, "Investigation of Hadronic Resonances with STAR", Dissertation thesis, Yale university, Yale (2006).

[37] S.A. Bass, M. Belkacem, M. Bleicher et al., "Microscopic Models for Ultrarelativistic Heavy Ion Collisions", Prog. Part. Nucl. Phys. 41 (1998) 225.

[38] E.A. Matyushevskiy, P.G. Akishin, V.S. Alfeev et al., "SC dipole magnet for CBM", in *CBM Progress Report 2010*, GSI Darmstadt, ISBN: 978-3-9811298-8-5 (2011).

[39] A. Malakhov and A. Shabunov (editors), "Technical Design Report for the CBM Superconducting Dipole Magnet", GSI, Darmstadt, (2013).

[40] M. Deveaux, "Development of Fast and Radiation Hard Monolithic Active Pixel Sensors (MAPS) Optimized for Open Charm Meson Detection with the CBM Vertex Detector", Dissertation thesis, Goethe university, Frankfurt am Main (2017).

[41] C. Dritsa, "Design of the Micro Vertex Detector of the CBM experiment: Development of a detector response model and feasibility studies of open charm measurement", Dissertation thesis, Goethe university, Frankfurt am Main (2011).

[42] T. Tischler, "Mechanical Integration of the Micro Vertex Detector for the CBM experiment", Dissertation thesis, Goethe university, Frankfurt am Main (2015).

[43] E. Krebs, "Application of the CBM Micro Vertex Detector for Dielectron Analysis", Dissertation thesis, Goethe university, Frankfurt am Main (2016).

[44] J. Heuser, W. Müller, V. Pugach, P. Senger, C.J. Schmidt, C. Sturm and U. Frankenfeld (editors), "Technical Design Report for the CBM Silicon Tracking System (STS)", GSI, Darmstadt (2013).

[45] M. Singla, "The Silicon Tracking System of the CBM experiment at FAIR. Development of microstrip sensors and signal transmission lines for a low-mass, low-noise system", Dissertation thesis, Goethe university, Frankfurt am Main (2013).

[46] K.-H. Becker, K.-H. Kampert, J. Kopfer at al. (RICH working group), "Technical Design Report for the CBM Ring Imaging Cherenkov (RICH) Detector", GSI, Darmstadt (2013).

[47] J. M. Kopfer, "Development of a prototype camera and Monte Carlo studies for the optimisation of the CBM-RICH detector", Dissertation thesis, Bergische Universität Wuppertal (2014).

[48] S. Reinecke, "Characterisation of photon sensors for the CBM-RICH and its use for the reconstruction of neutral mesons via conversion", Dissertation thesis, Bergische Universität Wuppertal (2016).

[49] Y. Ryabov, "CBM RICH mechanical design", Talk given on the 27th CBM collaboration meeting in Darmstadt, 2016.

[50] A. Arend, "Optimization of a Transition Radiation Detector for the Compressed Baryonic Matter Experiment", Dissertation thesis, Goethe university, Frankfurt am Main (2014).

[51] N. Hermann (Editor), "Technical Design Report for the CBM Time-of-Flight (TOF) System", GSI, Darmstadt (2014).

[52] P.-A. Loizeau, "Development and Test of a Free-Streaming Readout Chain for the CBM Time of Flight Wall", Dissertation thesis, Ruperto-Carola university, Heidelberg (2014).

[53] A.L. Garcia, "Timing Resistive Plate Chambers with Ceramic Electrodes for Particle and Nuclear Physics Experiments", Dissertation thesis, Technical university, Dresden (2014).

[54] C. Grupen and B. Schwartz, “Particle Detectors”, 2nd edition, Cambridge University Press, 2008.

[55] I.E. Korolko, M.S. Prokudin and Yu.M. Zaitsev, “The CBM ECAL”, IOP Conf. Series: Journal of Physics: Conf. Series 798 (2017) 012164.

[56] S. Chattopadhyay, Y.P. Viyogi, P. Senger, W.F.J. Müller, and C.J. Schmidt (Editors), “Technical Design Report for the CBM Muon Chambers (MuCh)”, GSI, Darmstadt (2014).

[57] K.A. Olive et al. (Particle Data Group Collaboration), “Review of Particle Physics”, Chin. Phys. C 38 (2014) 090001.

[58] D.E. Groom, N.V. Mokhov, and S. Striganov, “Muon Stopping Power and Range Tables 10 MeV–100 TeV”, Atom. Data and Nucl. Data Tabl. 78 (2001) 183-356.

[59] J. Bielcik, T. Galatyuk, M. Golubeva et al., “Technical Design Report for the CBM Projectile Spectator Detector (PSD)”, GSI, Darmstadt (2015).

[60] R. Snellings, “Elliptic Flow: A Brief Review”, New J. Phys. 13 (2011) 055008.

[61] D. Hutter, “The CBM FLES Input Interface”, DPG Spring Meeting 2015, Heidelberg, 23-27 March 2015.

[62] F. Friese, “The high-rate data challenge: computing for the CBM experiment”, J. Phys.: Conf. Ser. 898 (2018) 112003.

[63] I. Kisel, I. Kulakov, and M. Zyzak, “Standalone First Level Event Selection Package for the CBM Experiment”, IEEE Trans. on Nucl. Science, 60, 5, (2013), 3703.

[64] V. Akishina, I. Kisel, P. Kisel, P. Senger, I. Vassiliev, and M. Zyzak, “Reconstruction of Particles Produced at Different Stages of Heavy Ion Collision in the CBM Experiment at FAIR”, Poster, Quark Matter 2017, 5-11 February 2017, Chicago, USA.

[65] M. Zyzak, “Online Selection of Short-Lived Particles on Many-Core Computer Architectures in the CBM Experiment at FAIR”, Dissertation thesis, Goethe university, Frankfurt am Main (2016).

[66] S. Gorbunov and I. Kisel, “Reconstruction of decayed particles based on the Kalman filter”, CBM-SOFT-note-2007-003, 7 May 2007.

[67] S. Gorbunov, “On-line reconstruction algorithms for the CBM and ALICE experiments”, Dissertation thesis, Goethe university, Frankfurt am Main (2012).

[68] V. Akishina, I. Kisel, "Online 4-Dimensional Reconstruction of Time-Slices in the CBM Experiment", IEEE Trans. on Nucl. Science, 62, 6, (2015), 3172.

[69] V. Akishina, "4D Event Reconstruction in the CBM Experiment", Dissertation thesis, Goethe university, Frankfurt am Main (2017).

[70] S. Gorbunov, U. Kebschull, I. Kisel, V. Lindenstruth and W.F.J. Müller, "Fast SIMDized Kalman filter based track fit", Comp. Phys. Comm., 178 (5), (2008) 374–383.

[71] S.A. Bass, M. Belkacem, M. Bleicher at al., "Microscopic Models for Ultrarelativistic Heavy Ion Collisions", Prog. Part. Nucl. Phys. 41 (1998) 225.

[72] M. Bleicher, E. Zabrodin, C. Spieles at al., "Relativistic Hadron-Hadron Collisions in the Ultra-Relativistic Quantum Molecular Dynamics Model", J. Phys. G: Nucl. Part. Phys. 25 (1999) 1859.

[73] W.H. Desmonde and K.J. Berkling, "The Zuse Z3. German predecessor of the Mark I", Konrad Zuse Internet Archive, Essay – ZIA ID: 0046, 1966.

[74] G.C. Chase, "History of Mechanical Computing Machinery", Ann. Hist. Comp., Vol. 2, No. 3, 1980, pp. 198–226.

[75] Von Neumann, J., "First Draft of a Report on the EDVAC", Moore School, University of Pennsylvania, 1945. Reprinted in IEEE Ann. Hist. Comp., No. 4, 1993.

[76] W. Stallings, "Computer Organization and Architecture: Designing for Performance", Pearson Education, 2016.

[77] G.E. Moore, "Cramming more components onto integrated circuits", Electronics, Vol. 38, No. 8, April 19, 1965

[78] M.J. Flynn, "Very high-speed computing systems", Proceedings of the IEEE, 54 (12), 1966, 1901–1909.

[79] J. Baechler et al. (NA35 Collaboration), "Production of charged kaons in central S+S and O+Au collisions at 200 GeV/nucleon", Nucl. Phys. A 544 (1992) 609.

[80] E. Epple, K. Lapidus,
https://www.ph.tum.de/academics/org/labs/fopra/docs/userguide-75.en.pdf

[81] M. Zyzak, I. Kisel, P. Kisel, and I. Vassiliev, "Reconstruction of short-lived particle spectra with KF Particle Finder", CBM Status Report, GSI, 2017.

[82] W. Florkowski, "Phenomenology of Ultra-Relativistic Heavy-Ion Collisions", World Scientific Pub. Co. Inc. (2010).

[83] K.H. Ackermann et al. (STAR Collaboration), "STAR detector overview", Nucl. Instr. Meth. A499 (2003) 624.

[84] M. Harrison, T. Ludlam, and S. Ozaki, "RHIC Project Overview", Nucl. Instr. and Meth. A 499 (2003) 235.

[85] STAR Collaboration, "Studying the Phase Diagram of QCD Matter at RHIC", 01 June 2014.
https://drupal.star.bnl.gov/STAR/files/BES_WPII_ver6.9_Cover.pdf

[86] G. Odyniec (for the STAR Collaboration), "Beam Energy Scan Program at RHIC (BES I and BES II) — Probing QCD Phase Diagram with Heavy-Ion Collisions", Proceedings, 18th Hellenic School and Workshops on Elementary Particle Physics and Gravity (CORFU2018) : Corfu, Greece, August 18-September 28, 2018,

[87] Y. Fisyak, I. Kisel, P. Kisel, P. Senger, I. Vassiliev, and M. Zyzak, "Missing mass method: development and proof of the approach with the STAR data", CBM Status Report, GSI, 2017.

[88] V. Lepeltier, Review on TPC's, "Journal of Physics: Conference Series", Vol. 65 , No. 1, 2007.

[89] M. Anderson et al., "The STAR time projection chamber: a unique tool for studying high multiplicity events at RHIC." Nucl. Instr. Meth. A 499, 2003, 659.

[90] M. Anderson et al., "A readout system for the STAR time projection chamber", Nucl. Instr. Meth. A 499, 2003, 679.

[91] W.J. Llope, et al. "The TOFp / pVPD time-of-flight system for STAR", Nucl. Instr. Meth. A522, 2004, 252.

[92] J.S. Lange et al., "The STAR level-3 trigger system", Nucl. Instrum. Meth. A 453, 2000, 397.

[93] F.S. Bieser et al., "The STAR trigger", Nucl. Instrum. Meth. A 499, 2003, 766.

[94] E.G. Judd et al., "The evolution of the STAR Trigger System", Nucl. Instr. Meth. A 902, 2018, 228.

[95] P. Yepes, "A fast track pattern recognition", Nucl. Instrum. Meth. A 380, 1996, 582.

[96] A. Tang, “HLT and CA Tracker”, CBM–STAR Joint Workshop, CCNU Wuhan, September 23, 2017.

[97] I. Kisel, A. Belousov, Y. Fisyak, H. Ke, P. Kisel, G. Kozlov, S. Margetis, A. Tang, I. Vassiliev, and M. Zyzak, “TFG/HLT Report”, STAR Collaboration Meeting, Cracow, Poland, August 22, 2019.

[98] M. Shao, O. Y. Barannikova, X. Dong, Y. Fisyak, L. Ruan, P. Sorensen and Z. Xu, “Extensive particle identification with TPC and TOF at the STAR experiment”, Nucl. Instr. Meth. A 558, 2006, 419.

[99] The STAR TOF Collaboration, Proposal for a large area time of flight system for STAR, (2004).

[100] L. Adamczyk et al. “Bulk properties of the medium produced in relativistic heavy-ion collisions from the beam energy scan program”, Phys. Rev. C 96, 2017, 044904.

[101] https://www.flickr.com/photos/brookhavenlab/sets/72157613690851651, https://www.star.bnl.gov/public/tpc/tpc.html.

[102] F. Bergsma et al., “The STAR detector magnet subsystem”, Nucl. Instr. Meth. A 499, 2003, 633.

[103] STAR Collaboration, “Technical Design Report for the iTPC Upgrade”, 2015.

[104] STAR Collaboration, “Physics Program for the STAR/CBM eTOF Upgrade”, 2017.

The following papers have been published on the topic of this dissertation:

[A1] T. Ablyazimov, A. Abuhoza, R.P. Adak, ..., P. Kisel et al., “Challenges in QCD matter physics — The scientific programme of the Compressed Baryonic Matter experiment at FAIR”, Eur. Phys. J. A (2017) 53:60.

[A2] I.S. Kulakov, S.A. Baginyan, V.V. Ivanov, and P.I. Kisel, “Performance Analysis of a Cellular Automaton Algorithm to Solve the Track-Reconstruction Problem on a Multicore Server at the Laboratory of Information Technologies, Joint Institute of Nuclear Research”, Physics of Particles and Nuclei Letters, 2013, Vol. 10, No. 2, pp. 162–170.

[A3] T.O. Ablyazimov, M.V. Zyzak, V.V. Ivanov and P.I. Kisel, “Fast Parallelized Kalman Filter Based Reconstruction of Charged Particle Trajectories for the Compressed Baryonic Matter Experiment on a Many-Core

Server at the Laboratory of Information Technologies, JINR", Physics of Particles and Nuclei Letters, 2014, Vol. 11, No. 4, pp. 537–548.

[A4] T.O. Ablyazimov, M.V. Zyzak, V.V. Ivanov, and P.I. Kisel, "Kalman Filter-Based Fast Track Reconstruction for Charged Particles in a Compressed Baryonic Matter Experiment Using Parallel Computing on a Multicore Server at the Laboratory of Information Technologies, Joint Institute for Nuclear Research", Physics of Particles and Nuclei Letters, 2015, Vol. 12, No. 3, 423–427.

[A5] T.O. Ablyazimov, M.V. Zyzak, V.V. Ivanov, and P.I. Kisel, "The Kalman filter method for the reconstruction of charged particle trajectories in the CBM experiment and its parallel implementation on the LIT JINR multicore server," Bulletin of the Peoples' Friendship University of Russia, Series Mathematics, Informatics, Physics, N2, 2014, pp. 191–196.

[A6] I.S. Kulakov, S.A. Baginyan, V.V. Ivanov, P.I. Kisel, "Analysis of the efficiency and performance of the track recognition algorithm in the STS detector of the CBM experiment on the multicore server of the JINR LIT", JINR Communication, P10-2012-1, Dubna, 2012.

[A7] T.O. Ablyazimov, M.V. Zyzak, V.V. Ivanov, P.I. Kisel, "The Kalman filter method for the reconstruction of charged particle trajectories in the CBM experiment and its parallel implementation on the LIT JINR multicore server", JINR Communication, P11-2013-118, Dubna, 2013.

[A8] D.V. Belyakov, V.V. Ivanov, P.I. Kisel, and M.V. Zyzak, "Performance of the track parameter reconstruction algorithm on AMD Radeon HD 7970 GHz edition GPUs", CBM Progress Report 2013, p. 102.

[A9] I. Kisel, P. Kisel, P. Senger, I. Vassiliev, and M. Zyzak, "Σ^+ and Σ^- reconstruction by the missing mass method", CBM Progress Report 2015, p. 130.

[A10] I. Kisel, P. Kisel, P. Senger, I. Vassiliev, and M. Zyzak, "Σ^+ and Σ^- reconstruction by the missing mass method", CBM Progress Report 2016, p. 176.

[A11] Y. Fisyak, I. Kisel, P. Kisel, P. Senger, I. Vassiliev, and M. Zyzak, "Applying the missing mass method to the STAR at RHIC data", CBM Progress Report 2017, p. 197.

[A12] M. Zyzak, I. Kisel, P. Kisel, and I. Vassiliev, "Reconstruction of short-lived particles with the KF Particle Finder", CBM Progress Report 2017, p. 151.

[A13] M. Zyzak, I. Kisel, P. Kisel, and I. Vassiliev, "KF Particle Finder as a tool for control of the systematic errors", CBM Progress Report 2018, p. 157.

[A14] I. Kisel, P. Kisel, P. Senger, I. Vassiliev and M. Zyzak, "Recent development in the missing mass method", CBM Progress Report 2018, p. 158.

[A15] Y. Fisyak, V. Ivanov, H. Ke, I. Kisel, P. Kisel, G. Kozlov, A. Tang, and I. Vassiliev, "Application of the Missing Mass Method in STAR BES-II fixed target program", CBM Progress Report 2020, p. 223.

[A16] V.P. Ladygin, T.O. Ablyazimov, P.G. Akishin, ..., P. Kisel et al., "Investigation of the compressed baryonic matter at the GSI accelerator complex", EPJ Web of Conferences 138, 01020 (2017).

[A17] P. Kisel, I. Kisel, P. Senger, I. Vassiliev, and M. Zyzak, "Strange Particle Reconstruction by the Missing Mass Method", EPJ Web of Conferences 173, 04009 (2018).

[A18] Y. Fisyak, V. Ivanov, H. Ke, I. Kisel, P. Kisel, G. Kozlov, S. Margelis, A. Tang, I. Vassiliev, "Missing mass method for short-lived particle reconstruction in the CBM and STAR experiments", Proceedings of the 9th International Conference "Distributed Computing and Grid Technologies in Science and Education" (GRID'2021), Dubna, Russia, July 5-9, 473, (2021).

[A19] Y. Fisyak, V. Ivanov, H. Ke, I. Kisel, P. Kisel, G. Kozlov, S. Margelis, A. Tang, I. Vassiliev, M. Zyzak, "Application of the missing mass method in the fixed-target program of the STAR experiment", EPJ Web of Conferences 251, 04029 (2021).

Zusammenfassung

Relevanz der Dissertationsarbeit

In der vorliegenden Dissertation wurde die Missing-Mass-Methode zur Rekonstruktion von kurzlebigen Teilchen mit neutralen Teilchen in ihren Zerfallsprodukten und ihre Umsetzung in Form von schnellen Algorithmen für die praktische Anwendung in Schwerionenphysikexperimenten entwickelt. Die mathematischen Prozeduren, die die Methode implementieren, wurden zunächst in dem Softwarepaket FLES (First Level Event Selection) für das zukünftige CBM-Experiment (FAIR) entwickelt, implementiert und anschließend für die Verarbeitung und Analyse von realen Daten im STAR-Experiment (BNL) angepasst und angewendet.

Das Hauptziel moderner großer Experimente mit schweren Ionen wie CBM (FAIR), STAR (BNL) und ALICE (CERN) ist eine detaillierte Untersuchung des Phasendiagramms der Quantenchromodynamik (QCD) im Quark-Gluon-Plasma (QGP), der Zustandsgleichung der Materie bei extrem hohen Baryonendichten und des Übergangs von der hadronischen Phase der Materie zum Quark-Gluon-Zustand.

Das derzeit bekannteste theoretische Modell der Elementarteilchen ist das Standardmodell (SM) der Teilchen und Wechselwirkungen, das auf den Grundsätzen der Invarianz der lokalen Kalibrierung basiert, also der Invarianz der Bewegungsgleichungen gegenüber beliebigen Änderungen der Raumzeitkoordinaten.

Das Standardmodell postuliert die Existenz von 12 fundamentalen Elementarteilchen mit Spin 1/2. Diese Liste umfasst die folgenden Fermionen: 6 Leptonen (Elektron e^-, Myon μ^-, Tau-Lepton τ^-, Elektron-Neutrino ν_e, Myon-Neutrino ν_μ und Tau-Neutrino ν_τ) und 6 Quarks (u, d, s, c, b, t). Jedes dieser Fermionen hat ein entsprechendes Antiteilchen.

Quarks haben eine so genannte Farbladung, die ihre Beteiligung an der starken Wechselwirkung bestimmt. Durch das Tragen von elektrischer Ladung und Isospin können sie mit anderen Fermionen elektromagnetisch bzw. schwach wechselwirken.

Quarks sind Fermionen und haben den Spin 1/2; Gluonen sind Bosonen mit Spin 1. Quarks werden nach zwei Eigenschaften klassifiziert: Flavor und Farbe. Es werden insgesamt 6 Quark-Flavors und 3 Farben unterschieden. Flavor ist eine Eigenschaft, die durch starke Wechselwirkungen erhalten bleibt. Das Gluon zeichnet sich durch eine Doppelfarbe aus — Farbe und Antifarbe, und alle anderen Quantenzahlen sind Null. Wenn ein Gluon emittiert wird, ändert das Quark seine Farbe, aber nicht seinen Flavor. Im Standardmodell gibt es insgesamt 8 Arten von Gluonen. Bei normaler Kerndichte und Temperatur sind Quarks zusammen mit Gluonen in Hadronen gebunden. Zustände mit drei Quarks nennt man Baryonen (z.B. Proton $|p\rangle = |uud\rangle$ und Neutron $|n\rangle = |udd\rangle$), Mesonen bestehen aus Quark und Antiquark (z.B. Pion $|\pi^-\rangle = |d\bar{u}\rangle$ und Kaon $|K^-\rangle = |s\bar{u}\rangle$).

Es gibt Anziehungskräfte zwischen Quarks, die zwei Eigenschaften haben: asymptotische Freiheit bei sehr kleinen Distanzen und Confinement, da die potenzielle Energie der Wechselwirkung mit zunehmender Distanz zwischen den Quarks ins Unendliche steigt. Bei schweren relativistischen Ionenkollisionen können jedoch Bedingungen entstehen, bei denen die QCD-Materie ihre Confinement-Eigenschaften verliert und Quarks und Gluonen die Fähigkeit erhalten, sich über Distanzen von mehr als 1 fm zu bewegen.

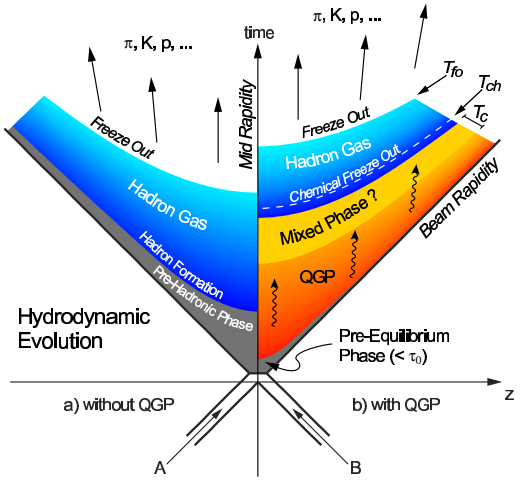

Abbildung 8.1: Schematische Darstellung der Entwicklungsstadien der Kernmaterie in der Raumzeit (bei niedrigen Energien wird die QGP-Phase nicht erzeugt).

Die Entwicklung zentraler Kollisionen schwerer Kerne in der Raumzeit bei RHIC- oder LHC-Energien sieht wie folgt aus (Abb. 8.1). Zu Beginn der Nukleon-Nukleon-Kollisionen zweier Kerne wechselwirken Partonen (Quarks und Gluonen), was zu einer massiven Produktion von Quarks, Antiquarks und Gluonen führt. Es wird angenommen, dass mehrere Parton-Parton-Wechselwirkungen zur Herstellung eines lokalen thermodynamischen Equilibriums im Quark-Gluon-System bei der Temperatur T_i führen können. Liegt die Anfangstemperatur über der kritischen Phasenübergangstemperatur ($T_i > T_C$), so befindet sich das System in einem Zustand des Quark-Gluon-Plasmas. Dann expandiert das QGP, die Temperatur sinkt, und erreicht die kritische Temperatur T_C. Bei einem

Phasenübergang erster Ordnung befindet sich die Kernmaterie für einige Zeit in einem gemischten Phasenzustand, der Quarks, Antiquarks, Gluonen und Hadronen vereint. In diesem Zustand wandeln sich die Freiheitsgrade der Quarks in hadronische Freiheitsgrade um, bis es zu einem chemischen Freezeout kommt. Infolgedessen expandiert das System weiter und zerfällt nach Erreichen des kinetischen Freezeouts in nicht wechselwirkende Teilchen, die dann im Detektorsystem registriert werden.

Soft-Hadronen, also Hadronen mit relativ geringem Transversalimpuls in Bezug auf die Kollisionsachse, machen über 90 % der erzeugten Teilchen aus und liefern Informationen über die Eigenschaften des QGP.

Schwere Quarks, das heißt Strange-, Charm- und Beauty-Quarks, werden hauptsächlich durch Gluonenfusion in inelastischen Streuprozessen in der Anfangsphase erzeugt und existieren während der gesamten Systementwicklung. Sie sind daher empfindliche Proben zur Untersuchung der Eigenschaften des stark wechselwirkenden Materiemediums, das bei Schwerionenkollisionen entsteht.

Aus der Tatsache, dass kollidierende Kerne nur aus u- und d-Quarks bestehen, können wir schließen, dass alle experimentell beobachteten Strange-Quarks oder Antiquarks bei Kollisionen entstehen. Die Analyse der Entstehung von Strangeness ermöglicht es uns also, die Bedingungen und die Dynamik von QGP besser zu verstehen. Dies erklärt den Schwerpunkt dieser Arbeit auf der Entwicklung effizienter Methoden zur Suche und Rekonstruktion von Strange-Teilchen.

Das CBM-Experiment (FAIR)

Die Anlage für Antiprotonen- und Ionenforschung (FAIR, Facility for Antiproton and Ion Research) dient der Untersuchung der Struktur und der grundlegenden Eigenschaften der Materie. In der FAIR-Beschleunigungsanlage der neuen Generation werden Forschungsarbeiten in verschiedenen Bereichen der Physik durchgeführt: Kerne, Hadronen, Teilchen, Atome, Antimaterie, kondensierte Materie sowie Plasmen hoher Dichte.

Eines der Experimente im FAIR-Beschleunigungskomplex wird das CBM-Experiment (Compressed Baryonic Matter) sein. Es wird bei Energien von 2–11 GeV/n auf dem SIS100-Synchrotron und 11–35 GeV/n auf dem SIS300-Synchrotron arbeiten.

Das Schwerionenexperiment CBM wird die höchsten baryonischen Dichten erzeugen und die Eigenschaften von superdichter Kernmaterie unter verschiedenen extremen Bedingungen untersuchen, wie z.B. den Zustand der Materie im Zentrum von Neutronensternen im letzten Entwicklungsstadium vor der Umwandlung in ein Schwarzes Loch. Das CBM-Experiment wird das experimentelle Schwerionen-Programm von ALICE (CERN) und STAR (BNL) ergänzen, mit dem die Eigen-

schaften heißer Materie untersucht werden sollen, wie sie kurz nach dem Urknall existierte.

Um die Eigenschaften der superdichten Kernmaterie mit noch nie erreichter Genauigkeit untersuchen zu können, muss der CBM-Detektor mit sehr hohen Kollisionsraten arbeiten (bis zu 10^7 Kollisionen pro Sekunde), die um mehrere Größenordnungen höher sind als bei derzeitigen und künftigen Experimenten mit schweren Ionen und extreme Anforderungen an die Detektoren, die Ausleseelektronik und die Datenverarbeitungsalgorithmen stellen.

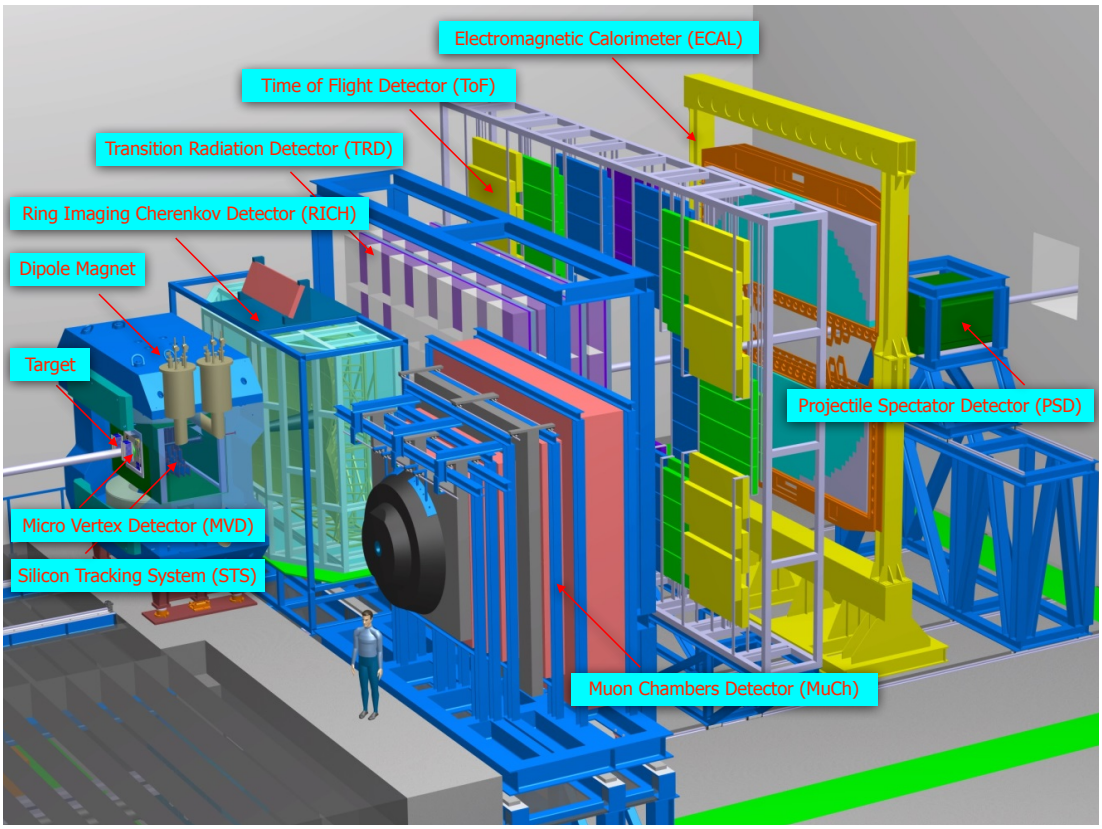

Abbildung 8.2: Der CBM-Aufbau: Target, supraleitender Dipolmagnet, Mikro-Vertex-Detektor (MVD), Silizium-Tracking-System (STS), Cherenkov-Strahlungs-Detektor (RICH), Übergangs-Strahlungs-Detektor (TRD), Flugzeit-Detektor (TOF), elektromagnetisches Kalorimeter (ECAL), Myonen-Detektor (MuCh), Vorwärts-Hadronen-Fragment-Kalorimeter (PSD).

Der CBM-Aufbau wird in Abb. 8.2 im Detail dargestellt. Für die Untersuchung von Elektronen- und Myonenpaaren wird der CBM-Detektor in zwei verschiedenen Konfigurationen betrieben: eine Elektronenkonfiguration mit dem RICH-Detektor zur Messung von Elektronenpaaren und eine Myonenkonfiguration mit dem MuCh-Detektor zur Messung von Myonenpaaren. Die beiden Konfigurationen werden jährlich ausgetauscht.

Das FLES (First Level Event Selection) Paket von Algorithmen im CBM-Experiment ist darauf konzipiert, die Topologie von Ereignissen vollständig zu rekonstruieren und sie in Echtzeit zu selektieren. Es dient der Suche nach Teilchentrajektorien, der Berechnung ihrer Parameter, der Identifizierung von Teilchen und der Bestimmung von Ereignissen, die für die Physik von Bedeutung sind. Als Eingabedaten verwendet das FLES-Paket die Geometrie der Tracking-Detektoren und die registrierten Koordinaten der Kreuzungspunkte von geladenen Teilchen mit den Detektorstationen (Hits). Die Trajektorien stabiler und langlebiger geladener Teilchen werden mit einem Algorithmus rekonstruiert, der auf einem zellulären Automaten (CA, Cellular Automaton) basiert. Die auf dem Kalman-Filter (KF) basierende Methode wird zur genauen Schätzung der Parameter der Teilchentrajektorien und ihrer Ungenauigkeiten verwendet. Kurzlebige Teilchen, die meist zerfallen, bevor sie die ersten Tracking-Stationen erreichen, werden mit Hilfe der Teilchen aus ihren Zerfällen (den sogenannten Tochterteilchen) rekonstruiert, die im Detektorsystem registriert und dann rekonstruiert werden.

KF Particle und KF Particle Finder Pakete

Teilchen mit sehr kurzen Lebensdauern und Resonanzen können meist nicht direkt in Detektoren registriert werden, da sie die ersten Detektorstationen nicht erreichen. Diese Teilchen können mit Hilfe ihrer Zerfallsprodukte rekonstruiert werden, die normalerweise eine ausreichende Lebensdauer haben, um im Detektorsystem registriert zu werden.

KF Particle ist ein Softwarepaket zur Rekonstruktion kurzlebiger Teilchen mit Hilfe eines Kalman-Filters (KF), das ursprünglich für CBM entwickelt wurde. Das Paket behandelt sowohl Tochter- als auch Mutterteilchen mit denselben Parametern und verarbeitet sie auf genau dieselbe Weise, so dass auch die Rekonstruktion von Zerfallsketten intuitiv und einfach wird. Das Paket ist nicht von der Geometrie des Detektorsystems abhängig und kann auch in anderen Experimenten verwendet werden.

Das KF Particle-Paket definiert den Zustandsvektor von Teilchen mit acht Parametern bestehend aus: drei Koordinaten des Teilchens (x, y, z), drei Impulskomponenten (p_x, p_y, p_z), Energie (E) und, wenn der Erzeugungspunkt bekannt ist, das Zeitintervall zwischen seiner Erzeugung und seinem Zerfall, das als Abstand geteilt durch den Impuls ($s = l/p$) gemessen wird:

$$\mathbf{r} = \{x, y, z, p_x, p_y, p_z, E, s\}. \tag{8.1}$$

Die Kovarianzmatrix der Fehler wird zusammen mit der Schätzung des Zustandsvektors berechnet, was es ermöglicht, die Genauigkeit der geschätzten Pa-

rameter zu bestimmen und den Wert χ^2 zu berechnen, der die Qualität der Teilchenrekonstruktion charakterisiert.

Das KF Particle-Paket verfügt über eine breite Palette von Funktionen, wie zum Beispiel: die Konstruktion von Mutterteilchen aus Tochterteilchen; die Bestimmung der Parameter jedes Teilchens an jedem Punkt seiner Trajektorie; die Berechnung der Entfernung zu einem anderen Teilchen oder zu einem Zerfallspunkt in χ^2-Einheiten; die Anwendung von Einschränkungen im Zustandsvektor auf die Masse oder die Produktionskoordinate des Mutterteilchens. Darüber hinaus bietet KF Particle einen einfachen und intuitiven Zugang zu den physikalischen Parametern der rekonstruierten Teilchen, wie Masse, Impuls, Zerfallslänge, Lebensdauer und Rapidität, sowie deren Fehler für weitere mathematisch genaue physikalische Analysen.

Das Paket KF Particle Finder wurde entwickelt, um die meisten Signalteilchen aus dem Physikprogramm des CBM-Experiments zu rekonstruieren, darunter Strange-Teilchen, Strange-Resonanzen, Hypernuklei, leichte Vektor-Mesonen, Charm-Teilchen und Charmonium. Das Paket umfasst die Suche nach über hundert Zerfällen von kurzlebigen Teilchen. Dies macht den KF Particle Finder zu einer universellen Plattform für die Rekonstruktion kurzlebiger Teilchen und die physikalische Analyse sowohl online als auch offline.

Der KF Particle Finder unterteilt zunächst alle Teilchen in zwei Gruppen: primäre und sekundäre. Primäre Teilchen sind solche, die durch Kollisionen schwerer Ionen entstehen. Ihre rekonstruierten Trajektorien müssen innerhalb der Fehler der Spurparameter auf den bereits gefundenen primären Kollisionspunkt (Primary Vertex) zeigen.

Die Sekundärteilchen (Tochterteilchen) werden dann entsprechend ihrer PID-Hypothese und ihrer Zerfallskanäle zu Kandidaten für Mutterteilchen zusammengefasst. Es werden zunächst Zwei-Teilchen-Zerfälle betrachtet, wobei die Kandidaten für die Mutterteilchen aus einer positiven und einer negativen Sekundärspur gebildet werden. Primärteilchen, die unmittelbar am primären Kollisionspunkt zerfallen, einschließlich Resonanzen, leichte Vektor-Mesonen und Charmonium, werden durch Kombination von zwei Primärspuren, einer positiven und einer negativen, rekonstruiert.

Zur Rekonstruktion von Zerfallsketten, die beispielsweise bei Zerfällen von Multi-Strange-Hyperonen (z.B. Ξ^- und Ω^-) auftreten, werden bereits rekonstruierte sekundäre Λ und $\bar{\Lambda}$ verwendet, die dann als Tochterteilchen für die weitere Analyse ähnlich wie oben beschrieben behandelt werden.

Da kollidierende Kerne nur aus u- und d-Quarks bestehen, werden die s- und $\bar{s}$ Strange-Quarks direkt bei Schwerionenkollisionen erzeugt und haben eine relativ geringe Masse von 95 MeV/c^2. Dies trägt dazu bei, dass sie in großen Mengen produziert werden. Theoretischen Vorhersagen zufolge könnte die erhöhte

Produktion von Strangeness ein Indikator für QGP sein. Strange- und Multi-Strange-Hyperonen können auch in nachfolgenden Kollisionen innerhalb des QGP erzeugt werden und somit sensitiv für die Eigenschaften des Mediums im kollidierenden System sein. Es wird erwartet, dass diese Sensitivität zunimmt, wenn die Strahlenergie näher an oder sogar unter die Erzeugungsgrenze sinkt. Daher eignen sich Strange- und Multi-Strange-Teilchen gut für die Untersuchung von heißer und dichter baryonischer Materie.

Die Missing-Mass-Methode

Die Missing-Mass-Methode (missing mass method) wurde für die Rekonstruktion von Zerfällen kurzlebiger geladener Teilchen vorgeschlagen, wenn eines der Tochterteilchen neutral ist und im Detektorsystem nicht registriert wird. Die Methode basiert auf den Gesetzen der Energie- und Impulserhaltung.

Wie die Methode der fehlenden Masse funktioniert, wird anhand des Beispiels eines Zerfalls veranschaulicht:

$$\Sigma^- \rightarrow n\pi^-. \tag{8.2}$$

Bei diesem Zerfall (Abb. 8.3, links) wird das Tochter-Pion im Tracking-Detektor registriert und in einem der PID-Detektoren identifiziert, während das Neutron als neutrales Teilchen nicht im Detektorsystem registriert wird. Allerdings hat Σ^- zwar eine kurze Lebensdauer von $c\tau_{\Sigma^-} = 4,4$ cm, aber bei Experimenten mit fixiertem Ziel (fixed target) kann die durchschnittliche Länge der Trajektorie im Laborkoordinatensystem aufgrund des relativistischen Boosts 15–20 cm erreichen. In diesem Fall ist Σ^- in der Lage, mehrere Tracking-Stationen zu durchqueren, um registriert und dann rekonstruiert zu werden. Daher ist es bei diesem Zerfall möglich, die Trajektorien beider geladener Teilchen zu rekonstruieren, aber Σ^- kann im Gegensatz zu π^- noch nicht identifiziert werden, da es die PID-Detektoren nicht erreicht.

Die Rekonstruktion eines kurzlebigen geladenen Teilchens mit Hilfe der Missing-Mass-Methode erfolgt in drei Schritten (Abb. 8.3):

1. Rekonstruktion der Trajektorien des geladenen Mutterteilchens Σ^- und seines geladenen Tochterteilchens π^- im Tracking-System;
2. Rekonstruktion der Parameter des neutralen Tochterteilchens n auf der Grundlage der Parameter des Mutterteilchens Σ^- und des geladenen Tochterteilchens π^-;
3. Rekonstruktion des Massenspektrums von Σ^- unter Verwendung der Parameter der n- und π^--Tochterteilchen.

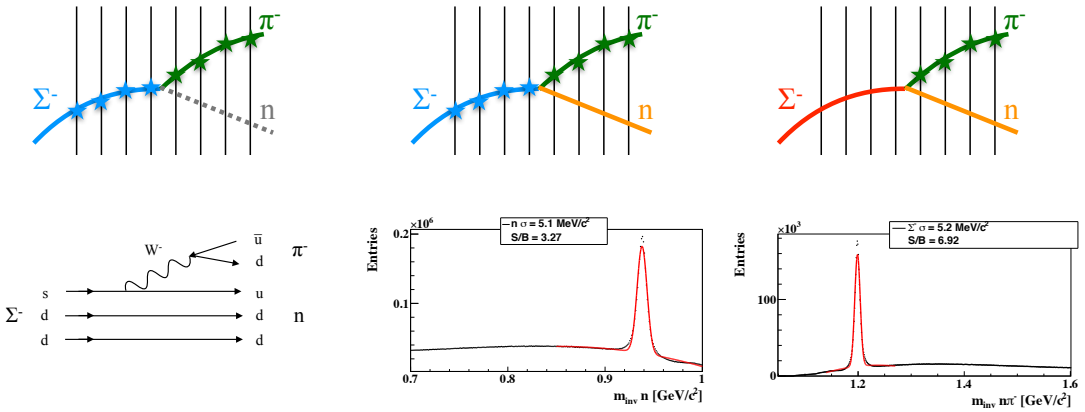

Abbildung 8.3: Drei Schritte bei der Umsetzung der Missing-Mass-Methode im CBM-Experiment: (1) Rekonstruktion der Trajektorien der geladenen Teilchen Σ^- und π^-; (2) Rekonstruktion des neutralen Teilchens n; (3) endgültige Rekonstruktion des Σ^- Mutterteilchens.

Die Missing-Mass-Methode ist technisch so organisiert, dass Primärteilchen als Kandidaten für Mutterteilchen bei der Suche nach Zerfällen mit einem neutralen Tochterteilchen ohne PID-Information verwendet werden, sie wird aus der Annahme des gesuchten Zerfalls hinzugefügt, und die Sekundärteilchen erhalten ihren Typ aus ihren Messungen in den PID-Detektoren. Wenn ein sekundäres Teilchen aus irgendeinem Grund nicht identifiziert wurde, wird es als Pion behandelt, das häufigste Teilchen, das bei Schwerionenkollisionen entsteht. Die Methode kombiniert alle Primärteilchen mit den entsprechenden Sekundärteilchen, je nach der aktuellen Hypothese des gesuchten Zerfalls, zum Beispiel mit allen π^- im Fall von Σ^- oder mit allen K^- im Fall von Ω^-.

Die Missing-Mass-Methode ist als Erweiterung des KF Particle Finder Pakets implementiert, das derzeit aktiv zur Suche und Rekonstruktion kurzlebiger Teilchen, sowohl online als auch offline, in großen Schwerionenexperimenten wie CBM (FAIR), ALICE (CERN) und STAR (BNL) verwendet wird.

Als Teil der Implementierung der Missing-Mass-Methode wurde eine Suche nach 18 Zerfällen mit einem neutralen Tochterteilchen zum KF Particle Finder Paket hinzugefügt (Abb. 8.4).

In der Anfangsphase der Methodenentwicklung war es wichtig, die Anwendbarkeit der Missing-Mass-Methode im CBM-Experiment zu beweisen. Dies geschah am Beispiel der Rekonstruktion eines neutralen Tochterteilchens, was mit den bereits vorhandenen und getesteten Funktionen des KF Particle-Pakets technisch möglich war. Zu diesem Zweck wurden Massenverteilungen eines neutralen Teilchens konstruiert, um die Leistung des Algorithmus direkt zu bestätigen. In diesem Stadium waren sofort deutliche Masse-Peaks von neutralen Teilchen sichtbar. Die logische weitere Vorgehensweise bestand darin, die Param-

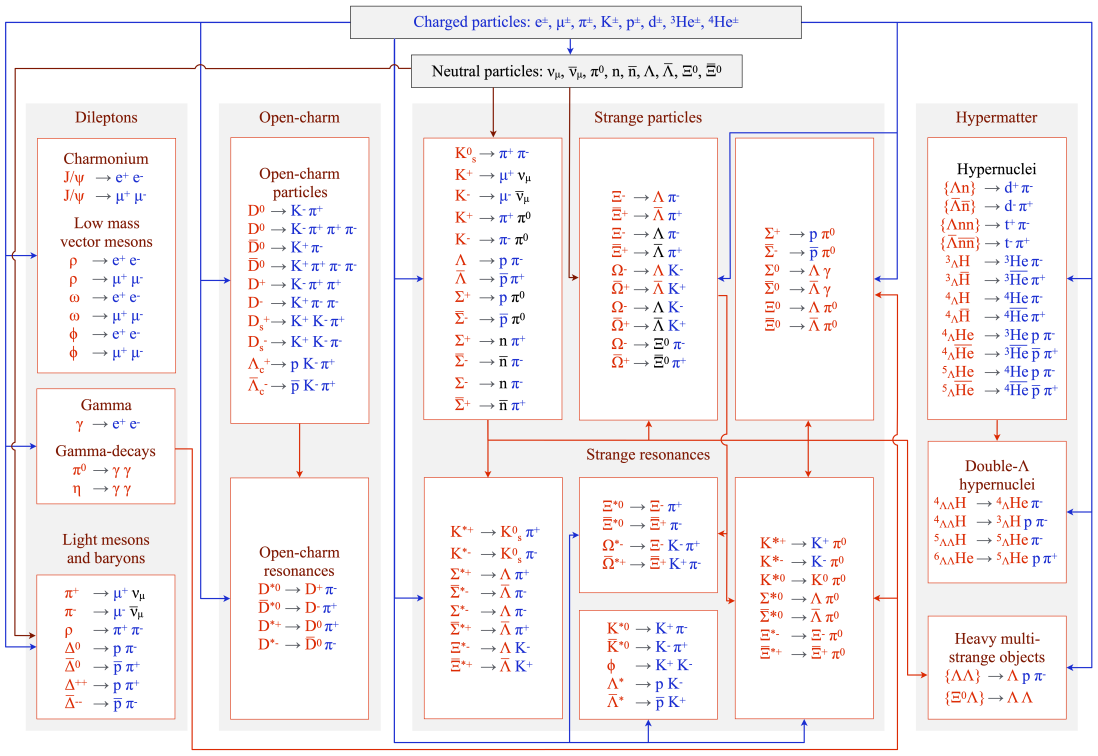

Abbildung 8.4: Blockdiagramm des KF Particle Finder Pakets mit implementierter Missing-Mass-Methode zur Suche nach Zerfällen kurzlebiger Teilchen mit einem neutralen Teilchen im Tochterkanal (schwarz dargestellt).

eter der Mutterteilchen aus den bereits vorhandenen Parametern der geladenen Tochterteilchen und der soeben berechneten neutralen Teilchen zu berechnen, so dass man auf diese Weise bei jedem Schritt die Arbeitsleistung der Methode überprüfen kann.

Der Zustandsvektor des neutralen Teilchens, als neue Messung, wurde mit dem bereits bekannten Zustandsvektor des sekundären geladenen Teilchens addiert, um die Parameter des Mutterteilchens zu bestimmen. Bei diesem Ansatz wurden die gefundenen Parameter des neutralen Teilchens mit den Eingangsparametern des geladenen Tochterteilchens addiert, mit deren Hilfe sie zuvor selbst berechnet wurden. Da ein solcher Additionsvorgang automatisch die Bestimmung des Zerfallspunktes beinhaltet, wurde der Zerfallspunkt ein zweites Mal berechnet. Bei diesem Ansatz wurde also einmal die Mutterspur, aber zweimal die Spur des geladenen Tochterteilchens einbezogen, was mathematisch nicht korrekt ist. Dennoch wurde dieser Ansatz in der Anfangsphase gewählt, da die Zeit für die Entwicklung der Methode knapp war und die Methode schrittweise entwickelt werden musste, wobei die Parameter der neutralen Teilchen als wichtiges Zwischenergebnis ermittelt werden mussten, um die Anwendbarkeit der Methode im CBM-Experiment zu überprüfen.

Infolgedessen hat die Missing-Mass-Methode bereits in der Anfangsphase ihrer Entwicklung gute Ergebnisse gezeigt (Abb. 8.5, links), obwohl sie einige Nachteile bei der Umsetzung aufwies, wie z.B. das Vorhandensein exzessiver zusätzlicher Berechnungen und die nicht ganz mathematisch korrekte Bestimmung des Zerfallspunktes kurzlebiger Teilchen.

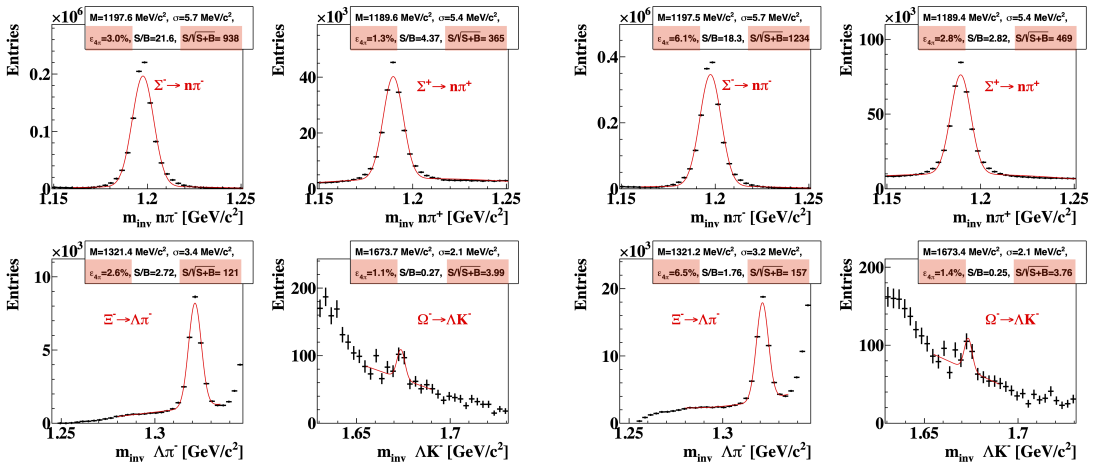

Abbildung 8.5: Mit der Missing-Mass-Methode rekonstruierte Massenverteilungen von Strange-Teilchen für 5 M simulierte zentrale AuAu-Kollisionen im UrQMD-Modell bei 10 GeV/n Energie im CBM-Experiment (links: Ergebnisse der ersten Implementierung, rechts: die verbesserte Implementierung der Methode). Die mathematisch genauere Implementierung der Missing-Mass-Methode erhöhte die Rekonstruktionsleistung um den Faktor 2 und die Signifikanz der Signaldaten um 25–30%.

Tabelle 8.1: Vergleich der 4π-Effizienz in der ersten und der verbesserten Version

Version	$\Sigma^- \to n\pi^-$	$\Sigma^+ \to n\pi^+$	$\Xi^- \to \Lambda\pi^-$	$\Omega^+ \to \Lambda K^-$
Erste	3.0%	1.3%	2.6%	1.1%
Verbesserte	6.1%	2.8%	6.5%	1.4%
Faktor	2.03	2.15	2.50	1.27

Nach intensiver Beschäftigung mit der Methode wurden zahlreiche Verbesserungen an der ersten Implementierung vorgenommen. So wird bei der geänderten Implementierung der Methode die Position des Zerfallspunktes des geladenen Mutterteilchens sofort durch zweistufige Extrapolation bestimmt und erfordert keine weitere Korrektur und Neuberechnung, was mathematisch exakt ist.

Der mathematische Teil der Umsetzung der Methode wurde ebenfalls erheblich verbessert, wobei ein genauerer und schnellerer Algorithmus verwendet wurde. Insbesondere werden alle grundlegenden Berechnungen jetzt mit 6×6-Matrizen

anstelle der früheren 7×7-Matrizen durchgeführt, da der Energieparameter aus dem Zustandsvektor und der Kovarianzmatrix entfernt wurde. Die Energie- und Massenberechnungen werden nun im letzten Schritt getrennt durchgeführt, und die Parameter aller kurzlebigen Teilchen werden in einer Iteration der Subtraktion des Kalman-Filters berechnet, statt wie in der ersten Version in zwei Iterationen (Subtraktion und Addition). Damit entfällt auch die Notwendigkeit einer sehr ressourcenintensiven Massenbeschränkungsmethode, die die Teilchenparameter in einem bestimmten Stadium der Berechnung ausgleicht, was zusätzliche Ungenauigkeiten mit sich bringt und den Berechnungsprozess stark verlangsamt.

Eine solche mathematisch genauere Implementierung der Methode der fehlenden Masse verbesserte die Qualität der Rekonstruktion von kurzlebigen Teilchen erheblich, was zu einer zweifachen Steigerung ihrer Rekonstruktionsleistung und einer Erhöhung der Signifikanz der Signaldaten um 25–30% führte. Ein Vergleich zweier Versionen der Implementierung der Missing-Mass-Methode im CBM-Experiment unter Verwendung von Daten des TOF-Flugzeitdetektors ist in Abb. 8.5 und Tab. 8.1 dargestellt.

Wie alle anderen Algorithmen in den Paketen KF Particle und KF Particle Finder ist auch die Missing-Mass-Methode unter extensiver Verwendung von Vektorbefehlen (SIMD) implementiert und für den parallelen Betrieb auf modernen Hochleistungsrechnersystemen mit vielen Kernen optimiert, die sowohl Prozessoren als auch Koprozessoren enthalten können. Eine Reihe von Algorithmen, die die Methode implementieren, wurde auf Computern mit mehreren Dutzend Kernen getestet und zeigte eine hohe Geschwindigkeit und nahezu lineare Skalierbarkeit in Bezug auf die Anzahl der beteiligten Kerne.

Approbation im Experiment STAR (BNL)

Das Schwerionenexperiment STAR (Solenoidal Tracker at RHIC) (Abb. 8.6, links) ist derzeit das einzige in Betrieb befindliche Experiment am RHIC-Beschleuniger im Brookhaven National Laboratory, USA.

Das STAR-Experiment dient der Untersuchung von Kernmaterie unter den extremen Bedingungen relativistischer Schwerionenkollisionen, einschließlich der Hadronenproduktion, der Suche nach Anzeichen für die Bildung eines Quark-Gluon-Plasmas und der Untersuchung seiner Eigenschaften.

Ein sehr wichtiges Merkmal des RHIC-Beschleunigungskomplexes ist die Möglichkeit, den gesamten Bereich des baryonischen chemischen Potenzials μ_B von 20 bis 420 MeV im Rahmen des Beam Energy Scan (BES)-Programms des STAR-Experiments zu untersuchen (Abb. 8.6, rechts). Die BES-I-Studien wurden zwischen 2010 und 2014 durchgeführt. Die zweite Phase des Beam Energy Scans BES-II wurde in den Jahren 2019 bis 2021 durchgeführt und deckt den

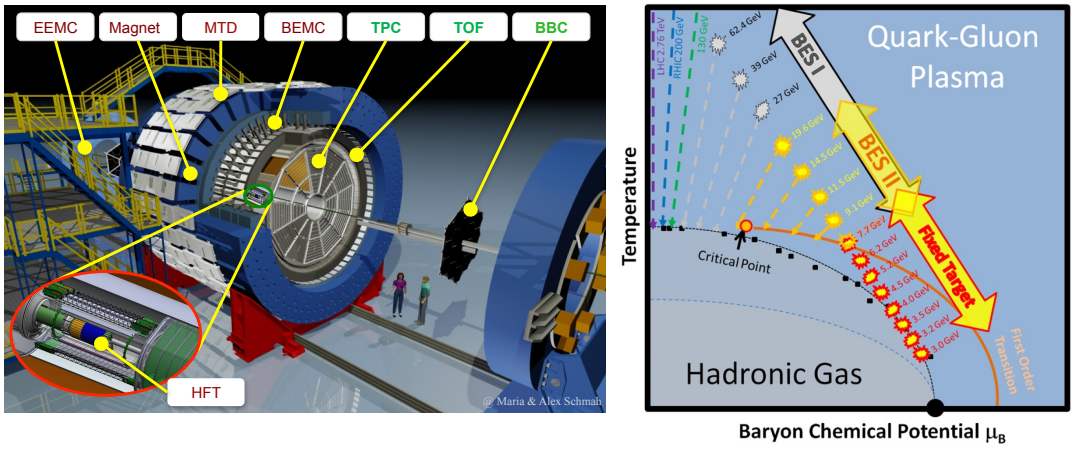

Abbildung 8.6: Links: Die STAR-Detektoranlage mit ihren Hauptdetektoren: dem elektromagnetischen Endkappen-Kalorimeter (EEMC), dem Myonen-Teleskop-Detektor (MTD), dem elektromagnetischen Barrel-Kalorimeter (BEMC), der Zeitprojektionskammer (TPC), dem Flugzeitdetektor (TOF), dem Beam-Beam Counter (BBC) und dem Heavy Flavor Tracker (HFT). Rechts: QCD-Phasendiagramm für das Beam Energy Scan (BES) Programm.

Energiebereich $\sqrt{s_{NN}} < 20$ GeV. Aktuelle Gitter-QCD-Rechnungen sagen voraus, dass wichtige Merkmale des Phasendiagramms, wie der kritische Punkt und der Phasenübergang erster Ordnung, innerhalb der Reichweite des BES-II-Programms liegen.

Vor allem für die Anfangsphase des CBM-Experiments, das für das Jahr 2025 geplant ist, ist es von besonderer Bedeutung, bereits jetzt an realen Daten die Zuverlässigkeit des entwickelten Ansatzes sowie die hohe Effizienz der derzeitigen Implementierung des gesamten KF Particle Finder Pakets und seines integralen Bestandteils, der die Missing-Mass-Methode implementiert, zu demonstrieren. Eine solche Gelegenheit bot das FAIR-Phase-0-Programm, das die Verwendung von ursprünglich für das CBM-Experiment entwickelten Softwarepaketen im STAR-Experiment ermöglichte.

Da die Rekonstruktion der Spuren im STAR-Experiment Messungen im TPC-Detektor erfordert, der sich in einer Entfernung von mehr als 50 cm vom Kollisionspunkt befindet, können die Spuren von Σ-Hyperonen wegen der kurzen Lebensdauer dieser Teilchen nicht gefunden werden, da $c\tau_{\Sigma^+} = 2,4$ cm und $c\tau_{\Sigma^-} = 4,4$ cm. Jedoch kann die Korrektheit der Missing-Mass-Methode dadurch überprüft werden, dass der Zerfall zahlreicher Strange-Mesonen wie $K^+ \to \pi^+\pi^0$ und $K^- \to \pi^-\pi^0$ mit deutlich längeren Lebensdauern rekonstruiert wird.

Um die Durchführbarkeit der Missing-Mass-Methode im STAR-Experiment zu beweisen, wurde die Methode zunächst offline auf Daten angewandt, die bereits 2016 im Collider-Modus (Gegenstrahl-Kollisionsmodus) gesammelt wurden,

und zwar auf eine Reihe von 700 K AuAu-Kollisionen bei der Kollisionsenergie $\sqrt{s_{NN}} = 200$ GeV. Die Ergebnisse zeigten eine hohe Qualität der rekonstruierten Mutterteilchen und ihrer neutralen Tochterteilchen.

Das Programm mit fixiertem Ziel, bei dem nur ein Strahl mit dem inneren Au-Ziel kollidiert, erreicht im Vergleich zum Collider-Modus eine höhere μ_B mit hoher Luminosität innerhalb von BES-II. Die Datenverarbeitung und -analyse in diesem Fixed-Target-Modus ist auch deshalb wichtig, weil die Bedingungen denen des CBM-Experiments ähneln.

Genauere Messungen in BES-II sind auch aufgrund der um Größenordnungen besseren Statistiken möglich, die durch die Aufrüstung des Elektronenkühlsystems im RHIC sowie durch die Aufrüstung der Detektoren, insbesondere des inneren Teils der Zeitprojektionskammer (iTPC) und des Endkappen-Flugzeitdetektors (eTOF), erreicht wurden.

Die Inbetriebnahme der iTPC- und eTOF-Detektoren in STAR sowie der Online-Betrieb im Fixed-Target-Modus erforderten auch umfangreiche Anpassungen des KF Particle Finders. So wurde beispielsweise der Algorithmus zur Reinigung des Hintergrunds von Teilchen, die aus dem Detektormaterial oder im Strahlrohr und im Separatorbereich zwischen dem inneren und dem äußeren Teil des TPC herausgeschleudert wurden, geändert.

Tabelle 8.2: Vergleich der Anzahl der rekonstruierten Signalteilchen in der ersten und der verbesserten Version

Version	$\pi^\pm \to \mu^\pm \nu_\mu$		$K^+ \to \mu^+ \nu_\mu$		$K^\pm \to \pi^\pm \nu^0_\pi$	
Erste	340.0	505.0	19415.7	4117.2	5609.3	1181.8
Verbesserte	15538.2	19284.1	36267.1	7688.4	10973.8	2309.9
Faktor	45.7	38.2	1.9	1.9	2.0	2.0

Die Missing-Mass-Methode wurde sowohl in ihrer ersten als auch in ihrer verbesserten Version online für die Suche nach Pionen- ($\pi^\pm \to \mu^\pm \nu$) und Kaonenzerfällen ($K^\pm \to \mu^\pm \nu$ und $K^\pm \pi^\pm \pi^0$) in realen Daten von 2 M AuAu-Kollisionen bei Energien von (5,75+7,3+9,8+26,5) GeV/n mit fixiertem Ziel eingesetzt, die im Jahr 2020 als Teil des BES-II Beam Energy Scan Programms gesammelt und online mit einer Kette von Expressverarbeitungs- und Datenanalysealgorithmen auf dem STAR HLT Computercluster rekonstruiert wurden. Es wurde gezeigt (Tab. 8.2), dass bei der verbesserten Version der Missing-Mass-Methode in den $\pi^\pm \to \mu^\pm \nu$-Kanälen das Signal um den Faktor 40 und die Signifikanz um den Faktor 7 anstieg. In den Kanälen $K^\pm \to \mu^\pm \nu$ und $K^\pm \pi^\pm \pi^0$ erhöht sich das Signal um den Faktor 2 und die Signifikanz um das 1,5 fache im Vergleich zur ursprünglichen Version.

Das umfangreiche Physikprogramm von BES-II erforderte auch eine schnelle Datenverarbeitung und eine vorläufige Physikanalyse in Echtzeit, um nicht nur die Qualität der gesammelten Daten zu überwachen, sondern auch das Erreichen des erwarteten physikalischen Ergebnisses während der Datenaufnahme zu bewerten und bei Bedarf Anpassungen am Betriebsplan des Beschleunigers vorzunehmen.

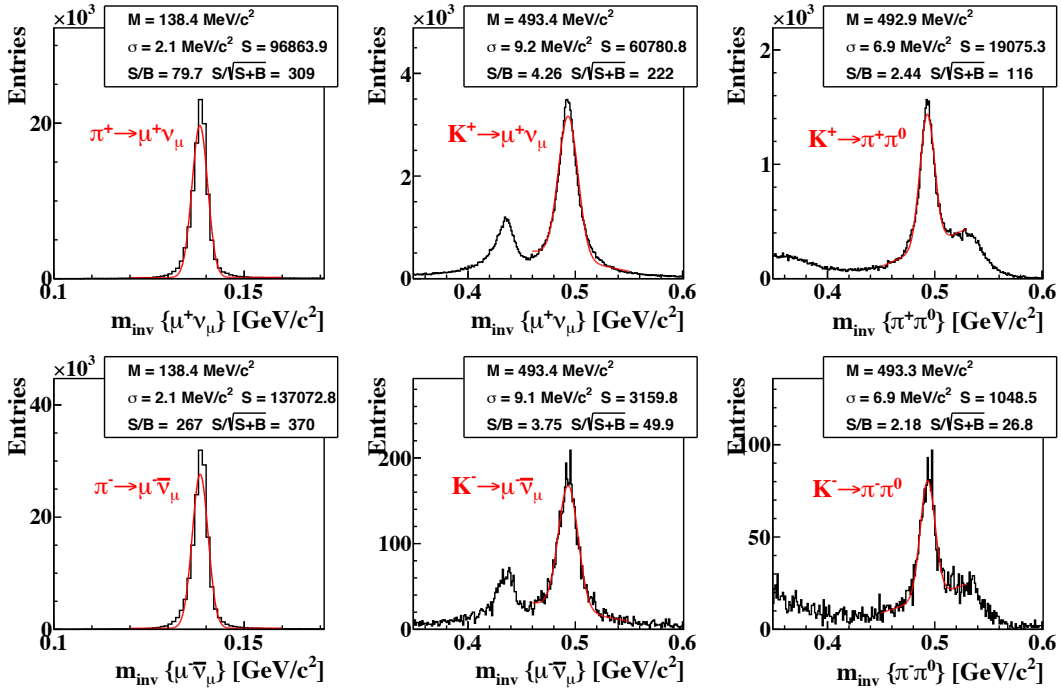

Abbildung 8.7: Ergebnisse für $\pi^{\pm} \to \mu^{\pm}\nu$, $K^{\pm} \to \mu^{\pm}\nu$ und $K^{\pm} \to \pi^{\pm}\pi^0$ Massenspektren, die bei 9 M AuAu-Kollisionen mit einem fixiertem Ziel bei einer Strahlenergie von 3,85 GeV/n erreicht wurden. Die Daten wurden am 1. und 2. Mai 2021 gesammelt und online in der Express-Kette am STAR HLT-Cluster verarbeitet.

Die Notwendigkeit einer schnellen Online-Datenverarbeitung und -Analyse hat daher zur Entwicklung schnellerer und besserer Algorithmen geführt, die später in das Standard-Offline-Datenverarbeitungssystem des STAR-Experiments integriert werden.

Abbildung 8.7 zeigt die Ergebnisse der Anwendung der Missing-Mass-Methode innerhalb der Expresskette auf 9 M AuAu-Daten, die am 1. und 2. Mai 2021 bei einer Strahlenergie von 3,85 GeV/n im Fixed-Target-Modus gesammelt wurden. Die Methode wurde verwendet, um $\pi^+ \to \mu^+\nu_\mu$, $\pi^- \to \mu^-\bar{\nu}_\mu$, $K^+ \to \mu^+\nu_\mu$, $K^- \to \mu^-\bar{\nu}_\mu$, $K^+ \to \pi^+\pi^0$ und $K^- \to \pi^-\pi^0$ Zerfälle zu finden.

Die Anwendung der Methode auf reale Daten zeigt sehr gute Ergebnisse mit einem hohen Signal-Hintergrund-Verhältnis und einem großen Signifikanzwert. Im Falle

der Pionenzerfälle $\pi^{\pm} \to \mu^{\pm}\nu$ war es möglich, ein fast reines Signal zu bekommen, wobei der Hintergrund fast vollständig verschwand. Bei den Kaonenzerfällen $K^{\pm} \to \mu^{\pm}\nu$ wird ein zweiter Peak beobachtet, der auf die falsche Identifizierung von π als μ zurückzuführen ist.

Die Ergebnisse zeigen die Zuverlässigkeit und hohe Effizienz der Missing-Mass-Methode bei der Rekonstruktion sowohl geladener Mutterteilchen als auch ihrer neutralen Tochterteilchen. Als integraler Bestandteil des KF Particle Finder Pakets, das jetzt der Hauptansatz für die Rekonstruktion und Analyse kurzlebiger Teilchen im STAR-Experiment ist, wird die Missing-Mass-Methode weiterhin für die physikalische Analyse im Online- und Offline-Modus verwendet werden.

Es sollte auch darauf hingewiesen werden, dass die hohe Qualität der Ergebnisse der Express-Datenanalyse dazu geführt hat, dass sie den Status von vorläufigen physikalischen Ergebnissen erhalten haben, mit dem Recht, sie im Namen der STAR-Kollaboration auf internationalen Physikkonferenzen und -treffen zu präsentieren.

Fazit

Die wichtigsten Ergebnisse der Dissertation:

1. Im Schwerionenexperiment CBM (FAIR) wurden die Missing-Mass-Methode und die entsprechenden parallelen Algorithmen auf der Grundlage der Kalman-Filter-Mathematik für die schnelle Suche und Rekonstruktion seltener kurzlebiger Teilchen mit neutralen Teilchen in ihren Zerfallsprodukten implementiert. Verbesserungen im mathematischen Teil der Methode führten zu einer 2-fachen Steigerung ihrer Rekonstruktionsleistung und einer 25- bis 30-prozentigen Steigerung der Signifikanz der Signaldaten.

2. Die Missing-Mass-Methode ist unter Verwendung von Vektorbefehlen (SIMD) implementiert und für den Parallelbetrieb auf modernen Multicore-Hochleistungsrechnersystemen optimiert, die sowohl Prozessoren als auch Koprozessoren umfassen können.

3. Im Rahmen des entwickelten Ansatzes werden die Prinzipien und die optimalen Werte der Merkmalsvariablen identifiziert, die es erlauben, das Signal mit hoher Genauigkeit zu isolieren und den Hintergrund zu minimieren. Insbesondere wurden Methoden entwickelt, um den physikalischen Hintergrund zu unterdrücken, der von der Wechselwirkung der Teilchen mit dem Material und den Stationen des Detektorsystems stammt, sowie den kombinatorischen Hintergrund aus falsch rekonstruierten Spuren, die einem Teilchen entsprechen, aber als zwei Teilchen, eine Mutter und eine Tochter, aus demselben Zerfall interpretiert werden.

4. Für die physikalische Analyse der Eigenschaften von kurzlebigen Teilchen wurden zwei voneinander unabhängige Methoden zur Untersuchung von Teilchenspektren eingeführt: die Seitenband- und die Multidifferenzialanalyse. Beide Methoden ermöglichen die zuverlässige Berechnung verschiedener Arten von Effizienzen sowie die Extraktion wichtiger Mediumsparameter, wie beispielsweise der effektiven Temperatur.

5. Die Algorithmen, die die Missing-Mass-Methode implementieren, wurden für das Schwerionenexperiment STAR (BNL) angepasst und im Rahmen des BES-II-Physikforschungsprogramms erfolgreich eingesetzt, um Zerfälle $\pi^+ \to \mu^+\nu_\mu$, $\pi^- \to \mu^-\bar{\nu}_\mu$, $K^+ \to \mu^+\nu_\mu$, $K^- \to \mu^-\bar{\nu}_\mu$, $K^+ \to \pi^+\pi^0$ und $K^- \to \pi^-\pi^0$ online auf dem High Level Trigger HLT-Computercluster unter ausschließlicher Verwendung freier Rechenressourcen zu finden und zu rekonstruieren.